Direct frequency comb spectroscopy of carbon monoxide in the mid-infrared

Dissertation
zur Erlangung des Doktorgrades
an der Fakultät für Mathematik, Informatik und Naturwissenschaften
Fachbereich Physik der
Universität Hamburg

vorgelegt von

Vinicius Silva de Oliveira
aus
São Paulo, Brasilien

Hamburg

2018

Gutachter der Dissertation: Prof. Dr. Franz X. Kärtner
Dr. Axel Ruehl

Zusammensetzung der Prüfungskommission: Prof. Dr. Roman Schnabel
Prof. Dr. Franz X. Kärtner
Dr. Axel Ruehl
Prof. Dr. Piotr Masłowski
Dr. Sang-Kil Son

Vorsitzende der Prüfungskommission: Prof. Dr. Roman Schnabel

Datum der Disputation: 20. Mai 2019

Vorsitzender Fach-Promotionsausschusses PHYSIK: Prof. Dr. Wolfgang Hansen

Leiter des Fachbereichs PHYSIK: Prof. Dr. Michael Potthoff

Dekan der Fakultät MIN: Prof. Dr. Heinrich Graener

Eidesstattliche Versicherung

Hiermit erkläre ich an Eides statt, dass ich die vorliegende Dissertationsschrift selbst verfasst und keine anderen als die angegebenen Quellen und Hilfsmittel benutzt habe.

Hamburg, August 2018

Vinicius Silva de Oliveira

Acknowledgments

During the course of my PhD, I have met a lot of people that helped me in so many ways and I cannot be thankful enough. Prof. Franz Kärtner has accepted to be my supervisor and allowed me to perform this work. I would like to thank Dr. Ingmar Hartl, who provided the outstanding FS-LA group and received me in his group, together with his ideas on decisive times that had a great impact on the project.

I am really grateful to have met Dr. Axel Ruehl as my supervisor and mentor, who taught me so much about the research field and a great amount of the physics I know. His guidance and ideas were crucial and, without any doubt, the many advices and amazing discussions we continue to have were an essential component during my PhD from several aspects. I also had the chance to work together with Prof. Piotr Masłowski who contributed in many ways for this thesis. His views were a fundamental contribution and I am very grateful to our discussions and to the continuous help he provided over these years.

My colleagues in the FS-LA group always helped with me no hesitation and made the daily routine joyful. It is where I had the opportunity to get to know Tino Lang, Lutz Winkelmann, Sebastian Köhler, Francesca Moglia. In particular, Peng Li, Chenchen Wan and Rudrakant Sollapur. As if it was not enough to share the office and the lab with them for several years, we did include a lot of extra hours outside the work for sharing stories and culture during our time working together.

My wife always providing inspiration, her continuous support and encouragement over these years were crucial. I thank my parents, my sister and my brother. Even with the distance they remain constantly so close and are a big part of my life. Together with tio André, they also helped me with the manuscript, each one with their own specialties. I cannot forget to thank Gina and Phillip for their help and friendship.

Abstract

Spectroscopy is a fundamental tool for the investigation of physical systems. Technical advances in spectroscopy measurements provided the ability to perform better observations of phenomena once hindered by technical limitations. Hereby, frequency accuracy plays a crucial role, from defining fundamental physical quantities, such as the second, to help understand complex molecular systems, by precisely determining their energy levels. Even though all spectral regions of the electromagnetic spectra contain meaningful information for a diversity of studies, not all have been addressed with modern spectroscopy techniques. More specific, the extension of frequency comb based spectroscopy techniques beyond spectral regions covered by laser gain materials would enable various new applications and directions for future research. This thesis describes the development of a high-performance spectrometer and its application for broadband characterization of the molecular transitions of carbon monoxide in the mid-infrared spectral region. As a light source, a fiber-based femtosecond optical frequency comb is converted to spectral regions not covered by conventional laser gain media via nonlinear frequency conversion. The temporal coherence over a broad spectral bandwidth provided by the frequency comb is explored to resolve spectral features beyond the resolution of the Fourier transform spectrometer used to analyze carbon monoxide in the Doppler broadening regime. High-frequency accuracy and high-dynamic range is demonstrated with instantaneous coverage of several molecular transitions in multiple pressure regimes. The system is capable of offering high-quality spectra in large quantity, which is as a powerful tool for acquiring benchmark spectroscopy data. Possible applications range from populating molecular databases and testing theoretical line shape models, along with the investigation of molecular transitions over broad spectral regions.

Zusamenfassung

Spektroskopie ist eine elementare Methode zur Untersuchung physikalischer Systeme. Technologische Fortschritte in der Spektroskopie haben zur Beobachtung von Phänomenen beigetragen, die aufgrund praktischer Einschränkungen bislang vorher verborgen blieben. Hierbei spielt die Frequenzgenauigkeit der Messung eine entscheidende Rolle, um z.B. physikalische Konstanten, wie die Sekunde zu bestimmen oder komplexe molekulare Systeme durch die präzise Bestimmung ihrer Energieniveaus besser zu verstehen. Obwohl alle Spektralbereiche des elektromagnetischen Spektrums für verschiedene Anwendungen wertvolle Informationen liefern können, sind nicht alle durch moderne Spektroskopiemethoden erschlossen. Besonders die Erweiterung der Frequenzkammtechnologie in Spektralbereiche, die nicht durch Lasermaterialien abgedeckt sind, würde vielseitige neuartige Anwendungen und Forschungsgebiete erschließen. Diese Dissertation beschreibt die Entwicklung eines Präzisionsspektrometers und dessen Anwendung zur Charakterisierung der Absorptionsbande von Kohlenmonoxid im mittleren infraroten Spektralbereich mit hoher Auflösung und Dynamikbereich. Als Lichtquelle wird ein Faserlaser basierter Femtosekunden-Frequenzkamm durch nichtlineare Frequenzkonversion in den mittleren infraroten Spektralbereich transferiert, der nicht durch herkömmliche Lasermedien abgedeckt ist. Die hohe zeitliche Kohärenz des Frequenzkammes (bei gleichzeitiger großer spektraler Bandbreite) wird ausgenutzt, um spektrale Merkmale auch unterhalb der nominellen Auflösung des verwendeten Fourier Spektrometers darzustellen. Dadurch konnte eine hohe Frequenzgenauigkeit bei gleichzeitiger Messung mehrerer Absorptionsbanden demonstriert werden. Das demonstrierte Spektrometer ist dadurch in der Lage eine große Menge an experimenteller Vergleichsdaten für molekulare Datenbanken oder zum Vergleich mit neuartigen theoretischen Modellen in kurzer Messzeit bereitzustellen.

Resumo

Espectroscopia é uma ferramenta fundamental para a investigação de sistemas físicos e avanços tecnológicos nesta área possibilitaram uma melhor observação de fenômenos que eram antes limitados por razões práticas. A exatidão das medidas de frequência tem um papel decisivo para a definição de grandezas físicas fundamentais, por exemplo o segundo (unidade de medida de tempo), e ajudam no entendimento de sistemas moleculares, atravéz da medição dos níveis de energia. Apesar de todas as faixas do espêctro eletromagnético conterem informações relevantes para diversos estudos, muitas não foram estudadas com técnicas modernas de espectroscopia. Especialmente importante seria ampliar a abrangência de tecnologias embasadas em pentes de frequência para regiões do espectro não cobertas por meios ativos de laser, possibilitando novas aplicações e direções para futuras pesquisas. Esta tese descreve o desenvolvimento de um espectrômetro de alta performance aplicado para caracterizar transições moleculares na região do infravermelho médio. Como fonte de luz, um pente de frequências gerado por um laser de fibra de femtosegundo é convertido para regiões do espectro não cobertas por meio de ganho convencionais, utilizando conversão não linear de frequência. A coerência temporal que abrange um amplo espectro, somente fornecida por pentes de frequência, é utilizada para distinguir características no espectro além da resolução de um espectrômetro de Fourier, usando uma amostra de monóxido de carbono no regime de alargamento Doppler. Diferentes condições de pressão foram utilizadas, e medidas com alta resolução e alta faixa dinâmica foram alcançadas com abrangência instantânea de diversas transições. O sistema oferece em larga escala espectros com alta qualidade, que podem ser processados para gerar espectros de referência. As aplicações vão desde fornecer informações para base de dados e testar modelos de teóricos de linhas espectrais, até investigar transições moleculares em amplas faixas espectrais.

Table of contents

List of Abbreviations

CW continuous wave.

DFG difference frequency generation.
DLA demodulating logarithmic amplifier.

FROG frequency-resolved optical gating.
FT Fourier transform.
FTIR Fourier transform infrared spectroscopy.
FTS Fourier transform spectroscopy.
FWHM full-width at half-maximum.

HeNe helium-neon laser.
HWHM half-width at half-maximum.

ILS instrument line shape.

LCI low-coherence interferometry.

MIR mid-infrared.

OPD optical path difference.
OPO optical parametric oscillator.

PID proportional integral derivative.
PLL phase-locked loop.

RF radio frequency.

SD speed dependent.
SDVP Speed-dependent Voigt profile.
SDVPq Speed-dependent Voigt profile with quadratic approximation.
SNR signal-to-noise ratio.

VC velocity changes.
VP Voigt profile.

List of Figures

List of Tables

1 Introduction

Gas phase spectroscopy in the mid-infrared

Spectroscopy is a powerful experimental tool in science and covers a broad range of applications [1]. Using different spectroscopy techniques, it is possible to interact with matter in different energy ranges, covering lengths scales from atomic nuclei to large molecules [2]. For instance, X-rays can be used to interact with inner-shell electrons while microwaves to the rotation of molecules. Electromagnetic radiation can be used to excite a sample and generate a response, such as the emission of electrons (X-ray photoelectron spectroscopy) or acoustic waves (photo acoustic spectroscopy) for example. In absorption spectroscopy, the ratio between incident and transmitted light is analyzed over a certain spectral range. Radiation is absorbed by the sample when the photon energy matches the energy difference between energy levels. Absorption spectroscopy can provide information about the atomic, electronic, or molecular structure of a sample. Figure 1.1 illustrates the various interactions between matter and electromagnetic radiation.

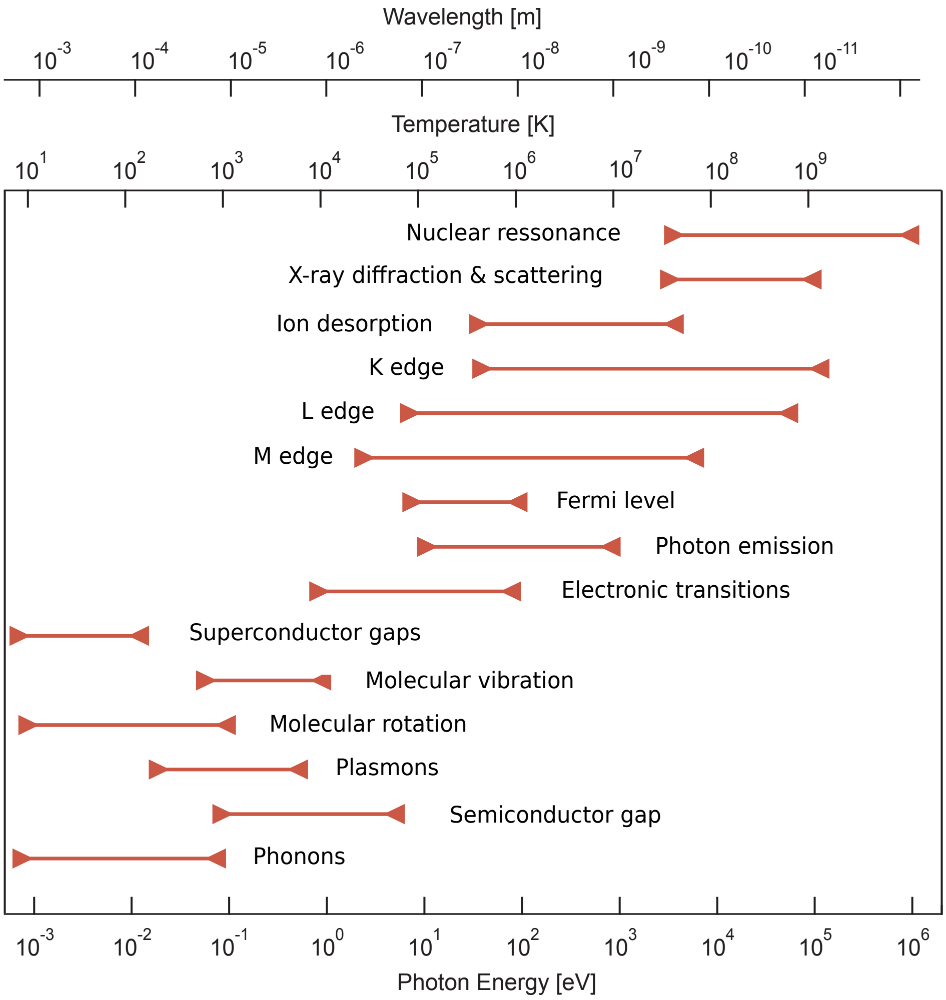

Figure 1.1: Characteristic energy scales for certain interactions between electromagnetic radiation and matter[1]. *Adapted from [1].*

There is a particular region of electromagnetic spectrum called mid-infrared (MIR). Combined effects of molecular vibrations and rotations are responsible for the absorption spectrum, referred to as ro-vibrational spectrum. Absorption in this region is influenced by parameters such as bond strength, and also by molecular interaction with the environment, such as molecular density. The MIR covers atmospheric transmission windows (3 to 5 µm, and 8 to 14 µm) which are crucial for spectroscopy, chemical sensing and biomolecular sensing. Spectroscopy in the MIR provides a way of determining dipole moments, molecular quantum numbers, and bond lengths, allowing the characterization of molecular degrees of freedom. From the macroscopic point of view, molecular absorption provides information about external influences on the sample and experimental conditions such as pressure, temperature, and concentration can be retrieved to characterize

---

[1] The boundaries are approximated. The values represent average materials and conditions. Engineered materials, as well as extreme conditions, can present values outside the respective range shown in the figure.

the environment. Figure 1.2 shows typical absorption regions for a variety of molecules and illustrates how rich this spectral region is for spectroscopy.

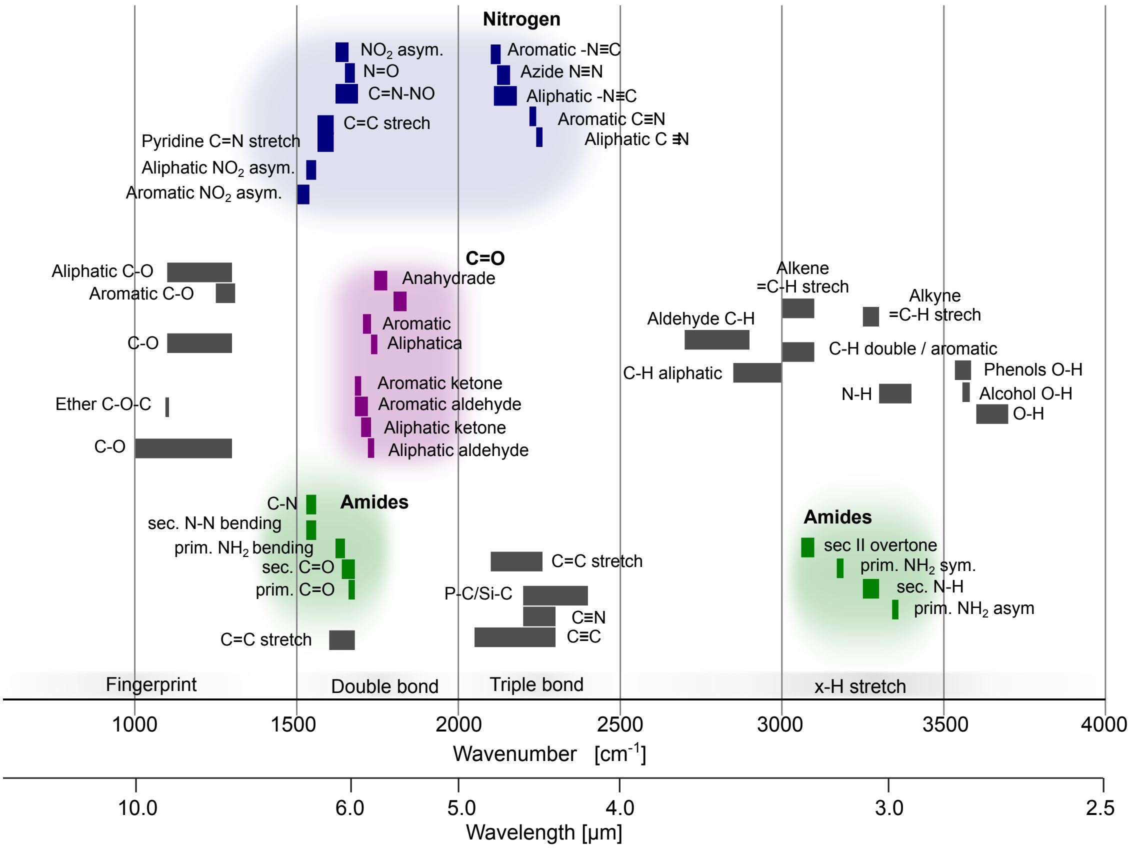

Figure 1.2: Absorption bands overview in the mid-infrared spectral region. Band positions depend not only on the atom, but also on the chemical bond and environment. This generates a rich amount of information. The abbreviations: prim. (primary), sec. (secondary), sym. (symmetric) and asym. (asymmetric). The position of the band are taken from Ref. [3]

Absorption cross-section of gaseous samples in the MIR is orders of magnitude higher than absorption regions at higher frequencies. Strong absorption leads to experimental advantages, because the interaction length between radiation and sample can be short and still provide sufficient absorption.

The MIR region of the electromagnetic spectrum is defined differently, depending on the field of study. In the short wavelength region, it starts between 2.5 μm or 3 μm. The difference is higher at longer wavelengths side, from 5 μm to 25 μm [1]. The difference can be attributed to detector and light source technology being used. In the field of spectroscopy, light sources (stars, thermal sources, and synchrotron radiation) and thermal detectors (bolometer, pyroelectric) can operate at longer wavelengths. Whether in the field of optics, typical semiconductor photodetectors (mercury cadmium telluride and indium antimonide) and nonlinear crystals (lithium niobate, barium borate, zinc germanium phosphide) have operation ranges up to 5 μm. In this thesis, the term MIR is referring to the spectral range between 3 μm and 5 μm.

Small molecules in gas phase can show absorption peaks in the MIR region, the absorption lines, which are transitions between molecular energy levels. Frequency, shape and intensity of the lines result from interplay between intrinsic properties of the sample and the experimental conditions. Spectroscopy techniques offering high-quality spectra with accuracy and precision are important source of line parameters [4, 5, 6, 7]. Molecular transitions are a source of calibration for spectroscopy experiments, for example, while studying fundamental physical constants [8]. In this particular experiment, the 1 MHz accuracy on transition frequency of water was one of the limiting factors on the value of the proton mass. The ability to cover a broad bandwidth with precision and accuracy is relevant considering the large quantity of molecular transitions yet to be studied. In some cases, for example ammonia, accurate theoretical studies predict transitions that are not covered by experimental data for comparison [9]. Broadband spectroscopy with high accuracy aids the investigation of spectral regions containing transitions predicted by theory but not yet observed experimentally. For example, the investigation of transitions involving nuclear spin conversion [10], such as in ortho/para water [11], can be combined with newly developed techniques [12].

High-resolution Fourier transform spectroscopy

Fourier transform spectroscopy (FTS) was developed in the 1950s (see [13] for a detailed review) and has become a well-established technique in many research fields [14, 15]. Especially in the infrared, as Fourier transform infrared spectroscopy (FTIR), it has been extensively explored as a broad bandwidth detection technique for molecular spectroscopy. It allows, for example, accurate measurement of transition frequencies and can cover a broad spectral with high frequency resolution [16].

The light source is one of the limiting factors in high-resolution Fourier transform (FT) spectrometers. Long optical path difference (OPD) is necessary to achieve high-resolution and the beam divergence becomes relevant. For any divergent light source, the central part of the optical beam experiences different OPD than the extremes of the beam due to the wavefront curvature. To limit the divergence of the light reaching the detector in FTIR, an aperture is used to select only the central part of the beam. This aperture reduces the available light intensity reaching the detector. It is common to find spectrometers achieving the highest resolutions in synchrotron light sources which can provide light with high power spectral intensity. Table 1.1 shows high-resolution FT spectrometers around the world (from [17]).

Table 1.1: List of high-resolution FTS based on the nine-chamber Bruker IFS 125 HR system (maximum OPD = 9.8 m). The last entry corresponds to the eleven-chamber system with 11.7 m maximum OPD.

Institute	Location	References
ETH Zürich, Laboratory of Physical Chemistry	Zürich, Switzerland	[18, 19]
University of Saskatchewan, Canadian Light Source	Saskatoon, Canada	[20, 21]
Australian Synchrotron	Melburne, Australia	[22]
Institute of Atmospheric Optics Russian Academy of Sciences	Tomsk, Russia	[23]
Institute for Spectroscopy RA, Center for Fourier Spectroscopy	Troitsk, Russia	[24]
National University of Defense Technology	Changsa, China	[1]
Advanced Light Source Division Lawrence Berkeley Laboratory	Berkeley, USA	[25]
Synchrotron Soleil	Paris, France	[26]
Swiss Light Source ETH Zürich	Villigen, Switzerland	[27]

The use of incoherence light sources present difficulties at high resolutions, long optical path, and high sensitivity, due to low spatial coherence and brightness [28]. Nevertheless, several molecular databases rely on results from studies using a combination between FTIR and incoherent light sources [4, 29, 6, 5]. Techniques using continuous wave (CW) lasers as light source and cavity-enhanced methods [30] developed as a parallel approach, and shifted the focus to narrow band detection with improved sensitivity and resolution. Experimental data became available and were incorporated to molecular databases [4, 5, 6, 7]. Developments on coherent light sources to spectroscopy applications provide a way to combine broadband detection with sensitivity and accuracy, offering an alternative to CW laser based spectroscopy systems. Faster acquisition due to

---

[1] This entry is on the original table from [17], however, references regarding this spectrometer were not found.

shorter averaging time and the coverage of multiple transitions at once can be employed to provide new input to databases, especially in regions not covered by experimental data.

Mid-infrared coherent light sources

Temporal coherence is important for achieving high-resolution, frequency accuracy and precision, which is of great interest for spectroscopy. Spatial coherence has a particular importance in Fourier transform spectroscopy. It allows for example a high-brightness beam to be transported over long distances. Coherent light sources with adjustable output spectrum in the MIR offer the possibility to instantly cover absorption bands of various molecules [31]. Femtosecond lasers are an attractive solution providing, in addition to spatial and temporal coherence, the spectral bandwidth to cover numerous absorption features at once. Short pulses from mode-locked lasers using MIR gain media have many applications [32]. On the other hand, the lack of established laser technology at arbitrary spectral regions limits the direct application of femtosecond lasers to specific spectral regions [33].

Nonlinear frequency conversion is an alternative approach to generate optical frequencies in spectral regions not covered by laser gain media [34]. The nonlinear interaction between high intensity optical fields and a nonlinear medium, usually a crystal, is explored to generate new optical frequencies. Several techniques provide a way to transfer specifications of established laser technology to the MIR [35, 36]. Among them, the optical parametric oscillator (OPO) and difference frequency generation (DFG) are widely explored concepts. In both cases, the process is mediated by second order nonlinearities and three optical fields are involved. They are defined from high to low photon energy as pump, signal and idler. In an OPO, the crystal is inside a cavity and the process initiates from noise by the intense pump field. As a result, idler and signal are generated [37, 38]. In the DFG, the signal field is generated beforehand to act as a seed and the interaction with the pump develops during a single pass through the crystal [39].

The OPO can operate solely relying on passive stability when carefully designed for this purpose [40]. However, practical applications, especially low-noise spectroscopy, require active stabilization of several parameters to provide stable output over hours of operation. Despite the fact that optical cavities are present in low noise applications and can be explored to increase the performance of optical systems [30], they also add complexity in the set-up. Optical parametric oscillators need to be operated at degeneracy for a predictable relation between input and output comb structure, limiting the spectrum coverage [40, 41]. In this thesis, the light source for the spectrometer is based on DFG. Difference frequency generation has been extensively used to generate mid-IR combining different techniques, for example, from CW fields [42], to a combination between CW and picosecond lasers [43]. The single-pass interaction through the nonlinear crystal is performed without optical cavities. It is possible to adjust the idler wavelength by changing the signal wavelength and phase matching conditions.

Short pulses from mode-locked femtosecond lasers have high peak powers, which allow nonlinear frequency conversion to be performed efficiently. The short pulse is generated by the interference of modes resonating in the oscillator cavity. Temporal and phase coherence of the output electric field can be actively controlled via phase locking the laser oscillator to optical and radio frequency (RF) references. The result is the generation of the so called optical frequency combs [44, 45]. The output spectrum of frequency combs is composed by periodically spaced modes whose positions are known and can be controlled with high accuracy and precision. Hundreds of thousands cavity modes, each one of them viewed as a single frequency laser and covering THz of bandwidth. Frequency combs provide many advantages for spectroscopy and several demonstrations in mid-infrared have been performed based on a variety of laser technology, such as Ti:Sapphire [46], Er:fiber [47], Yb:fiber [48] and Tm:fiber [49].

The combination of frequency combs, DFG to reach the MIR spectral region, and FTS is a powerful tool. Frequency combs offers a broadband light, which is highly coherent. It can be explored to favor bandwidth and resolution while maintaining high frequency accuracy. Operating in the MIR allows low pressure measurements in short sample path length, as the absorption cross-section is orders of magnitude stronger than the absorption at lower wavelengths. The frequency conversion needs to be selected with attention to the coherence of the optical fields involved in the process, which must be maintained to preserve the frequency comb structure [50]. Difference frequency generation can generated frequency combs with adjustable output spectrum over a broad spectral range. The detection of MIR is challenging, as many techniques present distinct advantages, trading optimization of parameters such as resolution, bandwidth, precision, accuracy, and sensitivity. Among several techniques, FTS offers resolution and high signal-to-noise ratio (SNR), at reasonable acquisition times when the broad bandwidth is considered.

Thesis objective and structure

The main objective of the thesis is to develop a spectroscopy system, composed by several parts. Difference frequency generation converts a Yb:fiber frequency comb to the MIR spectral region. For the detection, a custom FT spectrometer was constructed. The mid-infrared spectroscopy system is applied to detect radiation in the spectral region from 3 to 5 µm. The gas sample is contained in a single pass cell for the absorption measurements. Specific objectives of the project are defined as follow:

- Generate a MIR frequency comb
- Design a Fourier transform spectrometer
- Perform spectroscopy in gas phase
- Develop data analysis to retrieve high-quality spectroscopy results
- Utilize the frequency comb to acquire high-resolution spectra
    - Produce spectra with high signal-to-noise ratio
    - Achieve precision and accuracy in frequency and amplitude
    - Retrieve absolute values for the cross section and line parameters

The thesis is structured as follows. Chapter 2 introduces basic principles about molecular spectroscopy and high-resolution Fourier transform spectroscopy focusing on frequency combs in the mid-infrared as light source. Chapter 3 describes the laser and the frequency conversion stage for the MIR generation. Chapter 4 shows the construction of the Fourier transform spectrometer. It contains details regarding the design and assembly steps of the equipment, concentrating on high-resolution, high signal-to-noise ratio detection. The results are presented in chapter 5. Chapter 6 contains the conclusion an outlook.

2 High-resolution Fourier transform spectroscopy of molecules in gas phase with frequency combs

2.1 Molecular rotation and vibration

The absorption spectra of small molecules in gas phase in the MIR region occurs due to a combination between rotational and vibration states. The spectrum is composed by absorption lines, whose frequency corresponds to the difference between energy levels of the molecule. Although quantum mechanics provides the tools for modeling and interpreting high-resolution absorption spectra, a complete theoretical description is beyond the scope of the thesis. Nevertheless, the underlying mechanisms responsible for the absorption spectra of simple systems can be described semi-classically. This section provides a brief introduction with concepts applied to molecular spectroscopy, based on a diatomic system.

2.1.1 Born and Oppenheimer approximation

The Born and Oppenheimer approximation is based on the assumption that the electrons are less massive and move faster than the nuclei, i.e. the electronic response for the movement of the nuclei is instantaneous [2]. The separation between molecular and electronic transitions is possible because they occur in different time and energy scales. Time scales are approximately in the order of 1 fs (electronic), 10 to 100 fs (vibrational), and 0.1 to 10 ps (rotational). The energy scales cover different ranges as showed in the previous section, in figure 1.1. To a first approximation, nuclei positions can be considered fixed for the fast-moving electrons. In contrast, by the time the nuclear vibrations take place, an average electronic cloud can be assumed. In addition, during molecular rotation the nuclei position can assumed to be at an average vibrational motion.

2.1.2 Vibration

In a classical view, diatomic molecules can be considered as masses connected by spring-like bonds, as shown in figure 2.1. Despite being more complex system, such a simple representation can be applied to estimate, to a certain level of precision, the frequency of absorption lines.

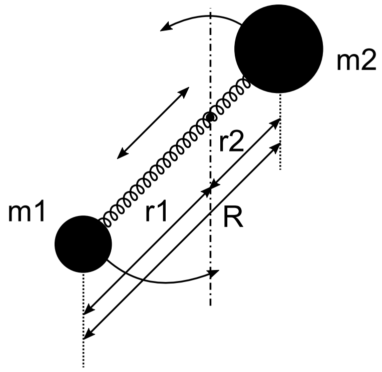

Figure 2.1: Illustration of a diatomic molecular system. A molecule composed by two different atoms can be represented as a system of two masses connected via a spring-like bond.

In such a system, there is one mode of vibration corresponding to the stretching of the bond. If the atoms masses are m_1 and m_2, the reduced mass can be expressed as

$$\mu = m_1 m_2/(m_1 + m_2). \tag{2.1}$$

The linear stretching of the bond is treated using Hook's law with the force constant f, which yields the fundamental frequency of vibration, ω_e, in the form

$$\omega_e = \frac{1}{2\pi c}\sqrt{\frac{f}{\mu}}, \tag{2.2}$$

where c is the speed of light. The simplified system can be considered a harmonic oscillator, for which the potential energy, V_h is a function of the separation R between the nuclei, which oscillates at the equilibrium distance, R_e

$$V^{harm}(R) = \frac{1}{2}f(R - R_e)^2. \tag{2.3}$$

In reality, molecules are composed by positively charged nuclei and negatively charged electrons. Quantum mechanics provide the basis for interpreting molecular spectra. The energy levels for the harmonic oscillator is quantized and can take only discrete values in the form

$$E_v^{harm} = \omega_e(v + \frac{1}{2}), \tag{2.4}$$

where the vibrational quantum number $v = 1, 2, 3, ...$ is introduced, and E_v^{harm} is in wavenumbers. In this approximation, the energy spacing between adjacent levels is independent of the quantum number v. For increasing vibrational levels, the approximation based on the harmonic potential start to differ by higher amounts from the observable values. A better approximation is to consider the bond as not rigid. The Morse potential is commonly employed in the modeling and it can be written as

$$V^{Morse}(R) = D_{eM}[1 - e^{-a(R-R_e)}]^2, \tag{2.5}$$

where D_{eM} is the bond dissociation energy in wavenumbers. The term a can be calculated by

$$\begin{aligned} a &= \omega_e\sqrt{2\pi^2 c\mu/(D_e h)}, \\ a &\simeq 1.2177 \times 10^7 \omega_e \frac{\mu}{D_e}, \end{aligned} \tag{2.6}$$

with Planck's constant h in Js, the fundamental frequency ω_e and D_e in wavenumber, and the reduced mass, μ, in Dalton.

For the Morse potential, the approximated energy eigenvalues are

$$E_v^{Morse} = \omega_e(v + \frac{1}{2}) - \omega_e x_e(v + \frac{1}{2})^2. \tag{2.7}$$

The anharmonicity constant x_e is a property of the molecule. Assuming that the molecule can be represented by the Morse potential, it is possible to write calculate the dissociation energy using the relation:

$$D_{eM} = \frac{\omega_e^2}{4\omega_e x_e}. \tag{2.8}$$

Figure 2.2 illustrates the difference between the harmonic and the Morse potential curves calculated using CO molecular parameters [51]. The inset shows the energy difference for the first vibrational v states.

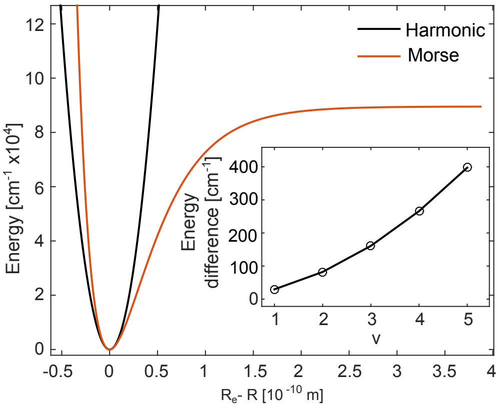

Figure 2.2: The difference between the harmonic and Morse potential is illustrated. The inset shows the energy difference between the first five vibrational levels for the two potentials.

2.1.3 Rotation

In addition to vibration, molecules in gas phase are free to rotate due to the lack of intermolecular forces present in solid and liquid phases [2]. The rotation energy is connected to the moment of inertia, I, which for the two atom system in figure 2.1 can be written as

$$I = \mu R^2. \tag{2.9}$$

As in the vibrational case, rotational states are quantized and can only have discrete energy values. The absorption of radiation occurs at particular frequencies, giving rise to a series of spectral lines which lies in the microwave spectral region. The quantum number J is used to represent the change the rotational angular momentum and the energy for a rigid rotator is given by

$$E_J = J(J+1)\hbar^2/2I = BJ(J+1), \tag{2.10}$$

where $B = \hbar^2/2I$ is the rotational constant for the rigid rotator. This description can be extended to include the increase in separation between the nuclei for higher rotational stages due to centrifugal forces. The result is a successive shift towards lower energy as the rotational level is increased. The new energies can be calculate with the addition of the constants B_v and D_v, to yield

$$E_J = B_v J(J+1) - D_v J^2(J+1)^2. \tag{2.11}$$

The subscript v indicates the dependence on the vibrational levels. The values of the vibrationally dependent constants for rotation, B_v, and centrifugal distortion, D_v are connected to quantum number v given by

$$\begin{aligned} B_v &= B_e - \alpha_e(v + 1/2) \\ D_v &= D_e - \beta_e(v + 1/2). \end{aligned} \tag{2.12}$$

The constants B_e and D_e represent the rotational and the rotation-vibration interaction constant at equilibrium, and the respective coupling constants α_e and β_e. A diatomic system helps to illustrate the connection between the absorption spectra and molecular parameters. The theoretical description presented here includes approximations that need to be reconsidered for accurate calculations. For polyatomic molecules, the complexity of the treatment greatly increases and there is not simple energy level formulae available.

2.1.4 Selection rules and the ro-vibrational spectrum

Molecular vibrations influence the moment of inertia and thus shift the value of the rotational constant B_v to lower values. This coupling gives rise to the ro-vibrational spectra and the energy lies in the MIR spectral region.

Transitions between energy levels are infrared active, i.e. radiation is absorbed, if there is a change in the molecular dipole moment. The allowed transitions are given by a combination between rotational and vibrational quantum numbers, which can take the values

$$\begin{aligned} &\Delta J = \pm 1, \text{ and} \\ &\Delta v = \pm 1, 2, 3, \dots . \end{aligned} \tag{2.13}$$

The rotational quantum number can either increase or decrease by one, which corresponds to a transition between energy levels, leading to a separation of the energies into two branches. The R branch represents a transition of increasing rotational quantum number ($\Delta J = +1$), whereas the P branch represents a decrease ($\Delta J = -1$). To represent the energies for the branches, it is necessary to consider the total energy of the transition as function of the vibrational E_v and rotational E_j energies, $E_{(v,j)} = E_v + E_J$. Assuming the energies from equations 2.7 and 2.11, and using the representation $B' = B_v(v')$ and $B'' = B_v(v'')$ for the upper and lower states, the energy for the P branch, $P(v, J)$, and R branch, $R(v, J)$, can be written as:

$$\begin{aligned} R(v,J) &= \Delta E_v + 2B' + (3B' - B'')J + (B' - B'')J^2 \\ P(v,J) &= \Delta E_v - (B' + B'')J - (B'' - B')J^2. \end{aligned} \tag{2.14}$$

In these equations, it is assumed functions of the lower quantum numbers only (v'' and J'') and the double prime in J is omitted for clarity. It is common to represent the transitions as $R(J'')$ and $P(J'')$, for example, R(7) indicates a transition from the lower $J'' = 7$ to the upper $J' = 8$ level. Figure 2.3 illustrates the transitions for a change of $\Delta v = 1$ and multiple values of J.

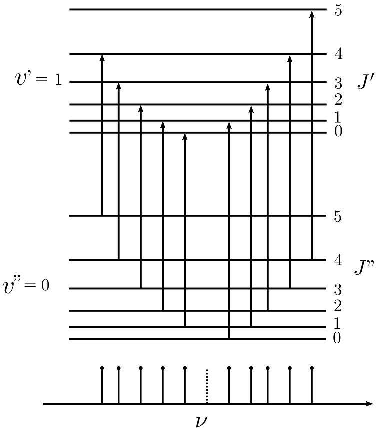

Figure 2.3: Illustration of transitions between vibrational and rotational states and the corresponding energy in the frequency spectrum (ν).

2.2 Absorption spectroscopy

When light enters a gas sample, scattering and reflection are usually negligible and the incident light is either absorbed or transmitted.

$$\underbrace{\text{absorption}}_{A} + \underbrace{\text{transmission}}_{T} + \underbrace{\text{reflection}}_{=0} + \underbrace{\text{scattering}}_{=0} = 100\%$$

A monochromatic light beam with intensity I_0 [W/cm^2], suffers attenuation over the path length L which can be described via [52]

$$dI = -\alpha_\nu I_0 dL, \tag{2.15}$$

where α_ν [cm^{-1}] is the absorption coefficient, which gives the relative intensity decrease dI/I_0 along the absorption path L. The integration of equation 2.15 yields the Beer-Lambert law

$$I_T(\nu) = I_0 \exp(-\alpha_\nu L). \tag{2.16}$$

In absorption spectroscopy, the ratio between transmitted I_T and incident I_0 light is detected as a function of the incident light frequency ν. A typical arrangement for absorption spectroscopy is illustrated in figure 2.4.

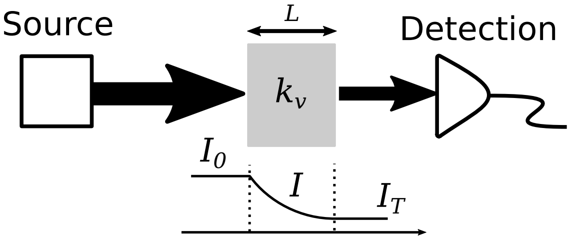

Figure 2.4: Simple absorption spectroscopy experiment with the light intensity represented at the bottom.

The absorption coefficient is measured experimentally and it is described by the relation between intensities over the interaction length

$$\alpha_\nu = -\frac{1}{L} \ln \frac{I_t}{I_0}. \tag{2.17}$$

The absorption coefficient is proportional to the concentration of absorbers in the sample path. In gas-phase spectroscopy, α_ν can be written as a function of the number density of absorbers N [molecules/cm^3] and a normalized line shape function ϕ_ν [cm], which provides the shape of the absorption [53]. For a single transition, isolated from other absorption features, between the lower i and upper j energy levels, it is convenient to write the absorption coefficient

$$\alpha_\nu = S_{ij} N \phi(\nu), \tag{2.18}$$

where S is the integrated line strength per molecule [(cm^{-1}/(molecules × cm^{-2}))]. The shape of the absorption provides information about the molecular environment and the interaction among absorber molecules. In the next section, particular shapes of $\phi(\nu)$ are discussed in detail. The number density N, is calculated by the ideal gas law $pV = n_v k_b T$, written in the form

$$N = \frac{n_v}{V} = \frac{p}{k_b T} \tag{2.19}$$

where p is the pressure, T is the temperature, n_v is the number of molecules in the volume V, and k_b the Boltzmann constant.

Integrating the absorption coefficient over the absorption line yields

$$S_{ij}^* = \int_{\text{line}} \alpha(\nu) d\nu, \tag{2.20}$$

where S_{ij}^* is the integrated line strength in units [cm^{-2}], representing the area under the absorption line. The integrated line strength, divided by the number density yields

$$S_{ij}[(\text{cm}^{-1}/(\text{molecules} \times \text{cm}^{-2}))] = \frac{S_{ij}^*[\text{cm}^{-2}]}{N[\text{molecules}/\text{cm}^3]}, \tag{2.21}$$

The area under the absorption line is measured experimentally and equation 2.20 provides the relation to the absorption coefficient. The line shape function is by convention normalized to unity, so that the integral over frequency is

$$\int_{-\infty}^{+\infty} \phi(\nu) d\nu = 1. \tag{2.22}$$

The absorption coefficient is proportional to the population density in the lower level of the absorption transition, and to the strength of the transition. The population density follows the Boltzmann distribution while the strength of the transition is related to the Einstein coefficient of induced absorption (B_{12}) [53]. The complete derivation of the relations is extensive and goes beyond the scope of this thesis. However, it is important to state that the line intensity can also be expressed as

$$S_{ij} = \frac{h\nu}{c} N B_{12}(1 - \exp(-h\nu/k_b T)), \tag{2.23}$$

which illustrates that the line strength is a fundamental property of the molecule. Measurements which provide accurate energies (frequency accuracy), shape (high SNR, resolution), and intensity (high SNR) of absorption lines provide understanding of fundamental physical processes, and about the molecular environment, as will be discussed in the next section with the discussion of line shapes.

2.3 Molecular line shape profiles

The previous section described how the center frequency of absorption lines is related to the molecular constants. In addition to the center frequency, the line is characterized by its shape, which is caused by three main line broadening mechanisms [53].

Due to the limited lifetime Δt of an excited state, the line presents a so-called intrinsic or natural linewidth described by a Lorentzian profile with half-width at half-maximum (HWHM) of $\Gamma_N = 1/2\pi\Delta t$. Molecules in gas phase have typical Δt in the order of milliseconds, which corresponds to a natural linewidth in the kHz range.

Molecules in gas phase are free to move due to the lack of intermolecular forces and are affected by the Doppler effect. Molecules with velocity components moving towards and molecules with velocity components moving away from the light beam, will absorb light at slightly shifted frequencies from the central frequency ν_0 of the transition. The thermal distribution implies that there are several classes of molecules with equal velocity component, causing an inhomogeneous broadening. For a molecule with velocity v_a, the shift is given by $\Delta\nu_D = \pm(v_a/c)\nu_0$. The effect of Doppler broadening is represented by a Gaussian distribution with HWHM Γ_D which models the Doppler broadening is represented by

$$F_D(\nu - \nu_0) = \sqrt{\frac{\ln 2}{\pi}} \frac{1}{\Gamma_D} \exp\left[-\ln 2 \left(\frac{\nu - \nu_0}{\Gamma_D}\right)^2\right]. \tag{2.24}$$

At a certain temperature, T [K], the sample with molecular mass m [kg] has a Doppler half-width Γ_D in Hz for the transition at a frequency ν_0

$$\Gamma_D = \nu_0 \sqrt{\frac{2 \ln 2 kT}{mc^2}}, \tag{2.25}$$

where the Boltzmann's constant k, is given in $[J \cdot K^{-1}]$.

The third broadening mechanisms is due to collision between molecules, which decrease the excited state lifetime. As the number of collisions is proportional to the pressure and all the molecules experience the same pressure, this type of broadening is homogeneous. This mechanism is called collisional or pressure broadening and it is represented by a Lorentzian profile (F_L), with the pressure-induced line shift (Δ_p)

$$F_L(\nu - \nu_0) = \frac{1}{\pi} \frac{\Gamma_L}{(\nu - \nu_0 - \Delta_p)^2 + \Gamma_L^2}. \tag{2.26}$$

The HWHM linewidth Γ_L has components which depend on the gas mixture. Pressure broadening is induced by collisions among the absorber molecule, also called self-broadening with the coefficient γ_s . In addition, it has components accounting for collision between the absorber molecule and other molecules in the mixture, p_j. With partial pressure p_s for the absorber, p_j for the j^{th} molecule, the Lorentzian HWHM is given by:

$$\Gamma_L = \Gamma_N + \gamma_s p_s + \sum_j \gamma_{aj} p_j. \tag{2.27}$$

The pressure-induced frequency shift due to collision $\Delta\nu_p$ is given by accounting for all the contributions collisions:

$$\Delta_p = \sum_j \gamma_{aj} p_j. \tag{2.28}$$

At low pressures, Doppler effect dominates and the contribution to the line shape is mostly caused by thermal effects. As the pressure increases, collisional effects become important.

To a certain degree of precision, the line shape can be approximated via a convolution between a Gaussian and a Lorentzian profile. The results of this convolution is the Voigt profile (VP) and it is characterized by the three parameters Γ_D, Γ_L, and Δ_p. The VP has widespread use in spectroscopy studies [54]. Despite not having an analytical solution, fast computational codes are available which makes the VP suitable for complex spectrum analysis [55, 56].

It has been widely reported in the literature that VP does not provide an accurate description for spectral line shapes [57]. The difference is observed in high-quality measurements and they have been reported for a variety of molecules and experimental conditions [58, 59, 60, 61]. The observed discrepancies from the VP can be attributed to two effects. Velocity changes (VC) due to collisions reduce the Doppler width Γ_D, and the speed dependent (SD) influence on the relaxation rates, which corrects the Lorentzian shape for different velocity-classes of the absorber molecule.

2.3.1 Line shapes beyond the Voigt profile

In the VP it is assumed that collisions occur with the average speed of the molecules, which yields the Lorentzian width. A more accurate description of the line shape is achieved by considering the Lorentzian as a function of the molecule speed, which follows a Maxwell-Boltzmann distribution. The effect can be modeled by introducing the SD collisional broadening and the SD shifting of the line [62, 63]. The VP can be modified to include these effects and generate the speed-dependent Voigt profile (SDVP) [64]. The SD width and shifting can be described by the hypergeometric function [63]. It is important to notice that there is no analytical solution for the VP and neither for the profiles originated from it. The SD effects are small and for a mass ratio between absorber and perturber close to one, the hypergeometric function can be approximated by a quadratic function and the model is known as speed-dependent Voigt profile with quadratic approximation (SDVPq). This model is employed for fitting absorption lines in chapter 5.

The theory behind modeling line shape profiles is extensive and beyond the scope of the thesis [65, 66]. A variety of line shape models have been developed to include high order effects, resulting in sophisticated models with different modeling of the underlying physics. There are several approaches to include SD and VC parameters in the calculation and table 2.1 shows a few profiles to illustrate the number of parameters.

Table 2.1: Line shape profiles, the respective fitting parameter, the inclusion of speed dependence SD and velocity change VC effects. Soft-collision models assume that many collisions are necessary to change the molecular velocity significantly. Hard-collision models assume that the collision is violent and the velocity before and after each collision is uncorrelated.

Acronym	Profile Name	Parameters	SD	VC
DP	Doppler	Γ_D	no	no
LP	Lorentz	$\Gamma_L,\ \Delta_p$	no	no
VP	Voigt	$\Gamma_D,\ \Gamma_L,\ \Delta_p$	no	no
GP	Galatry	$\Gamma_D,\ \Gamma_L,\ \Delta_p,\ \nu_{vc}$	no	soft
RP	Rautian	$\Gamma_D,\ \Gamma_L,\ \Delta_p,\ \nu_{vc}$	no	hard
NGP	Nelkin-Ghatak	$\Gamma_D,\ \Gamma_L,\ \Delta_p,\ \nu_{vc}$	no	hard
SDVP	Speed-dependent Voigt	$\Gamma_D,\ \Gamma_0,\ \Delta_0,\ \Gamma_2,\ \Delta_2$	yes	no
HTP	Hartmann-Tran	$\Gamma_D,\ \Gamma_0,\ \Delta_0,\ \Gamma_2,\ \Delta_2,\ \nu_{vc},\ \eta$	yes	hard

The speed dependent effects are small compared to the overall shape of the line. To illustrate the difference between this effects, figure 2.5 shows the simulation of VP and the SDVP. The residuals (the difference between the measured profile and the fittings) have a characteristic shape observed in the bottom of the figure.

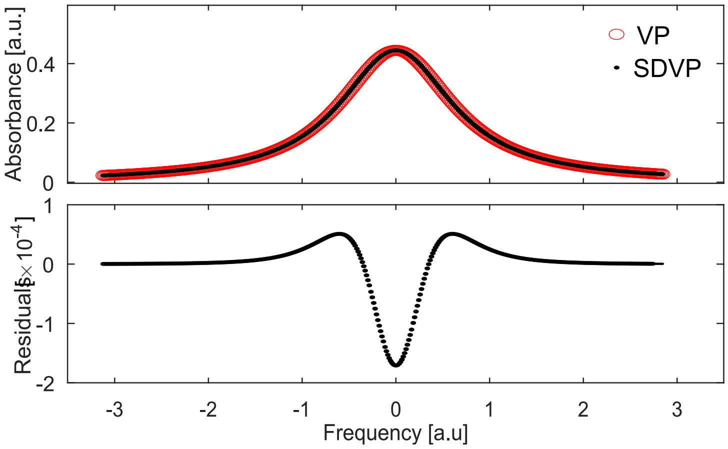

Figure 2.5: Comparison between simulated (VP) and (SDVP) to illustrate the effect of the speed-dependent effects in the line profile. The difference (VP−SDVP) is small and can only be seen in the residuals.

Additional free parameters result in better agreement with the measured spectra, but does not represent a validation of the line shape model. In order to achieve meaningful results with complex models, it is necessary to observe multiple lines and perform measurements at different pressures. Multi-spectrum analysis have the advantage of reducing uncertainties and correlation between parameters. However, high-precision measurements covering a broad spectral range are challenging and a suitable experimental setup is of great interest. To provide high-quality data is the main objective of the spectroscopy experiments.

2.4 Frequency combs

Optical frequency combs are optical sources whose spectrum is composed by equally spaced frequency structure. Various techniques can be employed to generate optical frequency combs, for example, high-repetition rate combs from microresonators [67], adjustable quantum cascade lasers which can cover the MIR spectral range [68], and from the modulation of continuous-wave lasers [69]. When carefully stabilized, the periodic frequency structure serves as optical reference and it is beneficial for a variety of applications [70]. Although many techniques are suitable for the generation of frequency combs, femtosecond lasers are differentiated. They provide ultra-short pulses that can be amplified, generating high intensities for nonlinear conversion and broad spectral bandwidth. In addition, frequency combs from femtosecond lasers present the highest coherence among laser sources, with well-defined frequency of all the comb lines [44, 45]. Femtosecond laser technology is broadly available and femtosecond frequency combs have been demonstrated using several technologies [71].

When originated from mode-locked lasers, the comb structure in frequency domain arises from the phase coherence between the modes of the cavity, and is observed via the interference of the pulses train [72]. The frequency of the n-th comb line ν_n in the optical region is linked to two radio frequencies. One is the repetition frequency (f_{rep}) of the pulse train, directly related to the comb spacing in frequency domain. The other originates from the carrier-envelope offset phase (ϕ_{ceo}), which is the phase shift between the peak of the carrier wave and the peak of the envelope. The pulse-to-pulse phase shift generates an offset in the comb structure f_{ceo}, given by: $f_{\mathrm{ceo}} = \frac{1}{2\pi} f_{rep} \Delta\phi_{\mathrm{ceo}}$. Figure 2.6 illustrates the relation between these parameters from the time and frequency domain picture.

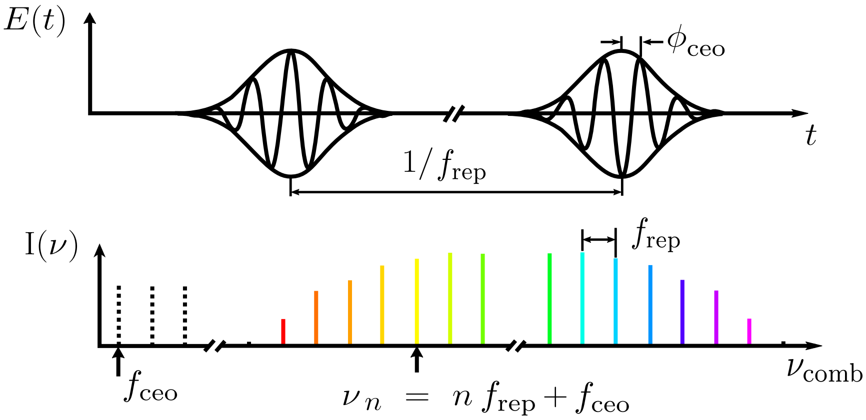

Figure 2.6: Representation of the frequency comb structure from mode-locked lasers, illustrating the relation between time domain and frequency domain parameters.

The carrier-to-envelope offset phase originates from the difference between phase velocity (v_p) and group (v_g) velocity, i.e. the dispersion in the cavity experienced by the pulses. For a round trip cavity length L_c and a carrier frequency ω_c, the phase change is

$$\Delta\phi_{\text{ceo}} = L_c\omega_c\left(\frac{1}{v_g} - \frac{1}{v_p}\right). \tag{2.29}$$

The frequency of the comb lines, ν_n, can be calculated via the comb number represented by an integer, n, and to the comb parameters, f_{rep} and f_{ceo}, by the so-called comb equation

$$\nu_n = n f_{\text{rep}} + f_{\text{ceo}}. \tag{2.30}$$

The stabilization via phase-locked loops to radio frequency standards allow the frequency of the comb modes to be known and the control over the complete comb structure. Accurate measurements of optical frequencies preceding frequency combs required sophisticated radio frequency chains, as the standard references are based on hyperfine atomic transitions in the microwave region [72]. Frequency combs create a link between radio frequencies and optical frequencies, which can be explored in a variety of ways [73]. The comb structure acts as frequency reference because the comb lines are know to the highest degrees of accuracy and precision among optical references, which is maintained even after nonlinear frequency conversion [46]. The linewidth is limited by the references used to stabilize the laser and can reach values at the mHz level [74].

Stabilization of the repetition rate and carrier-to-envelop offset phase is the requirement for generating a frequency comb with known structure. There are several approaches to achieve a fully stabilized oscillator [75] and the procedure can be separated into two steps. The first step is to generate the error signal that will be used to stabilize the two RF frequencies f_{rep} and f_{ceo}, which is usually independently of the selected laser technology. The second step is to control these parameters via actuators in the oscillator. This step can be significantly different depending on the oscillator, as different gain media and oscillator designs have distinct properties [75].

Between the two comb parameters, the repetition rate is easily detected. With the help of a photodiode, it is possible to compare the signal with the RF reference and generate an error signal. The main disadvantage in this method is that phase noise scales quadratically with the comb number. The RF reference phase noise is transferred to optical frequencies multiplied by the square of the comb number, which has typical values in the order of $n = 10^6$.

Instead of using the repetition rate to generate an error signal, a heterodyne optical beat between the comb and CW laser reference can performed to generate the error signal (f_{beat}). In this method, phase noise and frequency noise are directly coupled in the optical frequency, thus avoiding the quadratically scaling and the multiplication factor. The beat note (f_{beat}) is the result between the heterodyne beat with the closest comb mode (n_{beat}) and the frequency of the reference (ν_{ref}). The comb equation can be written as a function of the beat frequency

$$f_{\text{beat}} = \underbrace{n_{\text{beat}} f_{\text{rep}} + f_{\text{ceo}}}_{\text{closest comb mode to reference}} - \nu_{\text{ref}}. \tag{2.31}$$

The beat note is then phase-locked to an RF reference, which results in a transfer between the coherence of the optical reference to one of the comb modes.

This method requires stabilization of f_{ceo} to generate the comb structure, even for the DFG comb ($f_{\text{ceo}} = 0$), as the heterodyne beat stabilizes one comb mode. The error signal for f_{ceo} is usually generated by self-referencing the comb via a *f-2f* interferometer [76] using an octave spanning spectra. Such spectral coverage is usually achieved via nonlinear broadening of the pulses [77]. When carefully designed, the process is coherent and the comb structure is preserved [50]. The procedure consists in using a comb line, with index n, and frequency $\nu_n = n f_{\text{rep}} + f_{\text{ceo}}$, and frequency doubled it to generate $2\nu_n = 2(n f_{\text{rep}} + f_{\text{ceo}})$. On the high frequency of the spectrum, a comb line with index $2n$ and frequency $\nu_{2n} = 2n f_{\text{rep}} + f_{\text{ceo}}$ is filtered for the heterodyne optical beat between these two lines, which results in the f_{ceo} signal by:

$$\begin{gathered}2\nu_n - \nu_{2n} = \\ (2nf_{\text{rep}} + 2f_{\text{ceo}}) - (2nf_{\text{rep}} + f_{\text{ceo}}) = f_{\text{ceo}}.\end{gathered} \tag{2.32}$$

The beat note is phase-locked to the radio frequency (RF) reference, similar to the beat note in the repetition rate stabilization.

The periodic frequency structure provides several advantages for spectroscopy. In cavity enhanced methods, comb modes can be coupled to optical cavities and enhance the bandwidth of light transmitted [78, 79]. Other techniques rely on the mismatch between comb and cavity free spectral range [80, 81] to perform fast acquisition of spectra. These techniques profit from the precise spacing of the comb but often lose the absolute frequency calibration provided by the comb. Frequency combs have been applied to precision measurements in combination with the CW cavity ring-down technique. The comb provides frequency calibration and accuracy for the probe laser [82, 83]. In a similar manner, phase-lock between quantum cascade lasers to femtosecond frequency combs have been demonstrated [84]. Dual-comb spectroscopy is a technique that shares the FTS principles and can achieve fast acquisition times. Instead of interfering two pulses from the same source as in FTS, dual-comb uses two phase stable frequency combs with slightly different repetition rates [85, 86].

Independent of the spectroscopy technique, there is always a compromise between requirements and feasibility. It commonly involves resolution, acquisition time, signal-to-noise ratio, bandwidth, tuning range, accuracy, and sensitivity. Fourier transform spectroscopy is recognized for offering broadband acquisition at high-resolutions and signal-to-noise ratio. The femtosecond frequency comb strengthen the resolution and incorporates frequency accuracy as will be discussed in the following sections.

2.5 Frequency comb based Fourier transform spectroscopy

Fourier transform spectroscopy is performed traditionally with incoherent light from thermal sources [28]. Ultra-short laser pulses offer coherent broad-bandwidth and in combination with nonlinear frequency conversion, they offer an alternative light source for FTS. The low divergence of the laser beam facilitates the propagation through the interferometer, which is a common limitation for high-resolution FTS. In addition, the spectral brightness allows high signal-to-noise to be achieved in shorter measurement times.

The Fourier transform spectrometer is based on a Michelson interferometer, and in the simplest case it is composed by a beam splitter (BS) and two mirrors (M1 and M2), illustrated in figure 2.7. The interference signal, called interferogram, is acquired in function of the optical path difference (OPD) between the interferometer arms, which is this illustration is equal to two times the mirror M2 displacement, $\delta = 2x$. The spectrum is generated after Fourier transformation of the interferogram .

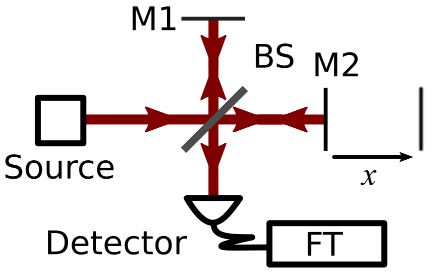

Figure 2.7: A simple FTS is composed by a Michelson interferometer. The beam splitter (BS) divides the light which goes to the interferometer arms, where the M1 is the fixed mirror and M2 the movable mirror.

For a monochromatic light source, constructive interference occurs when the OPD is an integer multiple of the wavelength, $\delta = n\lambda$, and destructive interference at $\delta = n\lambda/2$. The signal intensity, $I(\delta)$ for a monochromatic light source with intensity I_s is given by a cosine function

$$I(\delta) = I_s \cos(2\pi\delta\tilde{\nu}), \tag{2.33}$$

where $\tilde{\nu} = 1/\lambda$ is the wavenumber. As the measurement of the mirror displacement is commonly expressed in [cm] unit, the intuitive unit for frequency after FT is the wavenumber with unit [cm^{-1}].

The accuracy in measuring the OPD is directly related to the accuracy of the frequency grid. High-precision spectrometers have a reference laser propagating simultaneously with the broadband source to calibrate the OPD. The sinusoidal interferogram have well defined points at the zero-crossings ($\delta = n\lambda/2$) providing the calibration of the OPD, which is transferred to frequency after FT. The detailed role of the reference laser is discussed in section 4.9.

A broadband light source contains several optical frequencies. All components of the spectrum will interfere constructively at $\delta = 0$. The interference at this position is called central fringe, or central burst. For increasing OPD, the interference of each frequency component from the broadband spectrum occurs with different periods. The signal on the detector, integrated over all components, has the maximum signal at zero OPD and decays for longer OPD, as the frequencies interfere destructively. The spectrum and interferograms of four input spectra are illustrated in figure 2.8.

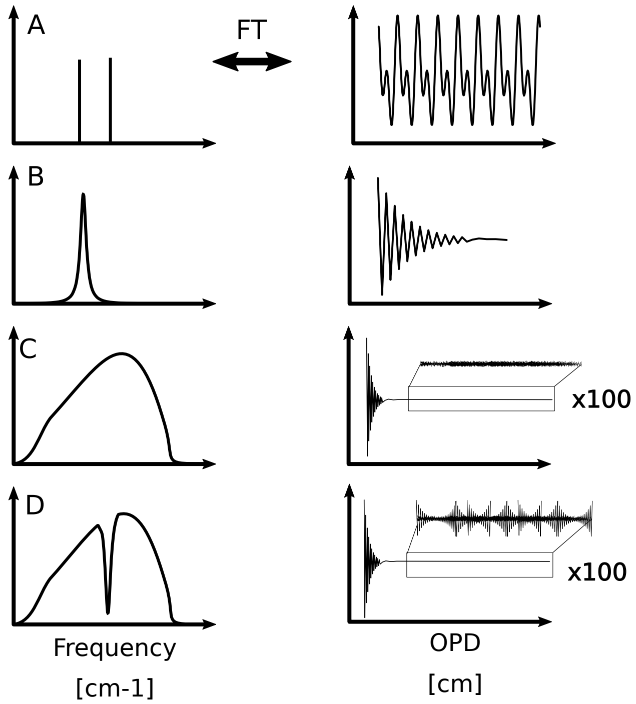

Figure 2.8: Examples of spectra and the respective single-sided interferograms. From top to bottom the interferogram of: two monochromatic lines; narrow-band spectrum; broadband spectrum; and broadband spectrum with narrow absorption feature.

Illustration A shows an emission spectra of two monochromatic lines, whose interferogram has a beating pattern which depends on the frequency separation and phase of those frequencies. A finite spectral line with a certain width, as shown in B, generates an interferogram that decays with a rate inversely proportional to the linewidth. The damping is stronger for a broader line. The interferogram of a source with broadband spectrum, shown in C, rapidly decays reaching the noise floor (illustrated by the 100 times amplification). When a narrow feature is present on a broadband spectrum, graph D, oscillations will be present and persist. Narrow features generate longer ringing in the interferogram. Graph C illustrates the importance of the signal-to-noise ratio (SNR) on the detection, specially for spectra with features, such as absorption lines. Figure 2.8 illustrates that the spectrum envelope generates a signal at short OPDs, close to the intense central fringe. The signal of spectral features are located at long OPDs, at the wings of the interferogram.

The resolution of the FTS can be intuitively illustrated considering the case of two narrow spectral lines with equal intensity and in phase. If the separation of the lines is $\Delta\tilde{\nu} = \tilde{\nu_1} - \tilde{\nu_2}$, the waves will be in phase for $\delta = (\Delta\tilde{\nu})^{-1}$ and out of phase for

$\delta = 0.5(\Delta\tilde{\nu})^{-1}$. Narrow separation between the lines require long OPD for the waves to be in-phase again, providing the required information to differentiate them. This simple picture intuitively illustrates that the resolution of the FTS, $\Delta\tilde{\nu}$, is inversely proportional to the maximum OPD, represented by Δ_{max}:

$$\Delta\tilde{\nu} = (\Delta_{\text{max}})^{-1}. \tag{2.34}$$

In fact, the FTS resolution has multiple definitions, for example the Rayleigh criteria or the full-width at half-maximum (FWHM) criteria [28]. Nevertheless, equation 2.34 is commonly employed in the literature to specify the FTS resolution and it is known as the nominal resolution, which will be the term employed throughout this thesis.

The interferogram has a finite length and it is digitized to be processed with a computer. Mathematically, the finite length of the interferogram can be interpreted as a multiplication between an interferogram $I(\delta)$ recorded from $-\infty$ to $+\infty$ with a function $D(\delta)$, limiting the interferogram from $-\Delta$ to $+\Delta$ Limiting the sampling between $-\Delta$ to $+\Delta$ is mathematically equivalent to multiply the interferogram by the boxcar type function

$$\begin{aligned} D(\delta) &= 1 \qquad \text{if } \; -\Delta \leq \delta \leq +\Delta \\ D(\delta) &= 0 \qquad \text{if } \; \delta > |\Delta|. \end{aligned} \tag{2.35}$$

The effect of multiplying two functions before FT represents a convolution of the FT of each separated function. The FT of the interferogram $I(\delta)$ is the spectrum $B(\tilde{\nu})$. The FT of the boxcar function $D(\delta)$ is $f(\tilde{\nu})$, represented by

$$\begin{aligned} f(\tilde{\nu}) =& \frac{2\Delta \sin(2\pi\tilde{\nu}\Delta)}{2\pi\tilde{\nu}\Delta} \\ \equiv& 2\Delta \mathrm{sinc}(2\pi\tilde{\nu}\Delta). \end{aligned} \tag{2.36}$$

The FT of the function that limits the interferogram is called instrument line shape (ILS) function. The ILS is present in all measurement devices and becomes visible when measuring a feature, i.e spectral lines, narrower than the resolution of the equipment. In the extreme case, the ILS is a convolution between a delta function and the instrument response function. In FTS, the instrument function can be chosen by selecting functions other than the boxcar to limit the interferogram. This process is called apodization [28, 87]. Top row of figure 2.9 illustrates four apodization functions, $D(\delta)$, and their respective Fourier transformation, $f(\tilde{\nu})$. The left panels show the apodization functions for $\delta = 2\Delta$. In a typical measurement several data points exists ($\approx 10^6$) from $-\Delta$ to Δ. The interference signal is not shown in this illustration, which can be considered a sine wave for simplicity. The right panels show the FT of the sine wave truncated by the functions shown in the left panels. The frequency grid is shifted to have the sine wave frequency at $1/\Delta = 0$. The legend shows the FWHM ($\Delta\tilde{\nu}_{1/2}$) values of the ILS functions. Although the nominal resolution introduced in equation 2.34 provides a good idea on the resolution limit of the FTS, the apodization of the interferogram dictates its effective resolution.

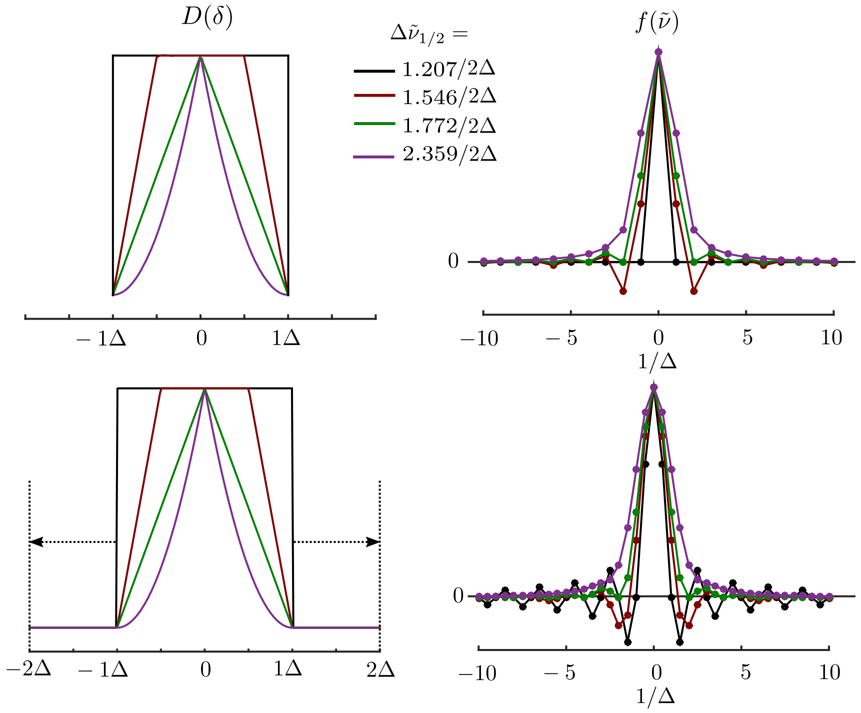

Figure 2.9: Four apodization functions and their Fourier transformation without (top) and with (bottom) zero padding. Black: boxcar; red: trapezoidal; green: triangular; and blue: triangular squared.

Bottom row of figure 2.9 illustrates an additional concept in FTS, called zero-padding, which is performed by adding zeros in the interferogram. Zero-padding is employed to generate linear interpolation in the spectrum [28], which makes the ILS clearer to be observed on the bottom of figure 2.9. The top graphs have no zero-padding and the bottom graph shows zero-padding from $-\Delta$ to -2Δ, and Δ to 2Δ. Despite having intense oscillations on the side lobes, the boxcar function gives the narrowest FWHM and it is usually applied in high-resolution FTS. In order to measure a spectral feature with negligible distortion caused by the ILS, it is necessary to have the nominal resolution three to four times higher than width of the spectral feature [28]. Typical absorption line widths at the Doppler limit are in the range of 150 MHz, which would require nominal resolution of 50 MHz ($\tilde{\nu} \approx 0.0016$ cm^{-1} or OPD ≈ 6m).

The generation of the optical spectrum from the interferogram requires calculations, which provide FTS mathematical tools. One of the advantages is the ability to control the data points in the spectrum by choosing the interferogram length (equation 2.34), especially in combination with frequency combs, due to the equally spaced comb modes. The combination between these two techniques and the advantages will be described later in this chapter.

2.5.1 High-performance Fourier transform spectroscopy

Performing spectroscopy with high resolution, high SNR and high precision is challenging and requires careful design of the spectrometer. One of factors that limit high-resolution FTS is the divergence of the beam. The OPD experienced by the center and the extremes of a divergent beam is different due to the wavefront curvature. Figure 2.10 illustrates the effect of a divergence beam passing through an interferometer and the effect on the interferogram for a monochromatic light source.

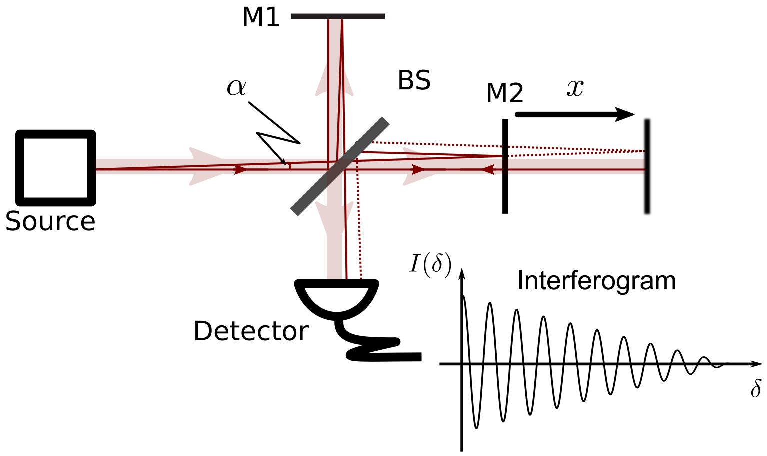

Figure 2.10: Illustration of a Michelson interferometer showing the influence of the divergence angle α on the interferogram of CW laser for a displacement x in the moving mirror.

The effect on the retrieved spectrum is known as self-apodization, and yet another convolution of the spectrum with a response function, which depends on the geometrical arrangement [28]. In the interferometer shown in figure 2.10, for a beam with divergence half-angle, α, and a mirror displacement, x, it is possible to show that the extremes of the beam experiences a displacement [28]

$$x' = x\alpha^2. \tag{2.37}$$

The extremes of the beam will be out of phase with the center when $x' = \frac{1}{2}\lambda$ and at this point no interference can be observed anymore. The distance x' sets the limit for the maximum resolution $\Delta\tilde{\nu} = (2x')^{-1}$ at a particular divergence half-angle. The maximum angle, α_{max}, accepted to acquire a spectrum at $\Delta\tilde{\nu}$ resolution, with $\tilde{\nu}_{\text{max}}$ as the highest wavenumber is

$$\alpha_{max} = \left(\frac{\Delta\tilde{\nu}}{\tilde{\nu}_{\text{max}}}\right)^{1/2}. \tag{2.38}$$

In interferometers using spatially incoherent light sources, an aperture is placed in front of the detector to limit the beam divergence passing through the spectrometer, which is in the range of 1 mm for resolution on the 30 MHz range [27]. This limits the amount of light reaching the detector and poses a challenge to perform high-resolution spectra.

In addition to the self-apodization, the divergence causes a shift on the frequency grid. The extreme rays experiences a higher OPD change than the center of the beam $\delta' = \delta/\cos\alpha$. As a result, the extreme portions of the beam will generate an interference signal with lower frequency than the center of the beam. Although the precision will not be affected, the frequency accuracy will be lost. A similar frequency shift is caused by a misalignment between the reference laser and the probe beam. The frequency shift effect (for both divergence and misalignment) can be corrected in the data processing. On the other hand, correcting the self-apodization is not trivial because it depends highly on the geometrical arrangement of the system, which is in practice not as simple as illustrated by figure 2.10.

Laser light provides great advantages for FT spectroscopy due to the small divergence angle. In addition, the spectral brightness significantly reduces averaging times to achieve high SNR. In FTS, the SNR in the time domain is obtained by the ratio between the amplitude of the central fringe (usually several Volts) and the standard deviation of the noise in the wings of the interferogram (in the mV range for a SNR of 1000). The SNR in the spectrum (SNR_s) can be, in principle, approximated to the SNR in the interferogram (SNR_i): $\text{SNR}_\text{s} = \text{SNR}_\text{i}/\sqrt{M}$, where M is the number of resolution elements [28].

An alternative procedure is to take the ratio between spectra, which in the perfect case the spectra are equal and ratio is equal to one. However, the system is affected by noise from electrical components and noise from the light source. e.g. amplitude noise, spectrum variation. The reciprocal value of the standard deviation over a certain spectral range corresponds the SNR measured at the spectrum (SNR_std). This is a useful way to analyze the stability of the system, for example, by comparing spectral changes over a series of measurements (as show in section 4.10.5).

2.5.2 Sub-nominal resolution

The periodicity of the frequency comb and its narrow linewidth, can be combined with FTS to measure spectral features that are narrower than the nominal resolution of the FTS without the influence of the ILS. This combination is referred to as the sub-nominal method [88, 89]. The method is described in this section.

The interferogram of mode-locked lasers is composed by the central fringe at $\delta = 0$ and consecutive fringes at OPD multiples of c/f_{rep}, where c is the speed of light and f_{rep} the repetition rate of the laser. The periodicity of the pulse train generates a periodic interferogram, in which all spectroscopy information lies between two central fringes. This is illustrated in figure 2.11.

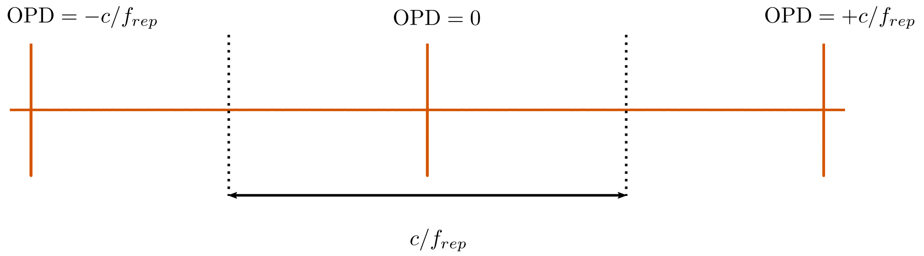

Figure 2.11: Interferogram of a mode-locked laser when the OPD is scanned through multiple interference fringes between pulse n and pulses $n-1$, n and $n+1$.

The spectrum of frequency combs is composed by comb modes separated by f_{rep} and the spacing between them has zero intensity. For this reason, increasing the OPD, i.e. the FTS nominal resolution beyond the comb spacing does not add spectral information. It generates large amounts of unnecessary data, which increases file sizes and data processing times. The SNR is depreciated as well because additional noise is recorded with no increase in information. It is therefore sufficient to sample the spectrum on the top of the comb modes, recording the interferogram with an OPD $\delta = c/f_{\text{rep}}$.

It is convenient to record the interferogram symmetrically around the central fringe to avoid the need for phase correction in the data processing [28]. The result is a double-sided interferogram, acquired at an equal number of sampling points on each side of the interferogram, with the central fringe at the center. The corresponding OPD can be calculated from a total number of points, N_0, on the interferogram sampled at $\lambda_{\text{ref}}/2$ steps

$$N_0 = \text{round}\left(\frac{2c}{\lambda_{\text{ref}} f_{\text{rep}}}\right). \tag{2.39}$$

The interferometer length has to be matched to c/f_{rep} precisely, for the frequency spacing to be $\Delta\tilde{\nu} = f_{\text{rep}}/c$. The OPD is calibrated using the sine wave interferogram of the reference laser with known wavelength λ_{ref}. As the MIR interferogram is resampled at $\lambda_{\text{rep}}/2$ equidistant steps, it is not possible to change arbitrarily $\Delta\tilde{\nu}$. After FT, the frequency grid is spaced by:

$$f_{\text{FTS}} = \frac{c}{\Delta_{\text{max}}} = \frac{2c}{\lambda_{\text{ref}} N_0} \quad \text{[Hz]}, \tag{2.40}$$

which leads to a FTS frequency grid $\nu_{\text{FTS}}(n)$ that can be indexed by an integer n and the FTS frequency spacing, $\nu_{\text{FTS}}(n) = n f_{\text{FTS}}$.

The elegance of acquiring using the sub-nominal resolution is that instead of increasing the resolution to remove the ILS influence on the spectrum, the periodicity of the function is adjusted to match the frequency comb grid. In such a scenario, the convolution occurs at the points that the ILS changes signs, i.e. the ILS crosses zero. Figure 2.12 illustrates two scenarios. On the left, the comb spacing is smaller than the FTS nominal resolution ($f_{\text{comb}} > f_{\text{FTS}}$), on the right, the perfect match ($f_{\text{comb}} = f_{\text{FTS}}$). An absorption feature narrower than the comb spacing is illustrated on the top. In the presence of an absorption feature, the measured spectrum is a convolution between ILS and the spectrum. The frequency comb is shown below the absorption line represented by the black lines. The amplitude of one comb line is decreased due to the absorption feature. The doted lines show the comb and FTS grid. The red curve illustrated the convolution between the ILS and the second sampling point. The blue curve shows the convolution for the fifth sampling point. The absorption is represented by the missing area in the ILS caused by the absorbed comb mode. On the left, the grids do not match and the result of the convolution between the ILS and the absorption feature at that point affects the spectrum, and the total ILS area is reduced. It causes the second sampling point to be affected by the absorption. On the right, it is possible to see that at the same point, the result of the convolution results in no area change and the spectrum is not affected. The blue curve shows the effect under the absorption line. On the left, it is possible to see that the mismatch between the grids causes a distorted line and it broadens the absorption feature. On the right, the correct line position is retrieved without influence of the ILS in the final spectrum.

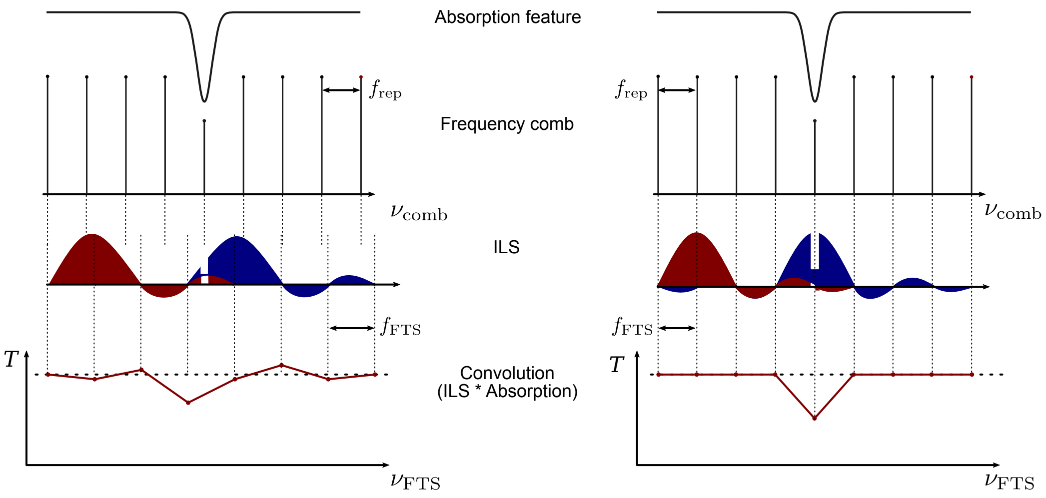

Figure 2.12: Absorption spectra acquired with different ratio between comb and FTS grids. Left: the FTS nominal resolution is smaller than the frequency comb spacing. Right: the FTS nominal resolution matched the frequency comb spacing. From top to bottom: a narrow absorption feature; the amplitude of one comb mode is decreased due to the absorption feature; the convolution between the ILS and the second sampling point (red), the fifth sampling point (blue); the resulting spectra with (right) and without (left) influence of the ILS.

The shape of the ILS is given by the apodization function and the periodicity is given by the nominal resolution of the FTS, which needs to be adjusted. The smallest change in f_{FTS} is obtained by changing N_0 by two points, removing one point at each side of the interferogram. This minimum frequency change is not always sufficient to precisely match ν_{FTS} with the frequency comb grid ν_{comb}. The consequence of a frequency difference between the FTS grid and the frequency comb grid is an observable effect of the ILS in the absorption feature. One effect is the clear ILS oscillation, in the form of a *sinc* function for a boxcar truncation. A second effect is the broadening of the absorption feature due to the convolution between the absorption feature and the ILS. To reduce the minimum frequency change in f_{FTS}, it is possible to apply zero-padding on the interferogram by a factor k_{pad}. This is accomplished by adding zeros to the measured interferogram, which changes equation 2.40:

$$f_{\mathrm{FTS}} = \frac{2c}{\lambda_{\mathrm{ref}} N_0 (k_{\mathrm{pad}} + 1)}. \tag{2.41}$$

The frequency shift required to adjust the FTS grid to the comb grid is smaller when the frequency grids are closer to each other. Smaller shifts of the FTS grid require larger padding factors. In principle it is possible to use only the padding to match the grids over the complete optical bandwidth covered by frequency comb spectrum. However, padding greatly increases computational time and still only permits a coarse adjustment of the frequency grid.

The FT grid starts at zero frequency, which might not be the case for the frequency comb ($f_{\text{ceo}} \neq 0$). In this situation, it is necessary to shift the FT frequency grid to start at a non zero frequency value. To include a frequency shift on the FT scale by a fraction of f_{rep}, the interferogram $I(\delta)$ is multiplied by an exponential function to add a f_{shift} to the FT grid:

$$I(\delta) = \exp(-i2\pi\delta f_{\text{shift}}/c). \tag{2.42}$$

The resulting FTS grid is $\nu_{\text{FTS}} = nf_{\text{FTS}} + f_{\text{shift}}$. Small differences between the comb and FTS frequency grid can be compensated by the shift as well. In the case the grids have different spacing ($f_{\text{FTS}} \neq f_{\text{rep}}$), the shift of the FT grid can be applied to achieve a local agreement between ν_{FTS} and ν_{comb}.

To complete the sampling in spectral regions between the comb modes, the frequency comb structure can be shifted by a fraction of the repetition rate using f_{rep} or f_{ceo}. The final spectrum is generated by interleaving spectra measure with different comb grids and sampled at different $\Delta\tilde{\nu}$ values. The ability to control the comb frequency and its narrow linewidth limits the final density of sampling points and it provides a tool to acquire information beyond the OPD limit of conventional FTS [89, 88]. Figure 2.13 shows the an example, with the measurement performed in CO at 0.2 mbar with interleaving steps of 30 MHz. The linewidth is Doppler limited at 150 MHz and the FTS nominal resolution is 150 MHz.

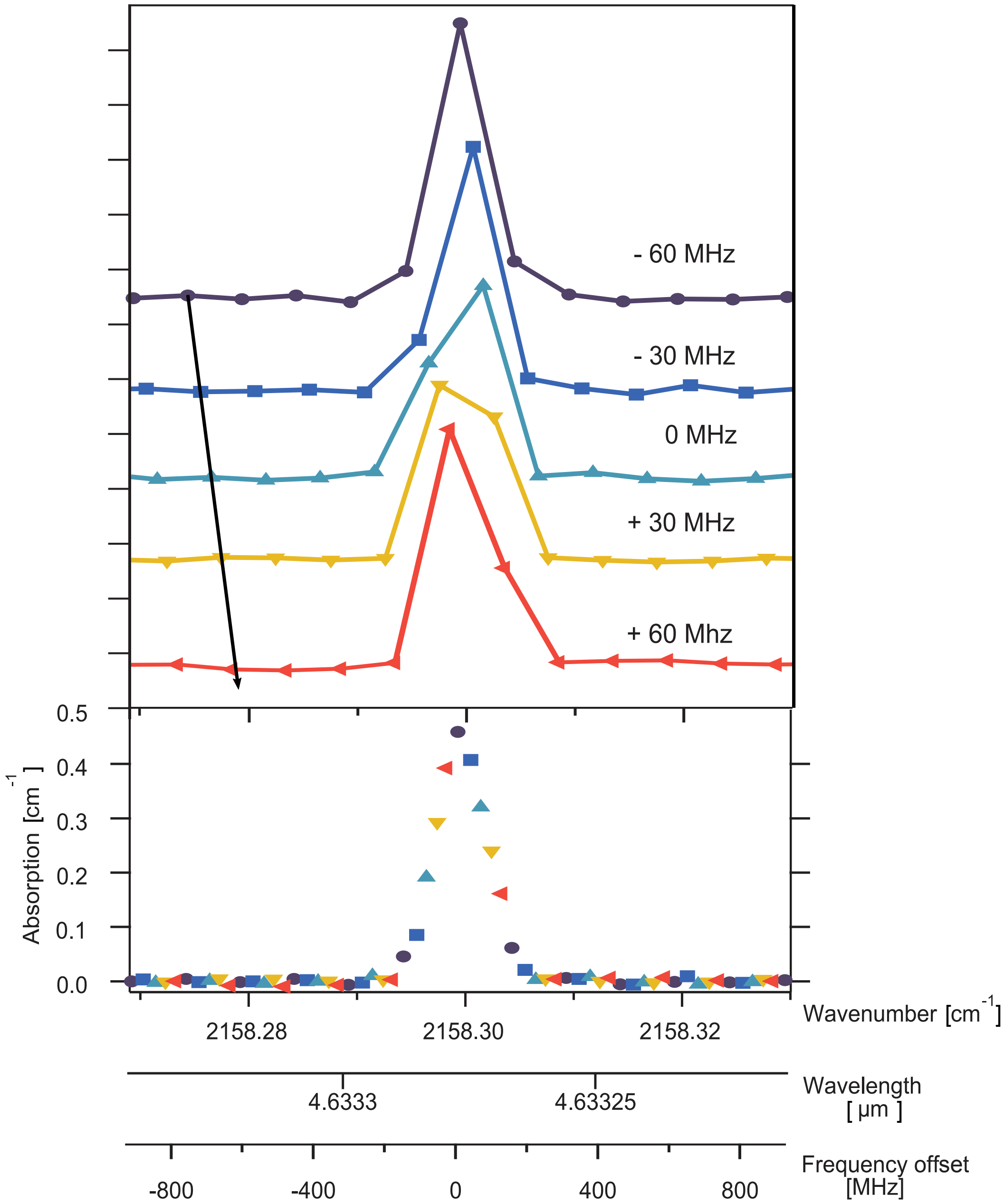

Figure 2.13: Carbon monoxide R(3) line acquired with sub-nominal resolution interleaving measurements with 30 *MHz steps of the comb modes. The Doppler limited linewidth is* 150 *MHz which is similar to the frequency comb spacing.*

3 Mid-infrared laser source

The light source was designed with the intention to cover part of the MIR that includes CO and CH absorption bands. Light from the frequency comb at 1050 nm is converted to the spectral range between 3 and 5 µm. The frequency conversion is performed by difference frequency generation, which is a widely explored technique to generate broadband optical pulses with adjustable output spectrum [39].

This chapter presents modification and optimization of the laser source aiming the acquisition of high SNR spectrum of CO.

3.1 Laser source

The MIR frequency comb is generated based on the system illustrated in figure 3.1. The oscillator, amplifiers 2 and 3 were available in the beginning of the project. Phase stabilization was modified and components included to attend the demands of experiments performed in the thesis, specially for the scanning of the repetition rate. The amplifier 1 and the DFG were included in the system during this project.

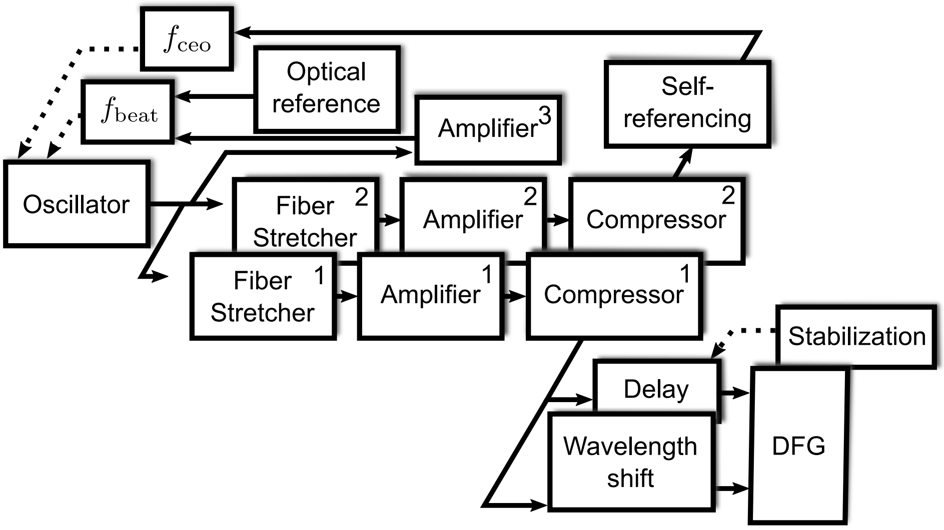

Figure 3.1: Diagram of the laser system used for the difference frequency generation stage, showing the oscillator stabilization, the amplifiers and the DFG setup.

The output of the oscillator is separated for the optical beat, the self-referencing, and the difference frequency generation, each one passing through an amplification stage. Amplification chain number 1 deliver pulses for the MIR generation. Amplification chain number 2 deliver pulses for the self-referencing stage, which is responsible for f_{ceo} stabilization. The amplifier 3 is required for the optical heterodyne beat between the oscillator and the optical reference. Amplifiers 1 and 2 are based on cladding pumped gain fibers, amplifier 3 is based on core-pumped gain fiber.

Two amplification chains provide the ability to optimize the pulse compression individually at two instances of frequency conversion that are critical for the system performance. In addition, two amplifiers is a simple solution compared to the alternative of having one amplifier with double the output power. One instance of frequency conversion is the highly-nonlinear fiber responsible for the octave spanning spectrum in the self-referencing stage. The second, is the highly-nonlinear fiber that provides the wavelength shift in the DFG (which will be discussed in section 3.2.3). Coherence degradation between multiple amplification chains has been studied by several groups [90, 91]. It has been demonstrated that additional noise arises mostly from non-common optical path and acoustic vibrations of optical components. Distinct amplification chains and frequency conversion stages (e.g. second harmonic generation, nonlinear broadening in optical fibers) does not contribute to coherence degradation of the optical fields.

Ytterbium doped fibers are the gain media for oscillator and amplifiers. Ytterbium offers advantages among other doping materials in fiber laser materials, especially for high-gain and high-repetition rate applications [92]. The oscillator is based on a Fabry-Perot type cavity, working in the similariton regime with a saturable absorber mirror for self-starting mode-lock [93], and it is a similar laser as reported in Ref. [50]. It has a repetition rate of 150 MHz and generates approximately 100 mW of output power, with 60 fs FWHM bandwidth-limited pulse duration estimated from the spectral bandwidth. The amplification chain 1 and 2 are based on chirped pulse amplification [94]. The pulses are temporally stretched in a dispersion compensating fiber, amplified, and then compressed using a pair of transmission gratings. Amplification chains 1 and 2 provide each compressed pulses with approximately FWHM pulse durations of 130 fs and operate at 1.5 W output power.

3.1.1 Amplifier

Chirped pulse amplification is employed using a fiber stretcher and a pair of transmission gratings. The setup is illustrated in figure 3.2. Pulses are temporally stretched to avoid nonlinear effects during amplification. The compression is performed by gratings due to the required amount of dispersion to be compensated. Conventional fibers have second order dispersion sign opposite to the grating compressor and can be fully compensated. On the other hand, conventional fibers and gratings have equal sign of third order dispersion. For the pulse to be compressed to the shortest duration, third order needs to be taken into account. The dispersion compensating fiber (optical fiber stretcher by OFS Specialty Photonics) is a crucial component in this system. It adds third order dispersion of the correct sign that is compensated by the compressor. The amount of fiber can only be estimated due to the lack of accurate dispersion data and requires experimental optimization in several steps. The pulse duration is minimized by careful balance between second and third order terms using frequency-resolved optical gating (FROG).

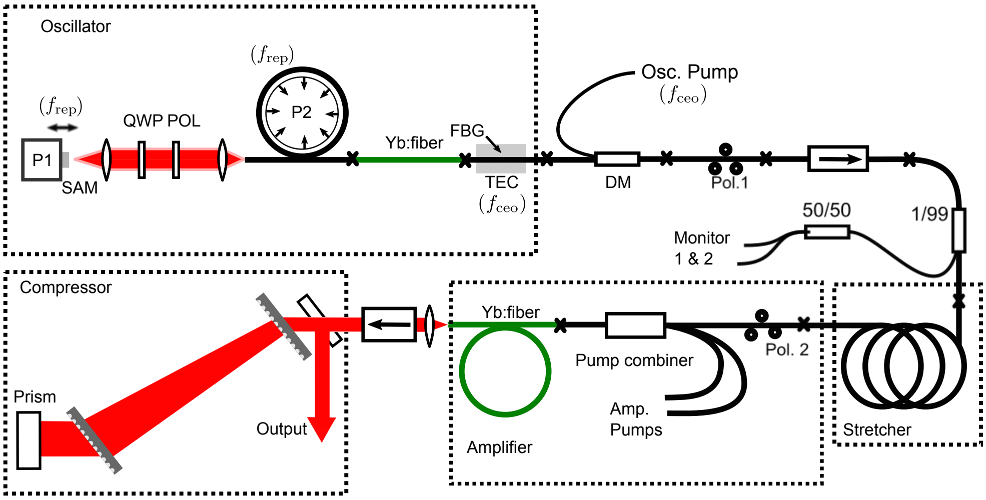

Figure 3.2: Schematic drawing of the main components of the laser source from oscillator to compression. The drawing shows in separated areas the oscillator, stretcher, amplifier and compression.

Several tests were performed with different gain fibers to build amplifier 1. Stretching and compression stages were tested to find an optimum amplification and the shortest pulse duration. The gain fiber of amplifier 2 has custom specifications from previous work from the group and it is not commercially available. The length of the custom fiber in amplifier 2 is 0.7 cm. Amplifier 1 uses a commercial product (nLight - Yb1200-20/125DC) with length 3.5 m. Longer gain fiber required more stretching ratio to avoid nonlinear effects during the amplification. In addition, a different grating compressor was designed to compensate for the extra dispersion. The pulses were characterized using frequency resolved optical gating [95, 96]. Figure 3.3 shows the results from the optimized pulse compression at the output of the amplifier 1. The average output power is 1.5 W and the FWHM pulse duration is 130 fs.

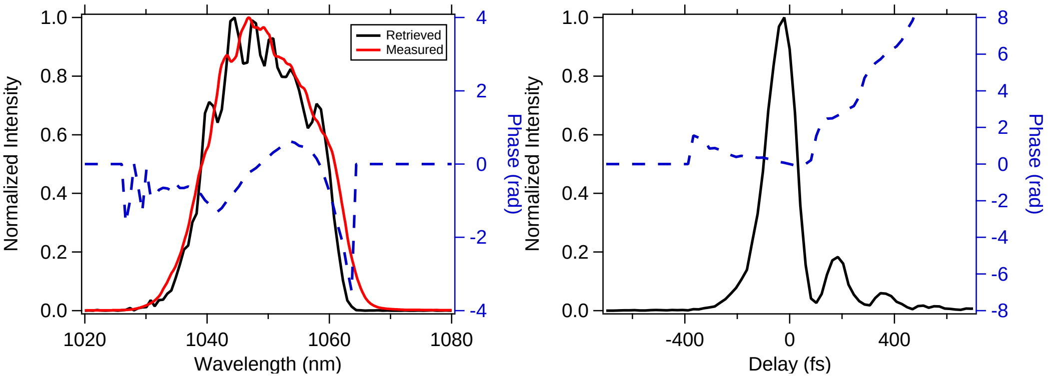

Figure 3.3: Pulse characterization results obtained by frequency resolved optical gating. Left: the measured spectrum using a spectrometer and the comparison with the retrieved spectrum and phase. Right: retrieved pulse in time domain. The compressed pulses have 130 *fs duration.*

3.1.2 Oscillator stabilization

The oscillator is stabilized via phase-locked loops (PLLs) to frequency references to generate a frequency comb. As discussed in section 2.4, the full comb structure in optical domain has two degrees of freedom controlled by the repetition rate (f_{rep}) and the carrier-to-envelope offset frequency (f_{ceo}). Different techniques are available to stabilize oscillators to RF references [75]. The oscillator in this thesis has two actuators for each comb parameter, due to the compromise between actuator speed and actuation range. Figure 3.4 shows the schematic drawing of the oscillator.

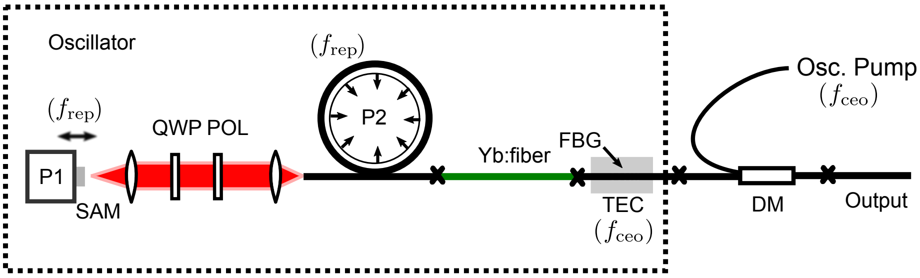

Figure 3.4: Sketch of the fiber laser oscillator. f_{rep} *and* f_0 *indicate the controls used for stabilizing the laser. P1: linear piezoelectric element; SAM: saturable absorber mirror; P2: piezoelectric ring; TEC: thermoelectric controller; FBG: fiber Bragg grating. WDM: wavelength division multiplexer.*

Optical heterodyne detection is performed to obtain the error signal for the phase lock of one of the comb modes to the optical reference [70]. The optical reference is a commercial single frequency laser (Coherent Mephisto). The signal of the beat note is generated by the comb mode closest to the reference laser. The oscillator spectrum is filtered and superimposed with the reference laser, generating the beat note whose phase is compared with the RF reference using a phase detector. The fast feedback is performed by a linear piezoelectric actuator (P1), moving the saturable absorber mirror at one end of the cavity. The output of the phase detector passes through proportional integral derivative (PID) loops and is applied to stabilize f_{beat} via the actuators of f_{rep}. The slow feedback is performed by the ring piezoelectric actuator (P2), which has a portion of fiber from the cavity spooled on it. Its diameter is controlled, shrinking or extending the fiber, providing a large actuation. The actuators P1 and P2 control the cavity length, and hence the repetition rate of the laser.

The detection of f_{ceo} is performed by self-referencing the comb using a f-$2f$ interferometer [76]. Similar to the f_{beat} stabilization, the f_{ceo} beat note is compared to the RF reference with a phase detector. The feedback loop is performed by the pump diode current as fast actuator (Osc. pump) and the temperature of the fiber Bragg grating as slow actuator (TEC). They both act on the laser dynamics to affect dispersion in the cavity, in effect changing the balance between group and phase velocity and controlling f_{ceo} (see equation 2.29) [75].

The oscillator phase-noise follows the phase-noise of the references. Accuracy at long and short time scales is provided by several references. The stabilization setup is illustrated in figure 3.5.

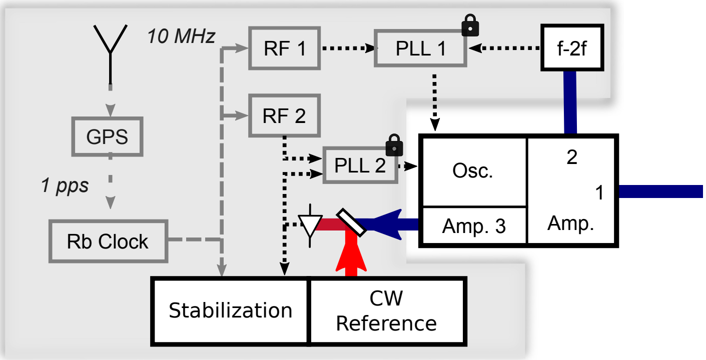

Figure 3.5: Schematic drawing of the frequency comb stabilization. The GPS provides the 1 *pulse per second reference with long term stability. The rubidium clock is referenced to this signal and provides a 10 MHz signal for the radio frequency generators (RF 1 and RF 2). The phase locked loops (PLL1 and PLL2) are used to stabilize* f_{ceo} *and* f_{beat}*. The CW reference was stabilized using two distinct approaches described later in this section.*

The long term stabilization of the radio frequency equipments is performed via the 1 pulse per second from the GPS receiver. Typical accuracy of the GPS is 10^{-12} over several days on the 1 pulse per second (PPS) level. This signal is employed as reference for a rubidium clock, which provides the 10 MHz references for the radio frequency generators (RF 1 and RF 2). The RF generators provide the references for phase-locked-loop 1 and 2 (PLL 1 and PLL 2). The accuracy on the 10 MHz signal is 10^{-11} over a second and decreases to 10^{-9} at hours without the 1 PPS reference. The optical reference provides 10^{-12} accuracy over 100 ms and requires stabilization for longer time scales. The stabilization of the optical reference is performed by the frequency comb and it is discussed in the next section.

3.1.3 Control of the comb modes

In order to perform FTS with sub-nominal resolution (discussed in section 2.5.2), the stability and accuracy of the frequency comb structure are crucial. The optical heterodyne beat between the optical reference (ν_{ref}) and the comb is applied to stabilize one of the comb modes. In combination with the f_{ceo} stabilization, the complete comb structure is fixed.

In addition to the stabilization, the comb structure needs to be controlled. It is necessary to shift the comb structure by a fraction of the repetition rate to access optical frequencies between the comb modes. It is possible to change the comb structure by controlling one out of the two comb parameters. The MIR frequency comb, however, is offset-free due to the difference frequency generation and it is not influenced by changes in f_{ceo}. Therefore, the change of the comb structure was performed by changing the optical frequency of the reference laser. Because of the PLL and the actuators applied to stabilize the f_{beat}, the change of the reference laser is transferred to a change of the comb structure via f_{rep}. A schematic drawing of the setup for locking the heterodyne beat is shown in figure 3.6.

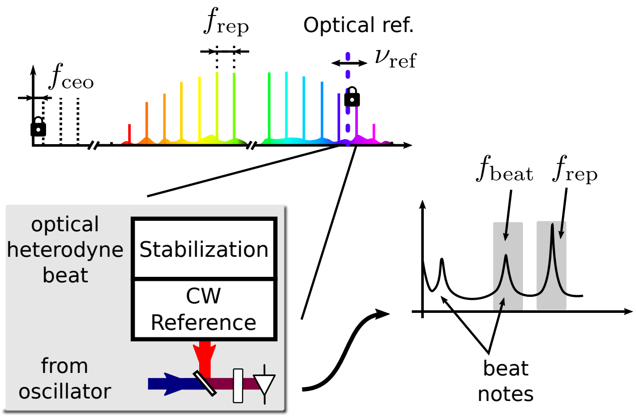

Figure 3.6: Schematic setup of the optical heterodyne beat between the reference laser and the frequency comb. The frequency comb and the relevant parameters are illustrated on the top. Light from the oscillator is superimposed with the comb generating the optical beat note.

The frequency structure is illustrated in the top of the figure together with the relevant parameters. The heterodyne beat is performed by superposing the oscillator and the optical reference. The beat note signal from the photodiode contains the repetition rate and two beats, corresponding to $\nu(n)_{\text{comb}} - \nu_{\text{ref}}$ and $\nu(n+1)_{\text{comb}} - \nu_{\text{ref}}$. One of the beat notes (f_{beat}) is filtered, amplified by low noise analog electronics and employed in the PLL.

The repetition rate (f_{rep}) is filtered and employed in the stabilization of the optical reference. Over a period of 100 ms, the optical reference has 1 kHz frequency stability. Over longer times scales, it is susceptible to fluctuations, which can be corrected using the temperature of the laser crystal and a piezoelectric actuator. Two schemes to stabilized the reference laser were tested and will be described.

Scheme 1, as shown in figure 3.7, consists in detecting the repetition rate with a frequency counter, which communicates with a computer. The PID loop is performed via software with long integration times, resulting in a feedback bandwidth of a few Hz. The feedback signal is applied to the temperature controller of the reference laser using a digital-to-analog converter.

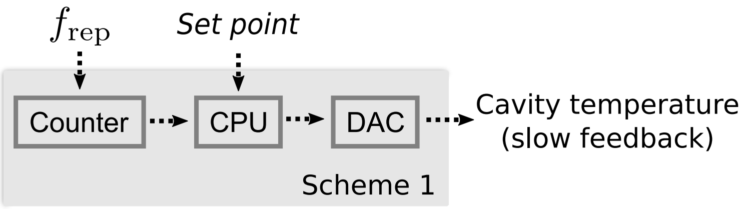

Figure 3.7: Stabilization of the optical reference via the frequency comb. The repetition rate is detected by the counter, which sends the value to a computer (CPU). The signal is compared to the set point and the slow feedback is applied to the cavity temperature of the reference laser using digital-to-analog converter (DAC).

The feedback bandwidth is limited by the temperature controller at ≈ 1 s. The effect of the slow bandwidth can be observed in figure 3.8 which shows the frequency counters monitoring the repetition rate, and the two phase-locked loops for f_{ceo} and for the heterodyne optical beat (optical beat).

The changes on the repetition rate are transferred to the comb mode multiplied by the comb number. The changes on the optical beat and f_{ceo}, on the other hand, are transferred without the multiplication and are small compared to the repetition rate deviations. The frequency counters indicate that the PLLs are stable, and that changes in repetition rate come from drifts of the reference laser frequency. The standard deviation of the repetition rate over the shown span is ≈ 100 mHz, which corresponds to 43 kHz fluctuation of the

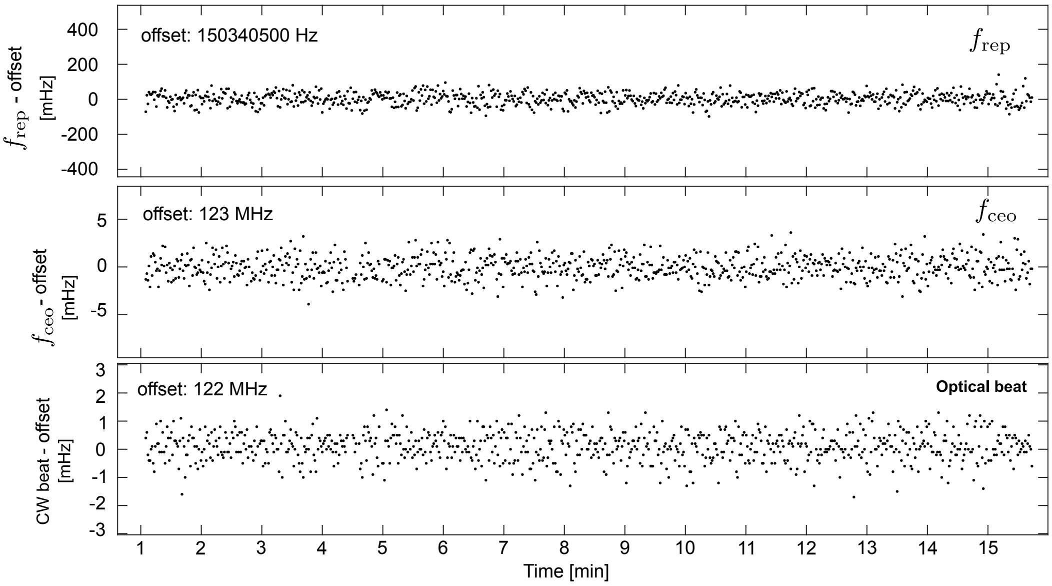

Figure 3.8: Recorded values from the frequency counters monitoring the laser stabilization using scheme 1. Top: the repetition rate; middle: the f_{ceo} beat note monitor; bottom: the optical heterodyne beat note monitor.

comb line.

Stabilization scheme 1 was applied during the experiments in section 5.3. The effect of a broad comb linewidth in the ILS is not trivial to be modeled because it involves a convolution between the absorption line, the comb and the ILS function. It was necessary to improve the stabilization to achieve a comb linewidth that can be considered infinitely small.

The second stabilization scheme is illustrated in figure 3.9. Instead of using the counter to generate the error signal, a phase-locked loop is performed between the comb repetition rate and the RF reference (RF 3). The phase detector generates a signal which is filtered using analog PID controllers (Stanford research systems - SIM960).

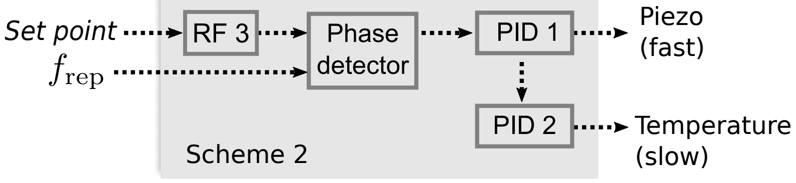

Figure 3.9: Stabilization of the optical reference via the frequency comb using a phase locked loop. The set-point value is applied in the RF reference. A phase detector compares the set-point and the repetition rate of the comb, generating the error signal. Two loop filters (PID 1 and PID2) treat the signal and feedback to the two actuators on the reference laser.

The signal from the phase detector is filtered to generate two error signals to stabilize the reference laser. The temperature controller and the piezoelectric actuator provide slow and fast feedback control over the reference laser frequency. The improvement is illustrated by figure 3.10, which shows the counter data after implementation of the third phase lock. The long term stability of the GPS is transferred to the reference laser, utilizing the comb as a link between radio and optical frequencies. The fluctuations on the repetition rate of the laser are at the resolution limit of the counter (1mHz). Such fluctuation corresponds to 400 Hz fluctuations of the comb modes at 4.6 µm. Stabilization scheme 2 was applied during the experiments in section 5.5.

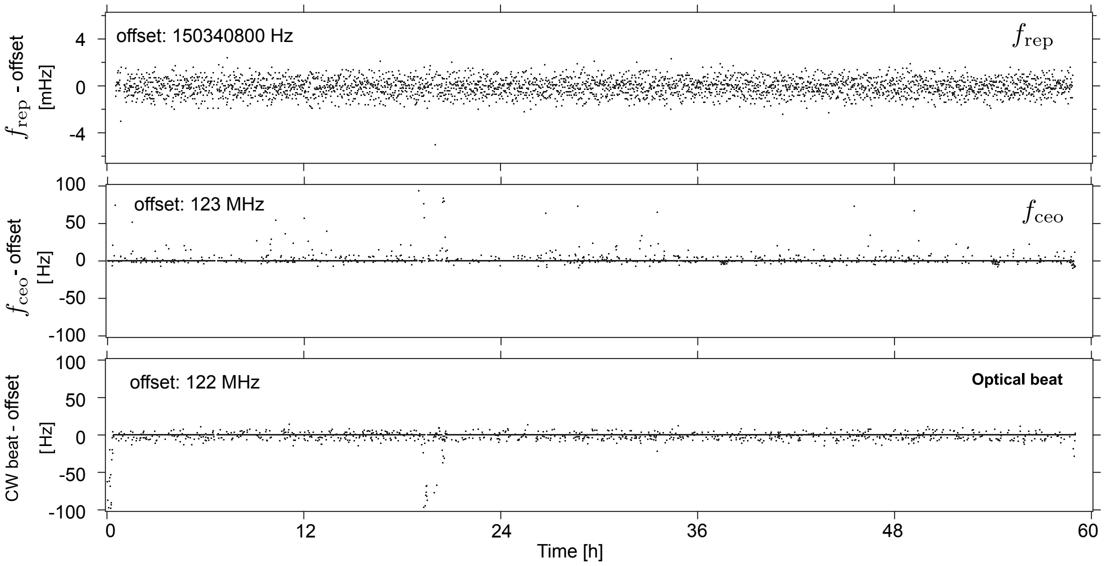

Figure 3.10: Recorded values from the frequency counters monitoring the laser stabilization using scheme 2. Top: repetition rate monitor; middle: the f_{ceo} beat note monitor; bottom: the optical heterodyne beat monitor.

The change of the reference laser frequency is now performed by adjusting the setpoint via the RF reference 3. The effect is a change of the reference laser center frequency, which changes the frequency of the heterodyne beat note. The PLL maintain the frequency of the beat note by moving the comb mode, effectively changing the repetition rate of the laser. A similar approach would be to preserve the reference laser frequency and change the frequency of the beat note. However, the frequency of the beat would change and the analog electronics treating the signal would require adjustment, which is less practical and more demanding from an experimental point of view. Figure 3.11 shows a typical measurement containing ten repetition rate scans. The graph on the left shows the counter value measuring the repetition rate. The beat note from the $f_{\rm ceo}$ and the optical lock are not disturbed by the change in the repetition rate if the rate is about 1 Hz/s (shown on the right side of the figure). During the change, it is possible to observe a small increase in noise on the optical beat but the system stays locked.

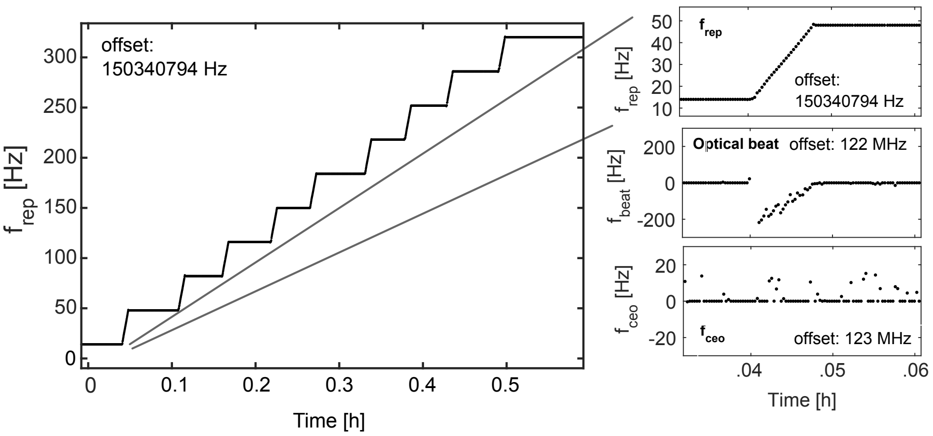

Figure 3.11: Values of the frequency counter during ten repetition rate scans. Left: Values of the frequency counter offset by 150340794 *Hz during the repetition rate scans. Right: zoom on the repetition rate during the change showing the slope, and the frequency counter values of the optical beat and the f_{ceo} beat.*

3.2 Nonlinear frequency conversion

Nonlinear frequency conversion is a powerful tool to generate laser light in spectral regions not covered by laser gain media. For the system reported in this thesis, the process occurs in a nonlinear crystal and the requirement was to be pumped at 1 µm and coverage of the mid-IR spectral region. Promising crystals that can be pumped at 1 µm wavelength are non-oxide crystals, such as GaSe, GaAs and OPGaP, which offer high nonlinear coefficients [36]. On the other hand, high birefringence and dispersion increase spatial and temporal walk-off. The advantages of using such materials are prominent when the application targets longer wavelengths (surpassing 10µm) [97].

Lithium niobate was chosen among the available crystals due to its high nonlinearity and the ability to cover the spectral region of interest. It can be periodically poled allowing quasi-phase matching and provides a transparency range that covers up to 5 µm. It is commercially available in many configurations and has been extensively studied [98, 99]. The poling periods are arrange in fan-out structure, illustrated in figure 3.12, allowing continuous adjustment of the central wavelength. Poling-periods ranging from 26.15 µm to 30.65 µm supported MIR generation from 3 to 5µm. The phase matching curve for pumping at 1050 nm is illustrated in figure 3.12

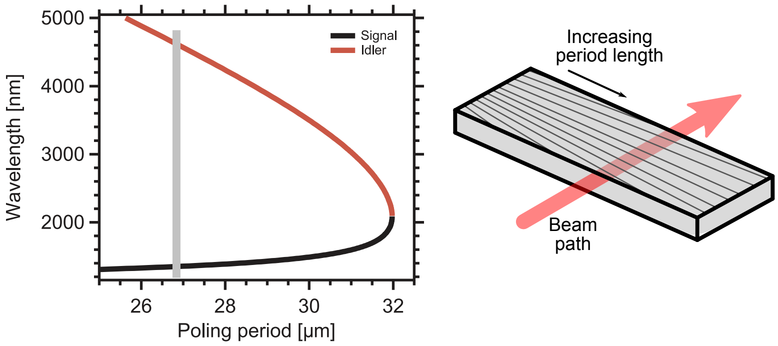

Figure 3.12: Signal and idler output versus poling period length on PPLN for 1050 *nm pump. The signal wavelength is showed in black and the idler wavelength in red. The bottom axis shows the poling period length. The gray line shows the operation: idler* 4.60µm*, signal* 1.36µm *and poling period* 26.84µm*.*

3.2.1 Difference frequency generation

Three optical fields are involved and they are named by convention, from higher to lower energy, pump, signal, and idler. Figure 3.13 illustrates the DFG, showing the interaction occurring in a single pass through the nonlinear crystal. The photon picture shows virtual energy levels and the three photons involved in the process, fulfilling energy and momentum conservation. Each pump photon generates a pair of signal and idler photons. The signal for the DFG is generated beforehand and acts as seed for the subsequent generated signal photons.

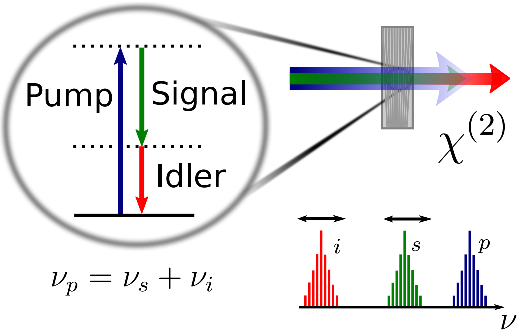

Figure 3.13: Illustration of the DFG process from different points of view. The photon picture can be represented by a two photon, non-degenerate transition between virtual energy levels. The interaction of the three fields and the non-linear media. The comb structure is maintained if pump and signal fields are coherent.

The involved fields share an equal comb structure if the coherence between pump and signal is maintained. It is possible to show with the comb equation (equation 2.30), that the idler comb is free from the influence of f_{ceo}. The comb mode number of the pump,

n_p, which generates a pair of signal with comb number n_s and idler with frequency ν_i, can be written as

$$\begin{aligned} \nu_i &= \nu_p - \nu_s \\ \nu_i &= (n_p f_{\text{rep}} + f_{\text{ceo}}) - (n_s f_{\text{rep}} + f_{\text{ceo}}) \\ \nu_i &= (n_p - n_s) f_{\text{rep}} \end{aligned} \tag{3.1}$$

Difference frequency generation can be used to generate carrier-to-envelop offset free combs [46, 100]. This offset-free frequency comb requires only the stabilization of the f_{rep}, which leads to a simplified oscillator stabilization.

From equation 3.1 it is possible to deduce that the signal generation is critical for DFG, as maintaining the coherence with the pump field is a crucial step if the comb structure is to be maintained. The generation of an offset-free comb assumes that pump and signal shares f_{rep} and f_{ceo}. For this reason, pump and signal are usually generated from one seed oscillator and broadening of the spectrum is involved [101, 102, 103].

In the DFG setup reported in this thesis, the signal is generated via soliton fission and subsequent self-frequency shift of Raman solitons [77]. Spectral broadening occurs in a highly-nonlinear fiber with suspended core geometry [104]. The input pulse is broadened and experiences temporal compression due to the propagation in the anomalous dispersion regime. The result is a high-order soliton which decays into fundamental solitons, temporally separated due to dispersion [77]. The solitons experience frequency shift due to Raman scattering while propagating through the fiber. It has been shown that for optimized fiber and laser parameters, the process generates coherent light in the form of a supercontinuum [50]. The next section describes the DFG assembly and characterization.

3.2.2 Experimental set-up

The DFG setup begins with dividing the amplified pulses into pump and signal segment, as shown in figure 3.14. The half-wave plate HWP1 and a polarizing beam splitter PBS separate the amplifier output. The pump passes trough the telescope Tl2, which provides mode-matching to the signal for an optimized interaction with the signal. The Tl2 telescope decreases the beam waist using lenses with 75 mm and 50 mm focal length. The delay line Mp1-2 is necessary to increase the beam path and it compensates the differences between pump and signal optical path. A second delay line Mp7-8 was positioned close to the recombination position. It can be controlled with a micrometer for rough adjustment and a piezoelectric stage for fine adjustment of the temporal overlap. This delay line is employed in the stabilization of the delay between pump and signal (details are described in 3.2.5).

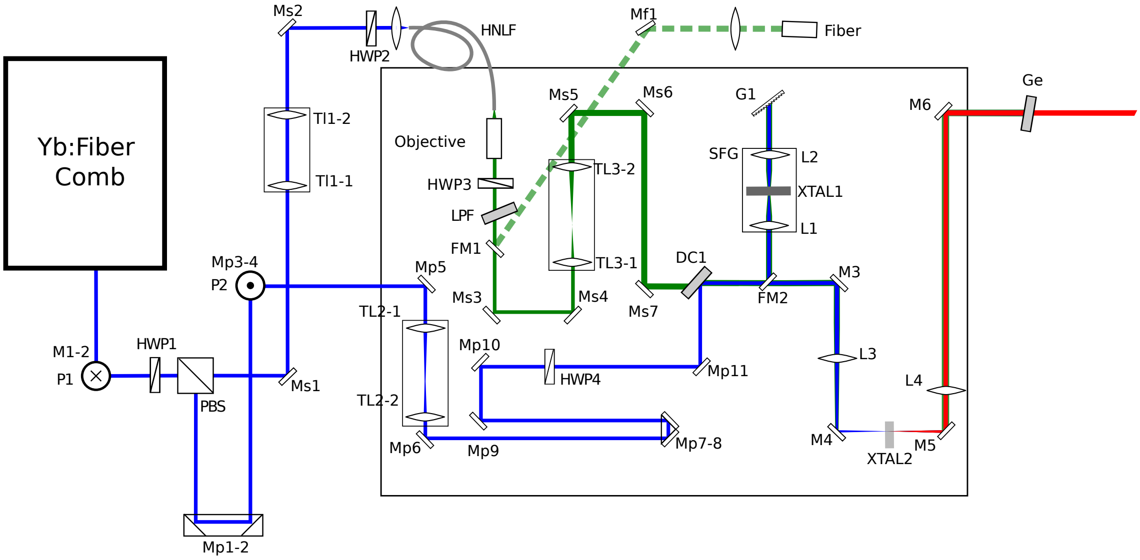

Figure 3.14: Difference frequency generation setup drawing. M: mirrors; PBS: polarizing beam splitter; HWP: half-wave plates; TL: telescopes; HNLF: highly-nonlinear fiber; DC1: dichroic mirror; FM: flip mirror; SFG: sum frequency generation; XTAL1: BBO crystal for SFG; XTAL2: PPLN for DFG; L: lenses; Ge: germanium window. The indexes s, p indicate the components for the signal and pump arms.

The signal segment is directed to the highly-nonlinear fiber. The fiber core size is ≈ 2 µm in diameter and it is surrounded by six air holes. After spectral broadening, the longer wavelength Raman soliton is filtered using a band-pass filter and used as signal. Although the remaining solitons generated in the broadening process are temporally separated, only one soliton is directed to the crystal to avoid the interaction between non-phase matched components in the DFG crystal.

The signal arm passes through the Tl1 telescope (Tl1-1 = 75 mm, Tl1-2 = 75 mm) for mode-matching to the nonlinear fiber. The optical path is around 2 m, from the amplifier output to the highly nonlinear fiber. The coupling efficiency is improved by adjusting beam divergence and size. The HWP2 waveplate before the coupling adjusts the beam polarization. The HNLF core is not symmetric and birefringent, which causes the broadening to be polarization dependent. After the nonlinear broadening, the beam is collimated by an achromatic objective lens and treated with the telescope TL3 for mode-matching, similar to the pump branch. The HWP3 (signal branch) and HWP4 (pump branch) half-wave plates are used to adjust the polarization for the nonlinear conversion. The pump and signal branches are combined collinearly using the dichroic mirror DC1.

The back side of the mirror has an anti-reflective coating for the signal wavelength and it highly-reflected coated for the pump wavelength. The combined beams are focused in the crystal using an achromatic lens with 150 mm focal length.

3.2.3 Tuning range

Raman solitons are formed at the long wavelength side from the broadband optical spectrum [77]. Depending on coupled pump power the spectrum can be shifted up to 1550 nm. This is the maximum tuning of the soliton, which limits the generation of the shortest idler wavelength at 3 μm. On the long wavelength side, crystal transparency restricts the generated idler wavelength to 5.1 μm. The output spectrum generated in the highly nonlinear fiber is shown in figure 3.15.

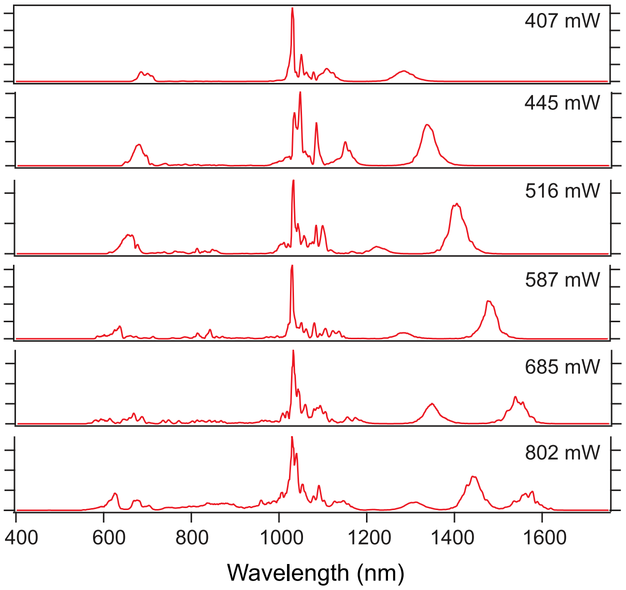

Figure 3.15: Supercontinuum output spectra from the highly-nonlinear fiber versus incident laser power.

Phase matching is achieved by choosing the correct poling period of the nonlinear crystal. Changing the signal wavelength, the poling period, and the temporal overlap allows continuous adjustment of the MIR spectrum. The MIR output spectra with respective average powers are shown in figure 3.16.

Output powers shown in figure 3.16 were not the highest achieved during the setup of the DFG stage. Optimization of the DFG output power did not lead to better performance of the system because of the quality of the output beam. Modifications were performed to improve the signal in the interferometer and they are described in the next section.

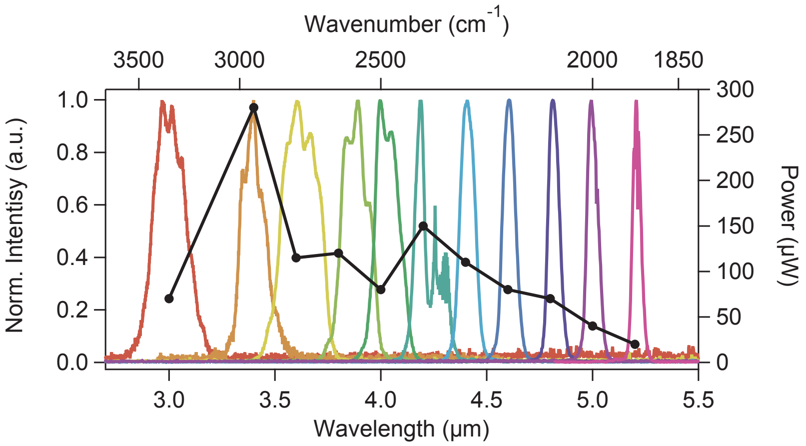

Figure 3.16: Output spectrum and output power from the difference frequency generation setup.

3.2.4 Beam quality

It was possible to achieve output powers above 1 mW at 4.6 µm. However, optimization of the interference signal suggested strong phase front distortions. The MIR beam properties are essential to acquire high quality spectroscopy data, especially in FTS as the spectrum is generated by interference. The transverse profile was heavily distorted as can be observed on the left from figure 3.17. The tight focusing of pump and signal in combination with the crystal length suggested that back conversion of idler photons could occur. The optimization on output power was performed using a lens with focal length $f = 40$ mm, which corresponds to beam waist of ≈ 30 µm. The focusing lens was replaced by a lens with $f = 250$ mm, which increased the focal spot to ≈ 200 µm. The corresponding beam profile after changing the lens is shown on the right side of figure 3.17.

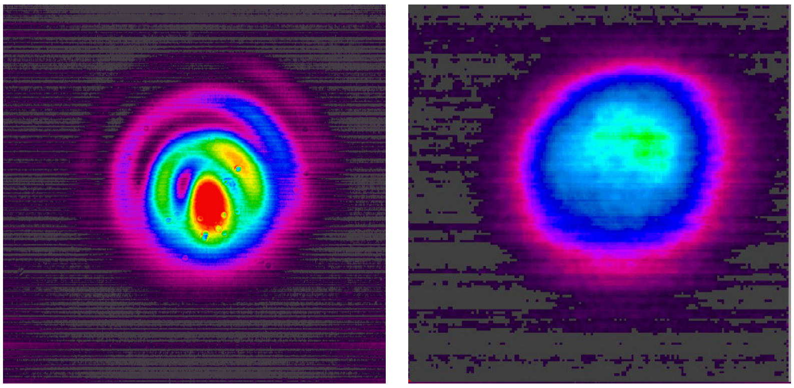

Figure 3.17: Comparison between the far-field MIR beam profiles using two different focusing lenses before DFG. Left: $f = 40$ mm. Right: $f = 250$ mm.

The MIR quality improved at the cost of output power and conversion efficiency. On the other hand, the interference signal increased even with less power because of the higher interference contrast. Further improvement in power was not necessary as the power was sufficient to saturate the detection chain (which is described in section 4.4).

As discussed in section 2.5.1, the beam divergence is important for high-resolution FTS. The beam divergence was measured using knife-edge scans at different positions over the optical path. The measurements and the fitting curve are displayed in figure 3.18.

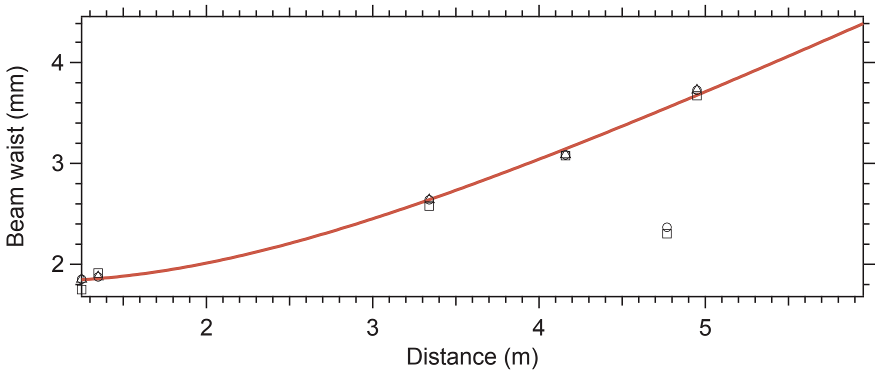

Figure 3.18: Knife-edge measurement of the MIR beam waist used to estimate the divergence of the beam.

The beam diameter was measured to be 3.5 mm at a distance corresponding to the FTS detectors position (5 m on figure 3.18). The knife-edge measurement allowed an estimation of the divergence half-angle to be 0.8 mrad. Estimation of the phase front for four wavelengths in the instantaneous bandwidth of the MIR beam at 4.6 µm is illustrated in figure 3.19. It shows the calculated wavefront curvature of four wavelengths at the detector positioned at 6 m away from the crystal. The distance is zero at the center of the beam for comparison and it illustrates how the wavefront evolves towards the edge of the beam for different wavelengths.

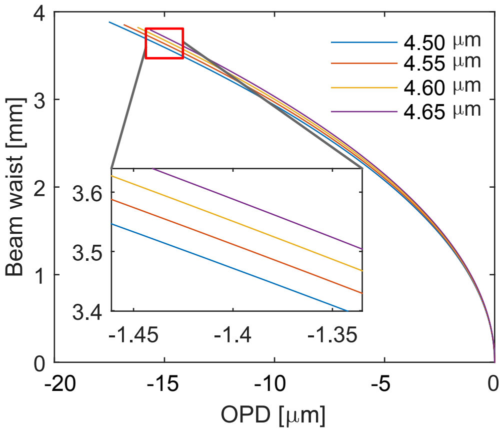

Figure 3.19: Calculated wavefront curvatures for different regions of the spectra. The effect of beam divergence is translated to a wavelength dependent OPD.

At the center of the beam the wavefronts overlap, generating a maximum interference fringe. At a radial distance of 3.5 mm, corresponding to the beam waist, the divergence causes close wavelength components to experience different OPD. For FTS, this is an important factor that contributes to decreasing the interference signal, as the interference is averaged by the detector.

3.2.5 Intensity noise in the mid-infrared source

The improved beam profile increased the interference contrast and FTS was performed with MIR radiation. In combination with the interference contrast, the average power of the MIR source contributes to the amplitude of the central fringe, as long as the detectors are not saturated. Over a sequence of measurements it was possible to observe a constant amplitude of the central fringe. However, noise with no particular periodicity was observed on the wings of the interferogram. Figure 3.20 shows multiple interferograms with the amplitude axis amplified to show the noise floor.

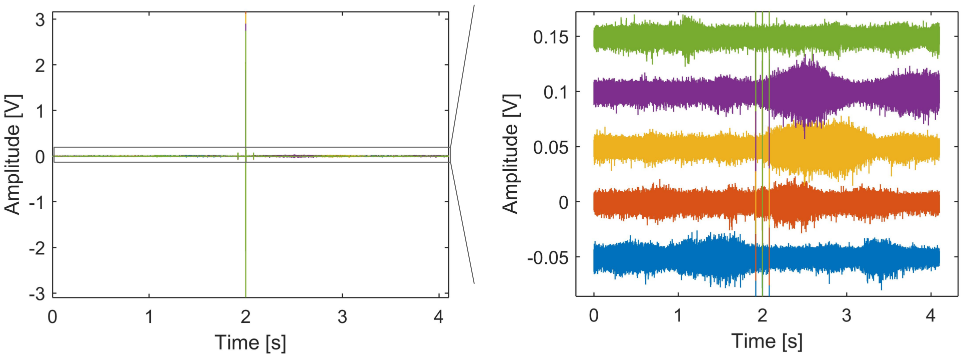

Figure 3.20: Different interferograms showing the noise observed in the baseline. The traces are offset by 50 *mV for clarity. The central fringe amplitudes are:* 6.4951, 6.4712, 6.4310, 6.4554 ,6.4789 *V.*

In order to investigate the origin of the noise, the setup illustrated in figure 3.21 was assembled. The light after DFG is filtered by a Germanium window which transmits the MIR and reflects wavelegnths below 2 µm. A long-pass filter transmits the signal and reflects the pump. An additional long-pass is used to separate the signal bandwidth being used in the DFG process and rejects the non-phase matched components, mostly second harmonics. The vector analyzer records the frequency domain signals while the oscilloscope monitors the output power of one of the spectral components. The output power of the idler depends on the temporal overlap between pump and signal and it acts as monitor of the overlap position.

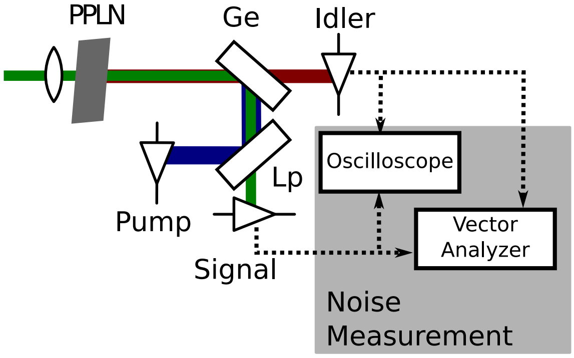

Figure 3.21: Schematic drawing of the electronic set-up to measure intensity noise of pump, signal and idler.

The relative intensity noise of the three fields is shown in figure 3.22. Noise at the signal field is comparable to the pump noise, except for slightly higher noise at acoustic frequency region. This behavior is attributed to vibrations coupled to intensity noise via the optical components responsible for coupling light into the optical fiber.

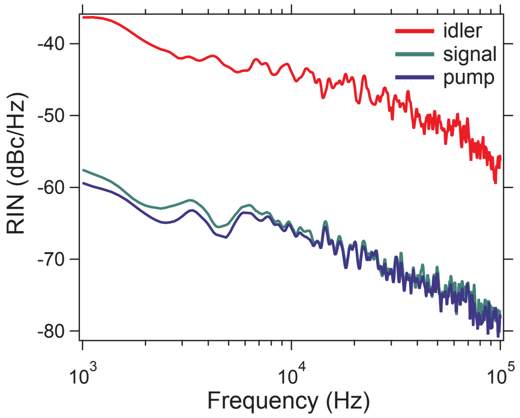

Figure 3.22: Intensity noise of pump, signal and idler.

The idler shows an increased noise behavior which can be attributed to a few factors. The extra optical path and optical components contribute to increase the idler noise. Pointing noise couples to intensity due to spatial overlap between pump and signal. Intensity noise from the signal and pump are coupled to the MIR via the nonlinear process and the overall noise of the MIR is higher [105, 106].

Much stronger dependence of the MIR noise on the temporal overlap between pump and signal was observed. The pumo/signal overlap range of minimum noise in the MIR is observed within a few fs. Measuring the absolute position and the length scale in which this effect occurs is challenging. Passive stability of delay line is not sufficient to maintain the position for a time long enough for measurements do be performed. In order to quantify the noise and to investigate its origin, a fast method to measure integrated noise power was assembled.

To detect the noise power we used a demodulating logarithmic amplifier (DLA) (Analog Devices - AD8310). A logarithm amplifier is a device that calculates the logarithm of an input signal. The DLA is a device applied to demodulate amplitude modulated signals, recovering the logarithm of the envelope of the input signal [107]. The DLA was combined with electronic filters and it provides information about electric power over a certain bandwidth. The response of the DLA circuit was adjusted to detect frequencies from 1 kHz to 30 kHz. The filtered frequency range is below the interferogram signal at 100 kHz, which is not affect by the measurement.

The interference signal is filtered using a band-pass filter. The signal is then fed to the DLA which converts AC signals from a large dynamic range (from µV to V) to a correspondent DC output varying from 0.5 to 1 V. The electronic schematic is shown in figure 3.23, together with the optical set-up to characterize noise. A piezoelectric element is located in the delay line to allow the temporal overlap to be controlled by a voltage source.

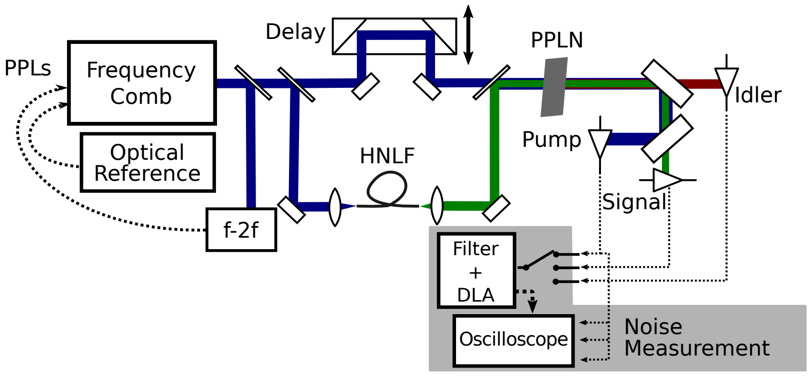

Figure 3.23: Experimental setup for intensity noise measurements. DLA: demodulating logarithm amplifier. PPL: phase-locked loop. f-2f: self-referencing. HNLF: highly-nonlinear fiber. PPLN: periodically poled lithium niobate.

A linear slope is applied to the piezoelectric and the signals from the DLA are referenced to it. The output from the DLA provides information about the noise from the three beams against the changes in pump/signal delay. The slope applied to the piezoelectric stage is 100 V, which corresponds to 172 µm delay change or approx. 570 fs which is enough to delay the pulses for more than the 130 fs FWHM pulse duration. The DLA and the control of the temporal delay allows quickly acquisition of data at small piezo displacements. Figure 3.24 shows the voltage output of the DLA, which is proportional to the integrated power of the frequency components over the bandwidth of the filter.

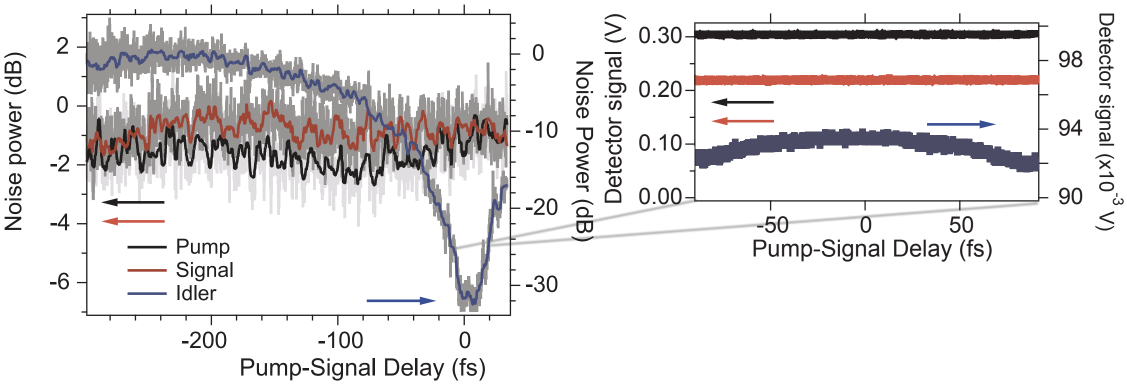

Figure 3.24: Integrated noise power of pump, signal, and idler in relation to the temporal overlap between pump and signal. The power of the three beam is also shown on the right pannel.

It is possible to observe a particular pump/signal delay when the MIR noise is minimum. Such behavior is not observed for pump or signal. Changes of the pump and signal noise are not substantial and but a tendency of signal noise to follow pump noise is observed. It is expected that the noise between idler and signal to be correlated [108] as the parametric process generates a pair of idler and signal photons. The most prominent noise source in parametric processes is superfluorescence, which is not observed in this system [108]. The minimum noise is observed at temporal delays under a few femtoseconds, which is much shorter than the 130 fs pulse duration. This behavior has a direct impact on the quality of the spectrum. The maximum output power DFG is slightly shifted from the minimum noise, and hence from the best SNR in the interferogram. The minimum noise region is observed at multiple wavelengths (not shown) throughout the tuning range. Due to the fact that this minimum is found within a narrow delay range of less than a few fs, it was not possible to determine the absolute value for this delay range.

As the operation at the minimum noise region is important, stabilization of the delay was implemented with a dither lock. Figure 3.25 illustrates the setup of the delay stabilization. A sinusoidal modulation is applied in the pump/signal temporal delay via the piezo to generate small noise modulations in the MIR. The modulation is small and no power modulation can be observed in the MIR or in the interferograms. The noise signal from the DLA is detected with a lock-in amplifier. The phase of the delay modulation in respect to the driving modulation generates an error signal. The delay is kept in the minimum noise position by adding a DC offset to the sinusoidal modulation, which centers the temporal delay in the minimum noise position. Details related to the balanced detection and the signal filtering are presented in section 4.4 The delay changes by only 80 nm, which corresponds to 57 as of temporal modulation. Due to the accentuated slope of the noise minimum, the delay modulation is small and no change in output power is detected.

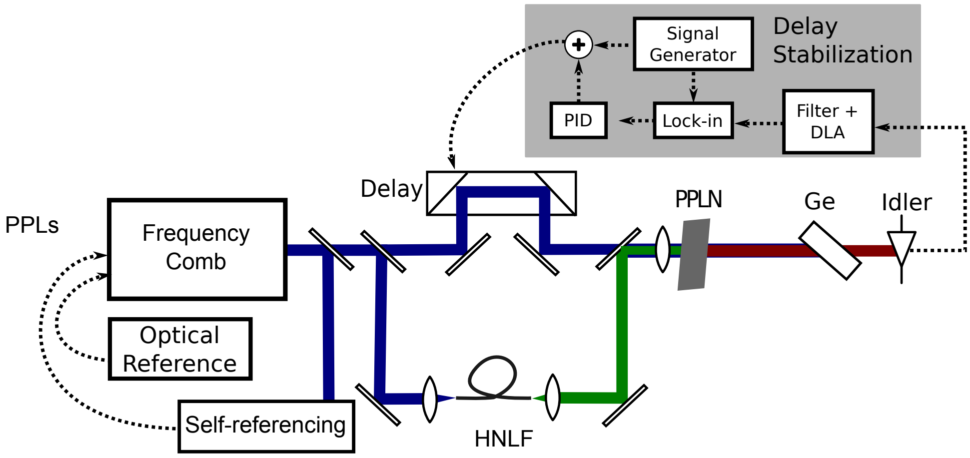

Figure 3.25: Temporal overlap stabilization setup. The MIR noise is measured and the system is keeps the delay at the minimum noise position.

After implementing the delay stabilization, it was possible to achieve stable operation for several hours at a fixed temporal overlap. The system performance is demonstrated in the context of spectroscopy results and it is presented in section 4.10.5.

4 Fourier transform spectrometer

4.1 Introduction

The mid-infrared frequency comb described in chapter 3 acts as broadband light source for absorption spectroscopy experiments. Several parameters of the MIR source were explored (beam diameter, output power, collimation), requiring modifications on the spectrometer, which occurred in parallel with the spectrometer design. The spectroscopy experiment is composed by different components as illustrated in figure 4.1.

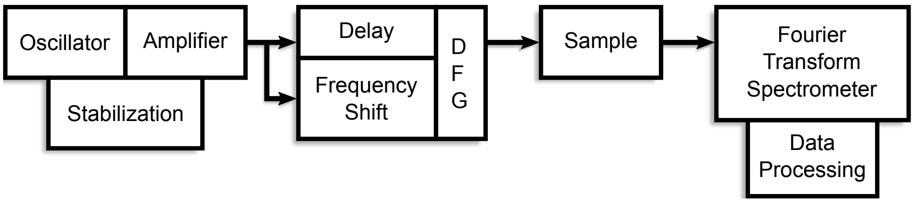

Figure 4.1: Block diagram of the parts forming the Fourier transform spectrometer, from the light source to the data processing.

It is important to have the spectrometer resolution at least two times higher than the frequency comb mode spacing, $f_{\mathrm{fts}} > (2 \times f_{\mathrm{rep}}) = 75$ MHz. In this condition it is possible to observe more than one interference fringe. The comb structure can be observed an it is possible to estimate the alignment of the MIR beam over the complete OPD range. The comparison between the amplitude of the central fringe at zero OPD can be compared to a second fringe at OPD $\pm 2c/f_{\mathrm{rep}}$.

Modifications in output power, central wavelength, and beam parameters required several optimizations from the spectrometer. Different detectors were tested, electronic amplifiers and filtering circuits are all specifically designed to achieve high SNR acquisition. This chapter describes the design of the custom Fourier transform spectrometer and provide details

4.2 Custom Michelson interferometer

The interferometer is designed to operate with the central fringe in the center of the available OPD to allow the double-sided interferogram to be recorded. A double-sided interferogram simplifies the post-processing as taking the magnitude spectrum after FT generates a spectrum with zero-phase [28].

In total, three fringes can be detected, one at the center and two at the edges of the translational stage. The comb repetition rate is 150 MHz, which requires the OPD to be $c/f_{\text{rep}} = 2$ m for a two sided interferogram and $c/f_{\text{rep}} = 4$ m to observe the central fringe plus two fringes. In order to achieve four meters of OPD on a small footprint, both arms of the interferometer are movable with the help of a translational stage. Two hollow retroreflectors are implemented facing opposite directions in respect to the translational stage movement. The double-pass configuration and two movable arms provide the required four meter OPD using a translational stage with one meter length. The schematic drawing of the spectrometer is presented in figure 4.2.

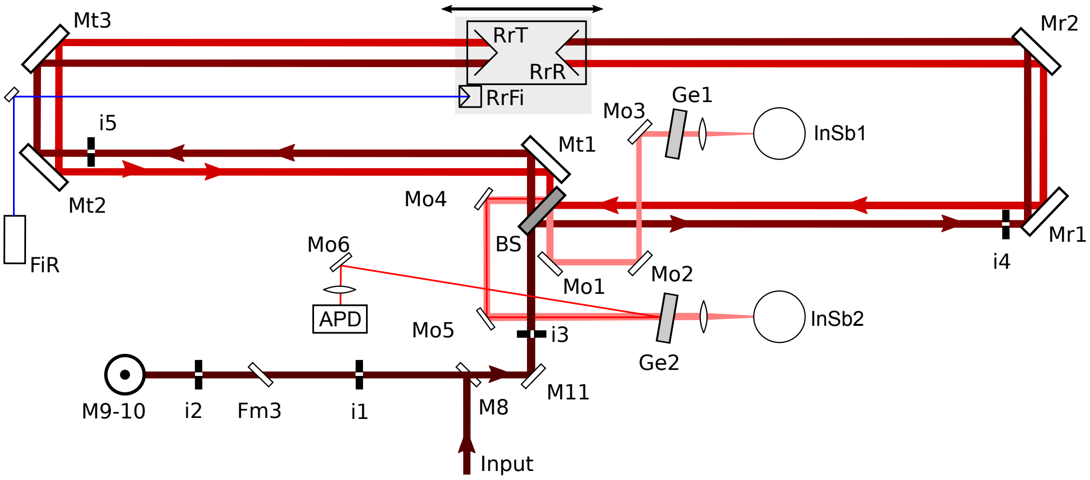

Figure 4.2: Optical setup of the Fourier transform spectrometer. Before the interferometer: M8 to M11 are mirrors and M9-10 is a periscope. Alignment irises: i1 to i5. Transmitted and reflected arms use, respectively: Mt1 to Mt3 and Mr1 to Mr2. Output steering mirrors after the beam splitter (BS): Mo1 to Mo6. RrT and RrR are the 2¨ retroreflectors for the Michelson interferometer. RrFi is the 1¨ retroreflector and FiR the fiber collimator for the reference arm of the fiber interferometer. Ge1 and Ge2 are coated germanium windows. InSb1 and InSb2 are the MIR detectors.

The correct calculation of the frequency components requires the interferogram to be sampled at equidistant steps. The calibration of the OPD is performed by using a frequency stabilized helium-neon laser (HeNe) laser. This monochromatic source generates a sinusoidal interferogram that acts as an equidistant grid for sampling the MIR at equal ODP steps. The frequency stability of the laser is 2 MHz over 24 hours, which corresponds to a relative accuracy of 10^{-9}. The absolute frequency calibration is performed via heterodyne optical beat with the frequency comb (details in appendix B on 119).

The interferogram amplitude is high at the central fringe and rapidly decays with increasing OPD. For this reason it is not possible to increase the signal, due to saturation of the detection, and it is important to design the data acquisition to minimize noise sources. Large part of the efforts during the work described in this thesis was to reduce and eliminate noise in order to increase SNR. The next sections describe the design of the interferometer and the steps taken in the direction of recording high quality spectroscopy data.

Mirror M8 steers the beam to periscope M9-10, which increases the beam height and directs it to the input mirror M11. Irises i1 to i3 are used for alignment of the input beams. The flip mirror Fm3 serves as a second input when it is necessary to bypass the gas cell. The Michelson interferometer starts at the beam splitter BS. The transmitted arm passes through 3 mirrors (Mt1 to Mt3) and the reflected through 2 mirrors (Mr1 and Mr2). Retroreflectors are mounted on a translational stage which generates the OPD for the transmitted (RrT) and reflected (RrR) beams. The RrFi retroreflector is used for the reference arm of the fiber interferometer (described in section 4.10). Irises i4 and i5 are used to align the beams trough the interferometer.

At the output, the reflected beams go through mirrors Mo1 to Mo3, and the transmitted beams go though Mo4 and Mo5. The germanium windows Ge1 and Ge2 act as filter, transmitting the MIR beam which is focused on the detectors InSb1 and InSb2. The reference laser is reflected by Ge2 window and is guided with Mo6 to be focused on the avalanche photodiode (APD).

The mirrors before the interferometer (M8-M11) and after (Mo1-6) are standard gold coated 1 inch mirrors, high-reflective from 600 nm to 5 μm. The optics inside the interferometer (BS, Mt1-3, Mr1-2, RrT, RrR) are two inches in diameter and the mirrors gold coated. Two inches optics are necessary to avoid overlap between the inward and outward optical paths. They provide a common reflective surface, stability, and damping of acoustic noise sources.

The two interferometer arms are steered to retroreflectors RrT and RrR after the beam splitter. The retroreflectors are mounted on a 1 m long translational stage, and face opposite directions allowing simultaneous OPD change in both interferometer arms. The double retroreflector configuration changes the OPD of both arms in opposite ways, which corresponds to a total OPD change of four times the physical displacement of the retroreflectors. Using the 1 m long stage it is possible to generate about 4 m of OPD, which is 75 MHz nominal resolution. In a typical measurement, the retroreflectors are moved at 125 mm/s speed, or 500 mm/s OPD change.

The interferometer is assembled on a 1500 x 600 x 60 mm optical breadboard. The setup is enclosed by 3 mm thick PMMA sheets which isolate the interior from laboratory air. Acoustic isolation is performed using 3 mm thick PVC sheets attached to the PPMA walls. The transmittance spectrum was simulated to estimate the effect of the four meter optical in the baseline absorption. Figure 4.3 shows the transmittance spectrum from lab air, with the line strengths taken from HITRAN [5]. The gas mixture and the respective concentrations by number of molecules in $\%$ (taken from [109]) are: H_2O:0.141, CO_2: 0.033 ,O_3: 0.000002, N_2O: 0.000032, CO: 0.000015, CH_4: 0.00017, O_2: 20.900001, N_2: 78.92578. The top graph shows the total air transmittance and the bottom graph shows the main contributors, namely, water vapor, carbon monoxide and carbon dioxide.

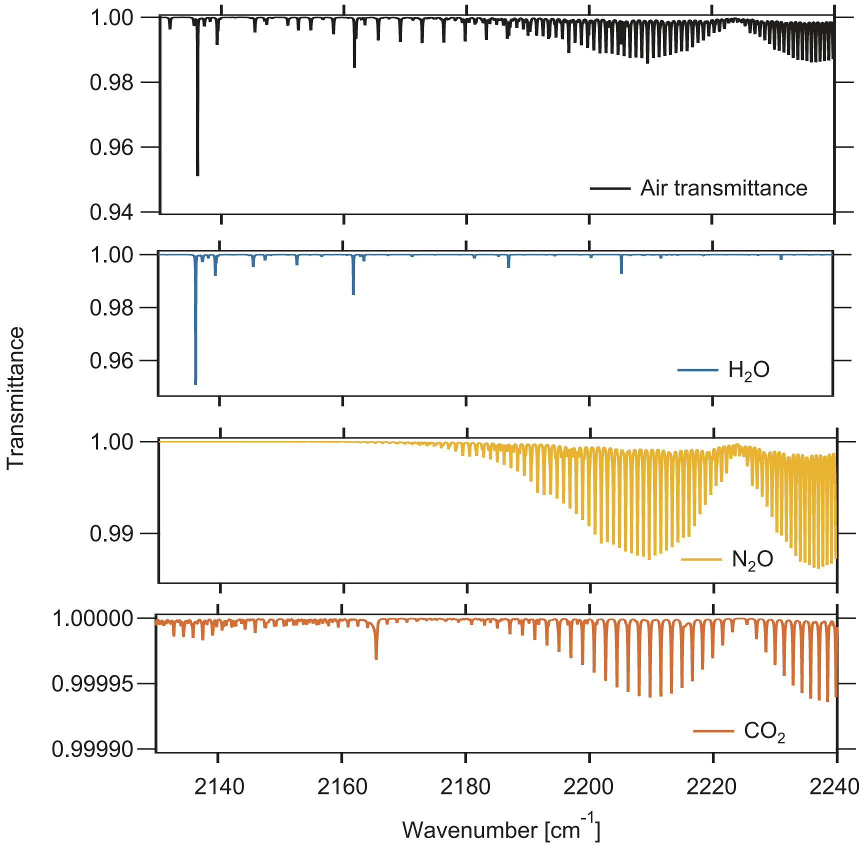

Figure 4.3: Calculated transmittance spectrum of air for an optical path of four meters, pressure 1 *atm, temperature* 296 *K. Calculated from the HITRAN database [5]*

4.3 Interferometer input

The MIR laser is not the only laser taking part into the experiment. The reference laser (HeNe) is responsible to measure the OPD and provides an equidistant grid to sample the MIR. A third laser is employed to measure the length of the gas cell, which is required in the calculation of the line intensity (discussed in section 2.2). The measurement of the length of the gas cell is crucial to determine the path length through the sample (which will be discussed in detail in section 4.10). The arrangement of the input beams before being directed to the spectrometer is shown in figure 4.4.

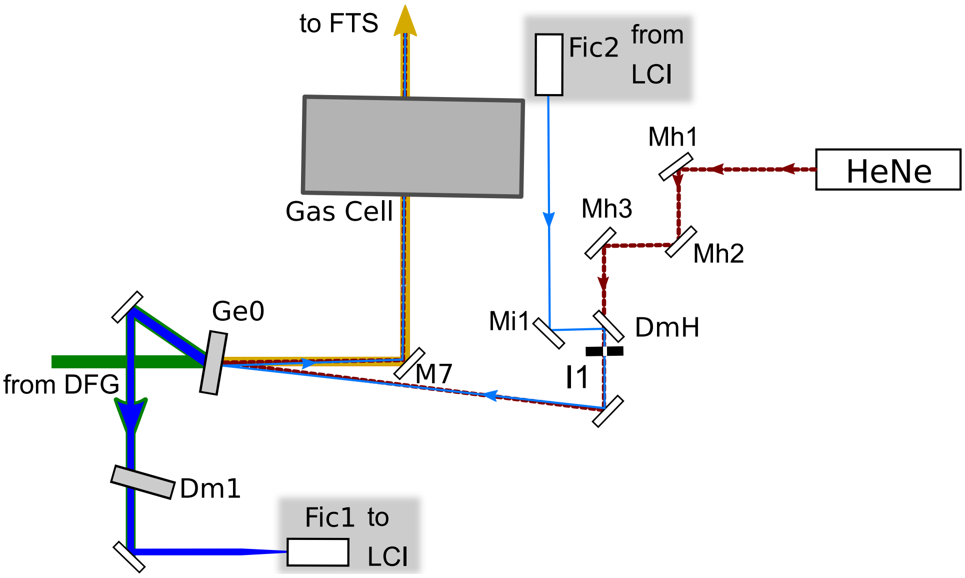

Figure 4.4: Arrangement of the input beams before being directed to the spectrometer in a collinear geometry. Ge0: MIR coated germanium window. Dm1: long-pass filter for 1 µm*. DmH: dichroic mirror, HT to* 633 *nm and HR to* 1µm*. i1: iris. Mh1-3: alignment mirrors for the reference laser. Fic2: fiber collimator of the measurement arm of the fiber interferometer.*

The Ge0 window filter residual components after the DFG stage. It transmits the MIR and reflects pump, signal, and other non-phase matched components such as the respective second harmonics, and sum frequency generation. The reflected light on Ge0 is guided to Fic1, which is a fiber collimator. The residual pump at 1µ m is filtered with the Dm1 long-pass (Thorlabs DMLP1000) and will be the laser source for the measurement of the cell length. It goes through a low-coherence interferometry (LCI) setup (which is discussed in section 4.10) and exits close to the gas cell on the Fic2 collimator. The DmH dichroic mirror combines in a collinear geometry the 1 µm from the LCI, and the HeNe. The combined beams (1 µm and HeNe) are steered to the Ge0 window and are reflected. Together with the transmitted MIR, they are guided by the M7 mirror towards the interferometer.

As discussed in section 2.5.1, the angle between the MIR and reference laser is a source of frequency error in the FTS. This angle is kept to a minimum because of the collinear arrangement. In combination with the long OPD ($>$ 4 m) and alignment irises, the effect of the angle between reference and MIR cannot be observed in the FTS results.

4.4 Photodetectors

Photodetectors can be found in a variety of configurations and it is helpful to have a parameter to compare performance among different detectors. Noise-equivalent-power (NEP) is a specification commonly found in photodetectors reports and it is measured in [W/$\sqrt{\text{Hz}}$]. It is defined as the signal power that gives a SNR of 1 over one Hz output bandwidth. Because NEP does not include the photodetector area, it cannot be directly used to compare photodetectors performance. Instead, the specific detectivity, D^*, is derived from the NEP and uses area (A) and bandwidth (f) as a normalization factor. Specific detectivity is measured in Jones [cm $\cdot$ $\sqrt{\text{Hz}}$/W] and usually defined by:

$$D^* = \frac{\sqrt{Af}}{NEP}. \tag{4.1}$$

It is also possible to show that the detectivity is connected to intrinsic properties of the semiconductor material. A theoretical model was proposed by [110] to calculate the limits in detectivity for infrared photodiodes in the range of 2 to 20µm. It is shown that the detectivity of a photodiode can be expressed as:

$$D^* = 0.31\,\frac{\lambda}{hc}\left(\frac{\alpha}{G}\right)^2, \tag{4.2}$$

where λ is the wavelength, h Planck's constant, c the speed of light, α the absorption coefficient and G the thermal generation rate. The ratio α/G is the figure of merit to compare detectors performance. The absorption coefficient decreases for semiconductors in the MIR [111, 112] . Moreover, the generation rate increases with temperature and the figure of merit decreases. This relation shows that detecting light at long wavelengths has two main disadvantages. Photodetectors in the MIR usually require cooling during operation to decrease the thermal generation rate G. Combined with the low absorption coefficient, photodetectors in the MIR present typical D^* values that are two orders of magnitude smaller than Silicon (Si) or Indium gallium arsenide (InGaAs) technology. Typical $D*$ values for Silicon and Gallium-arsenide are in the range of $D^* = 10^{13}$, whereas for indium antimonide (InSb) and mercury cadmium telluride (MCT) at liquid nitrogen temperatures, it is on the order of $D^* = 10^{11}$ [113].

In order to characterize the detectors performance in yielding high-SNR spectra, different detectors were tested to acquire interferograms. The results were compared by observing their performance at the frequency domain. Three detectors were tested, two liquid nitrogen cooled (LN) and one cooled by a three stage thermo-electric element (TE).

The TE-MCT has the advantage of being small and easily handled, because it is not cooled by liquid nitrogen. However, the operation temperature is 210 K and the detectivity $D^* > 2 \cdot 10^{10}$ at 6 µm which is one order of magnitude lower than the two LN cooled detectors. The liquid nitrogen cooled MCT (LN-MCT), and the liquid nitrogen cooled InSb (LN-InSb). The LN-MCT specifications were unknown and had to be tested via the measurements. The LN-InSb has an area of 0.5×0.5 mm and $D^* = 1 \cdot 10^{11}$ at 6 µm. The peak sensitivity of the InSb is at 5 µm, where the experiments were designed to be performed (CO absorption band centered at 4.6 µu). Figure 4.5 shows a comparison between the LN-InSb and the LN-MCT response.

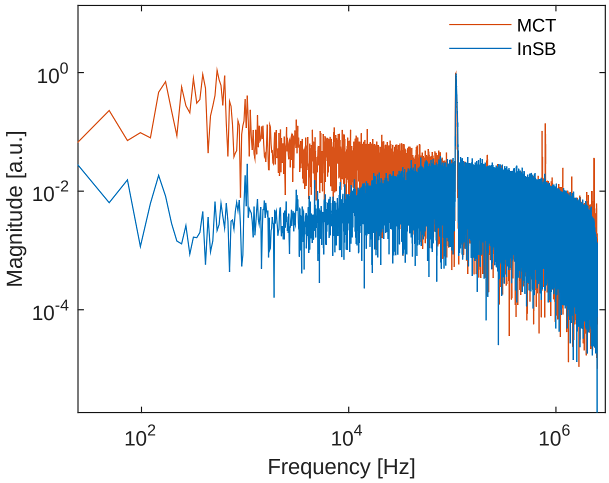

Figure 4.5: Frequency spectrum of the LN-InSb and LN-MCT detectors during a measurement. Two traces acquired at equal MIR average power normalized to the peak at 100 *KHz, which is the signal from the interferogram. The interferogram peak-to-peak signal was* 1.4 *V for the LN-MCT and* 6.8 *V for the LN-InSb.*

The LN-InSb has a few advantages for having a higher sensitivity and for being photovoltaic. To decrease shot-noise, the gain of the LN-InSb was reduced and the power of the MIR increased. In addition, photovoltaic detectors generate current in response to optical power which facilitates the arrangement of the balanced detection.

4.5 Balanced detection

Narrow features in the spectrum are located in the interferogram wings, at long OPD values where the signal amplitude is low. An extensive portion of the noise is caused by amplitude fluctuations of the light source (described in section 3.2). Amplitude fluctuations arise also from vibrations in optical components, and pointing due to the long optical path from the amplifier output to the FTS detectors. Air turbulence caused by temperature gradients over the optical path can contribute to the overall noise. One possible solution is to increase the amplitude of the signal in order to exceed the noise floor. In FTS, however, the dynamic range of the detector is the limiting factor and it is not possible to increase the optical power. The means to increase the quality of the signal needs to be via decreasing the noise.

Balanced detection is an established technique employed in detection systems that can efficiently suppress common-mode noise [114, 115]. It is performed by using two detectors and subtracting their currents before amplification. The subtraction suppresses in-phase components of the signal, whereas out-of-phase components are combined increasing the electric signal. This is of particular relevance in optical systems when the detection involves a beam splitter, which is the case of the FTS [116]. At the output of the interferometer, the two arms of the interferometer are separated in transmission and reflection and are out of phase. In addition to canceling common mode noise, the detection is more efficient because the two outputs of the beam splitter contribute to the signal.

Balanced detection was performed by using two InSb detectors. The polarity inversion has to be performed as close as possible to the photodiode to avoid electrical and electromagnetic interference in the signal. As the temperature isolation prevents direct access to the photodiode electronic contacts, the closest point is the SMA connector at the detector housing. The polarity of detector InSb1 signal was reversed after this connection as illustrated in figure 4.6.

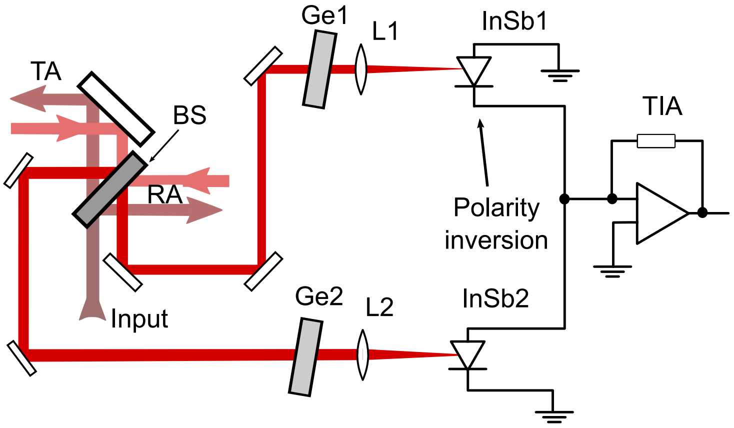

Figure 4.6: Optical and electronic at the output of the spectrometer. The light colored beams shows the input, the beam splitter (BS), the transmitted arm (TA), and the reflected arm (RA). L1 and L2 are the focusing lenses with $f1 = f2 = 65mm$*. At the output connector of the detector InSb1, the polarity is inverted. TIA: transimpedance amplifier. Ge: germanium filter.*

Figure 4.7 shows the interferograms and spectrum acquired at equal conditions, except for the balanced detection. It is possible to see a noise reduction and features that were below noise floor can be easily seen in the interferogram. The frequency domain shows a clear noise floor reduction and an overall increase in performance.

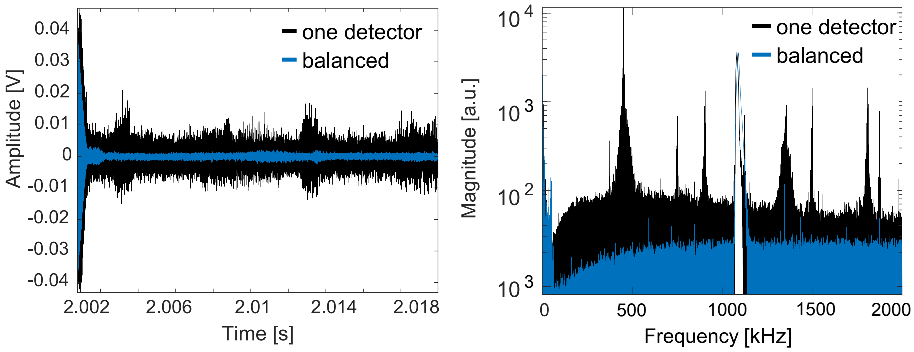

Figure 4.7: Interferograms and spectra showing the improvement of using the balanced detection. Top: interferogram acquired without (black) and with (blue) balanced detection. The traces were normalized to 1 on the central fringe for comparison. Bottom: the Fourier transformation of the interferograms on the top graph in logarithmic scale.

4.6 Signal digitization

The interference signals (from the MIR and HeNe) are simultaneously digitized by a National Instruments PCI-5922 data acquisition board controlled with a computer. This board offers flexible values for digitizer resolution and sampling rate. At low sampling rate, 500 kSa/s, the resolution is 24 bits, and at the higher end at 15 MSa/s, the digitizer resolution is 16 bit. The RMS noise at 5 MSa/s is around 30 μV which corresponds to more than 100 dB dynamic range. The flexibility allowed tests to be performed until a compromise was achieved between acquisition speed, dynamic range and number of sampling points. High-dynamic range is necessary because of the ratio between the signal amplitude on the central fringe at zero OPD and the interferogram edges. Typical interferograms are presented in figure 4.8.

The central fringe signal has contribution from all spectral components as they interfere constructively. This signal is typically in the volt range and can reach 10 V for this spectrometer. To illustrate the situation, interferograms with SNR (ratio between central fringe maximum and noise floor standard deviation at the interferogram wings) less than 50 and above 1000 are presented in figure 4.8. The traces are normalized to one on the central fringe intensity to facilitate the comparison.

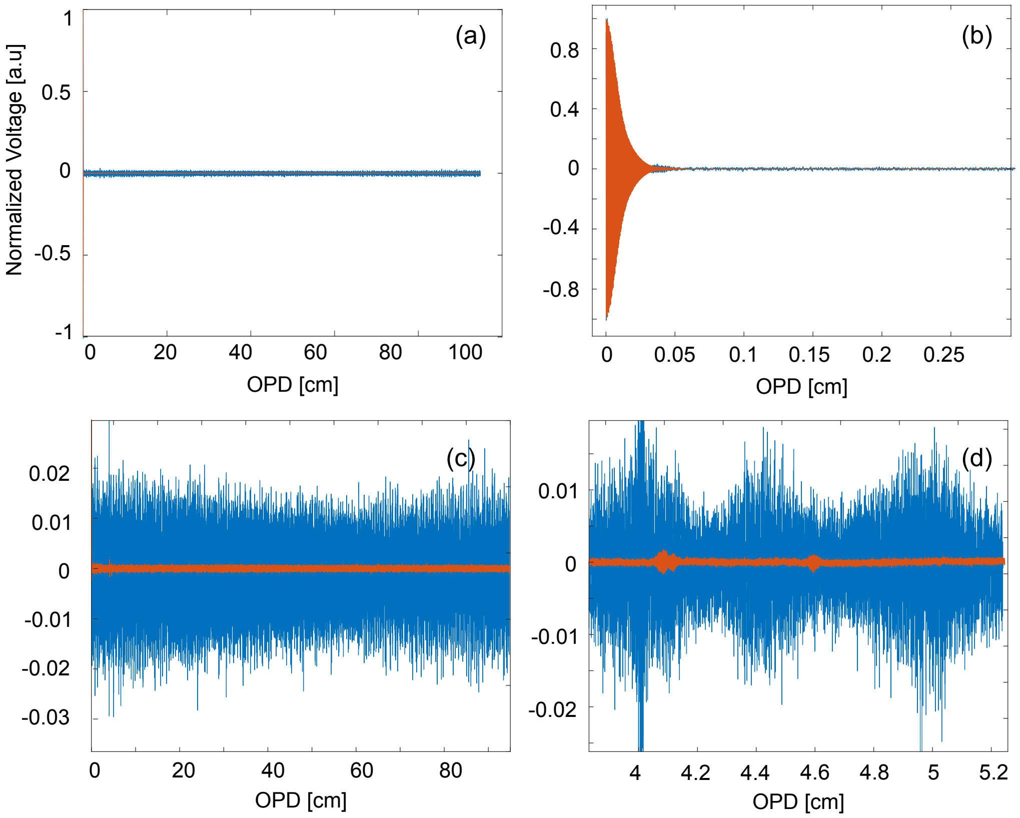

Figure 4.8: Comparison between signal-to-noise of two interferograms. The blue curve is an interferogram with lower SNR than the orange. This measurement was performed at the beginning of the development when such an interferogram was the highest achievable SNR. The orange curve is one of the latest measurements. (a) Single sided interferogram. (b) Zoom at the abscissa from 0 *to* 0.25 *cm OPD to show the central fringe. (c) Zoom on the ordinate for a clear comparison in noise reduction. (d) Zoom on both axis to show features covered by noise.*

4.7 Electrical signal filtering

The InSb detector and the amplifier are separated components connected via a coaxial cable. The electronic circuits could be accessed and modified. The transimpedance amplifier gain was reduced because the intense central fringe was saturating the detection system. The ADC was being saturated by the peak-to-peak amplitude of the interferogram (> 10 V) and prevented the full power of the MIR to be used. The transimpedance amplifier gain is adjustable and was measured to be approximately 70 dB to 100 dB, which was decreased by a factor of 5. Decreasing the amplifier gain allowed the average power of the MIR beam to increased, which decreased shot-noise.

Bandpass filters were designed to separate the interferogram in three frequency ranges. At the lower end (DC to 10 Hz), the signal is used to measure the MIR average power and is convenient to perform alignments, measure RIN, and optimize the balanced detection (described in the next section). Intermediate frequencies (1 kHz to 30 kHz) are used to measure intensity noise and generate the error signal for delay control in the DFG stage (discussed in section 3.2.5). The higher frequency range (100 kHz to 300 kHz) is used for the interferogram acquisition. Figure 4.9 illustrates the separation of these frequencies.

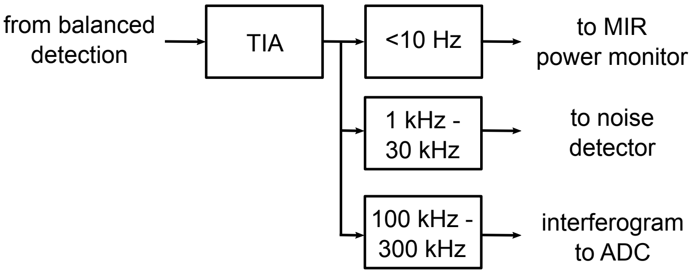

Figure 4.9: Electronic filtering of the interferogram signal in three frequency regions. InSb: mid-infrared detector. TIA: transimpedance amplifier.

4.8 Reference laser

The reference laser is helium-neon (HeNe, SIOS SL4) laser with wavelength $\lambda_{\mathrm{ref}} = 632.9909178$ nm, corresponding to a frequency $\nu_{\mathrm{ref}} = 473612436.6$ MHz $(+0.508; -0.428)$. The frequency is stabilized to 10^{-9} corresponding to 1 MHz over one hour.

The reference laser wavelength is shorter than the MIR and it generates the highest interference frequency. For 500 mm/s OPD change, the interference frequency of the reference laser is 1.6 MHz. In combination with the sampling rate of the analog-to-digital converter and the number of samples per half fringe, the reference laser sets the limit for the scanning speed. Figure 4.10 shows a typical measurement of the HeNe interference measure at 600 mm/s OPD change.

The interferogram frequency was chosen to be the highest possible, to allow the fastest acquisition times without adding noise. Another advantage to have the highest frequency is to avoid flicker noise with $1/f$ power spectral density. At high speeds, the translational stage movement generates air turbulence from the rapid movement of 2 inch optics, mechanical vibrations and acoustic noise.

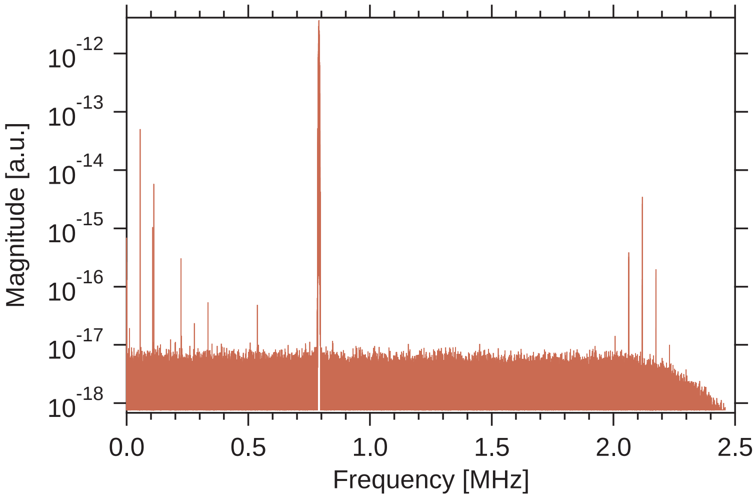

Figure 4.10: Typical measurement of the reference laser interferogram. The frequency axis shows from 0 *to Nyquist which is half of the sampling rate* $F_s/2$*.*

The acquisition is performed at 5 MSa/s sampling rate with 20 bit resolution. This value was chosen to combine a fast acquisition time and at least four data points per half-fringe of the reference laser to achieve a good retrieval of the zero crossings. Figure 4.11 shows on top the MIR interferogram close to the central fringe and on the bottom the HeNe interferogram for comparison.

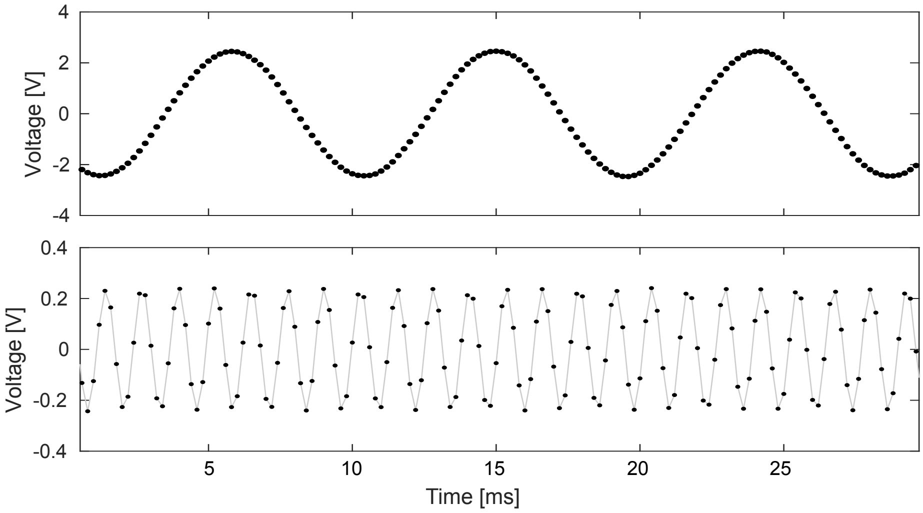

Figure 4.11: Interferogram data points before resampling. MIR (top) and HeNe (bottom) interferograms before resampling. The x axis is the time after the start of acquisition.

In order to test the scanning speed influence on the spectrum SNR, interferograms were recorded at different scanning speeds. The relation between noise power, N, and measurement time, t is: $N = \mathrm{NEP}/t^{1/2}$ [28]. In principle, shorter measurement times contribute to increasing the SNR until $1/f$ starts to dominate. Table 4.1 shows the SNR$_{std}$

of the spectrum in relation to different scanning speeds in the initial phase of construction. Despite the initial low values of SNR, the trend holds for the higher SNR achieved at the final stages of construction. Scanning at speeds lower than 500 mm/s decreases the SNR and increases the measurement time considerably.

*Table 4.1: Interferogram signal-to-noise ratio for different rates of OPD change. As increasing the speed does not affect the SNR_{std}, the OPD change speed was set to*500 *mm/s. This is a good compromise between acquisition time, SNR_{std} and the ADC dynamic range at* 20*bits.*

OPD change (mm/s)	SNR_{std} (std)	Sampling rate (MSa/s)	Dynamic Range (bits)
2000	46(5)	15	16
1500	45(11)	15	16
500	50(4)	5	20

4.9 Data management and processing

The grid spacing in the spectrum is inversely proportional to the number of points in the interferogram. It is possible to record the interferogram longer than required and choose the spectral point spacing post-acquisition, decreasing the number of points in the interferogram before performing the FT. The maximum OPD change in this spectrometer is 4 m, which corresponds to grid spacing of 75 MHz, two times higher than the repetition rate. Recording data at this OPD would generate unnecessary amounts of data. As discussed in section 2.5, recording an interferogram longer than the comb spacing is not necessary. For an optimized acquisition, the grid spacing should be equal to the repetition rate, which is roughly 150 MHz. The data is recorded at 145 MHz to provide a secure margin for the data processing, which corresponds to 20.5 million raw data points and 6.5 million data points after resampling at the HeNe zero-crossings. Including the HeNe interferogram, the file size of such an acquisition is 380 Mb.

The interferogram of the reference laser is used to resample the MIR interferogram at equidistant steps of optical path difference, corresponding to half of the reference laser wavelength. After resampling, the MIR interferogram size is reduced by a factor of 5, which represents an average value of data points per interference fringes of the reference laser. Each scan is saved in a binary file containing the raw MIR and HeNe interferograms. The first step is to resample the MIR data using the zero crossings of the HeNe. The resampling procedure is illustrated in the figure 4.12, which is a simplified illustration of figure 4.11. Due to the discrete sampling, the points are scattered around zero volt, either at positive or negative values. The vector h represents the HeNe interferogram containing n number of points. The data point before the zero crossing is determined and stored in the vector i, so that for the mth crossing points, $h(i(m))$ is the point before and $h(i(m)+1)$ the point after the zero crossing. The ratio $r_h(m) = h(i(m))/(h(i(m)) - h(i(m)+1))$ gives the relative mismatch to zero. The MIR interferogram and h are equal in length and the resampled point $res(m)$ falls between $mir(i(m))$ and $mir(i(m)+1)$. The relation $res(m) = mir(i(m)) - r_h(m) \cdot (h(i(m) - mir(i(m)+1))$ is used to calculate the interpolated points, at fixed OPD spacing corresponding to half the HeNe wavelength.

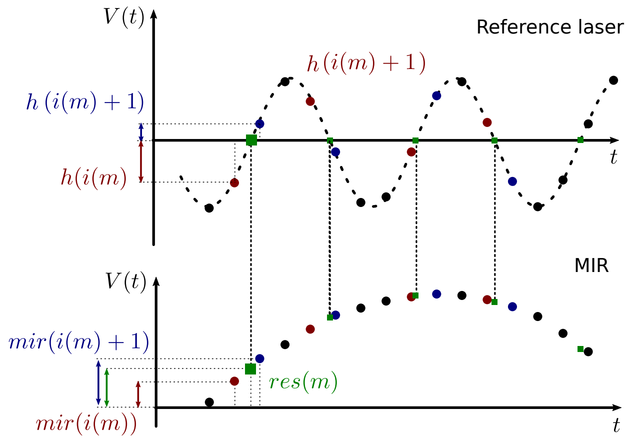

Figure 4.12: Graphical explanation of the MIR interferogram resampling on the zero crossings from the HeNe interferogram.

The number of points N_0 necessary to achieve a resolution f_{res} is given in equation 2.39. The resampling is performed individually for each MIR interferogram at equal number of points. For the 150 MHz measurements, the amount of points is reduced from 41 million to 6.5 million and the file size to 45 Mb. The resampled MIR interferogram is stored for further processing.

The data analysis procedure depends on the type of spectrum. There is a distinction between spectral features fully resolved by the FTS nominal resolution (standard method), and spectral features that are narrower than the FTS nominal resolution (sub-nominal method). When narrow absorption features are present in the spectrum, multiple acquisitions are performed with the frequency comb spacing at slightly different values, as discussed in section 2.5.2.

At nominal resolution higher than the comb spacing, interferograms are processed individually. A certain number of spectra is averaged to produce one averaged background spectrum and one averaged sample spectrum. The natural logarithm of the transmittance, divided by the interaction length produces the absorbance spectrum (from equation 2.17).

Processing of the interferograms with the sub-nominal method has extra steps. The final spectrum is composed by interleaving the spectra which were acquired at different repetition rates of the frequency comb. For each spectrum, the interferogram needs to be have the exact length which corresponds after FT to data points spaced by the repetition rate of the laser. At a resolution $f_{\text{res}} = 150$ MHz, the required number of points on each side of the central fringe is:

$$N_0 = \frac{c}{\lambda_{\text{ref}} f_{\text{rep}}} = \frac{299792458[\text{m/s}]}{632.998 \times 10^{-9}[\text{m}] \times 150 \times 10^{6}[\text{Hz}]} = 3157381.83 \tag{4.3}$$

This calculation is an approximation because λ_{ref} needs to be corrected (see section 2.5) and because f_{res} needs to be matched to the repetition rate, which depends on the measurement (a practical example is give in section 5.4.1). Due to the discrete sampling of the interferogram, it is necessary to round N_0 to closest integer. The total number of points is on the order of 6×10^6. As described in section 2.5, two approaches can solve the mismatch: zero-padding the interferogram, and adding a frequency shift on the FTS grid. In any of the scenarios, it is necessary to have multiple Fourier transformations to generate one interleaved spectrum, and observe the effects of the ILS. Using zero-padding, the change is performed in the interferogram length by changing the amount of points on the interferogram one point at a time. Using the frequency shift, a multiplication (described in equation 2.42) is performed on the interferogram of fixed length N_0 calculated via equation 4.3. Therefore, the required time to generate one interleaved spectrum is in the order of tens of seconds.

In principle, for an offset free frequency comb (as in the case of a DFG comb), only zero-padding is required to achieve a proper match between the comb grid and the FTS grid. For the interferograms at 150 MHz, a large amount of GPU memory is required to process the the interferograms after padding. This limitation was overcome using a computer cluster and it was possible to test the zero padding up to a factor of eight. The high end CPUs (32 x E5-2698 v3 @ 2.30GHz) and GPUs (Tesla K40m, 12 GB, 1.43 Tflops with double precision), low-latency network, and large RAM memory were explored. Using the cluster, it was possible to perform FT padding the interferogram to a factor of eight. The required time for processing one interferogram with padding is in the order of 2 s.

4.10 Experimental structure

Spectroscopy experiments are performed to retrieve accurate values of absorption line parameters. It is necessary to precisely know the temperature, pressure, and the optical path traveled by the MIR through the sample.

Temperature and pressure were recorded with commercial devices, while the optical path was measured in a custom experiment, which is described separately in the next section. Temperature measurements are performed by a class A thermistor calibrated by the standard probe (Fluke 5641) and Ohmmeter (Keithly $8\ 1/2$ digits). The standard probe has a metallic enclosure and it is 114 mm long, which prevents its directly use in the gas cell. The class A thermistor is calibrated against the reference thermistor and can be placed directly at the gas cell, with the thermal contact guaranteed. The pressure measurement is performed by three pressure gauges covering different pressure ranges: from 0.1 to 1000 mbar (Pfeiffer CMR 361), from 10^{-4} to 1.1 mbar (Pfeiffer CMR 364), and from 10^{-4} to 10 mbar (MKS 90A11TRA).

4.10.1 Gas cell

The absorption cross-section in the MIR spectral region is orders of magnitude stronger than the cross-sections at the overtones. Due to the absorption intensity, the optical path through the sample can be short and a single pass can be sufficient to achieve $100\ \%$ absorption for pure gas samples. The gas cell consists of two view ports and a spacer flange, all standard vacuum components, as shown in figure 4.13. Wedged CaF_2 windows provide the beam path through the gas cell and allowed transmission from visible to the MIR region. Transmission over a wide wavelength range is important because it allows an equal beam path between MIR, HeNe and the $1\ \mu m$.

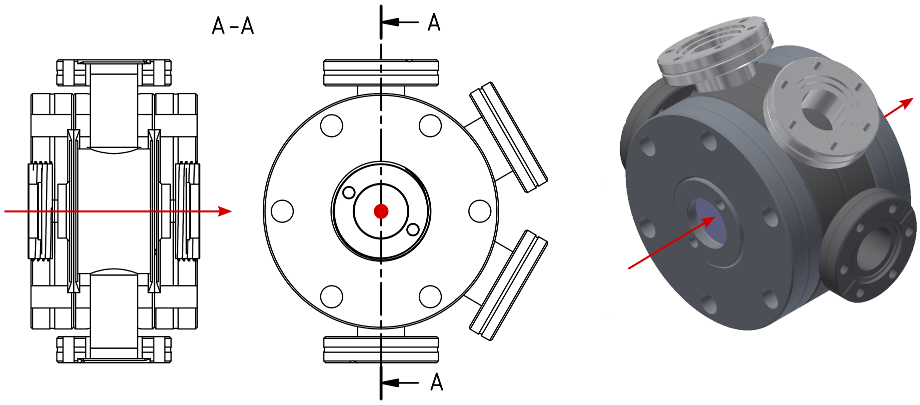

Figure 4.13: Gas cell used in the experiments. The red marks indicate the beam path.

4.10.2 Low coherence interferometry

The calculation of line strengths requires the measurement of the path length through the sample, which is the space between the two windows of the gas cell. Therefore, the accurate measurement of the beam path through the sample is crucial for obtaining accurate line strength values.

The measurement of the cell length was performed using low-coherence interferometry (LCI) with a setup based on Ref. [117]. The principle is to detect the reflected light from the gas cell windows by interfering the reflections with a reference pulse. The experimental setup is illustrated in figure 4.14.

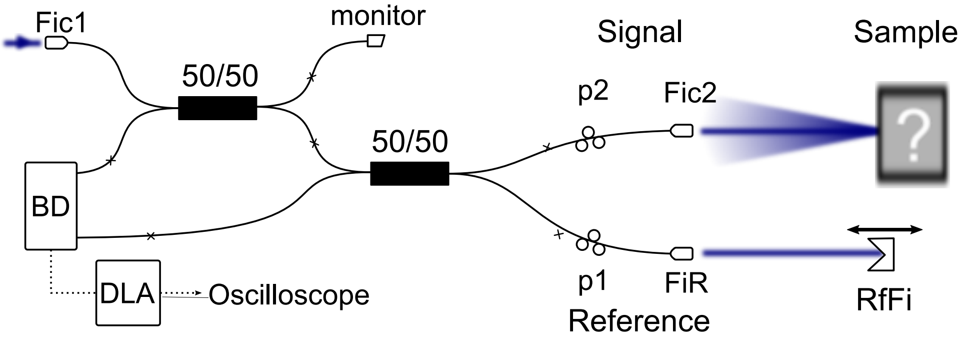

Figure 4.14: Schematic drawing of the low coherence interferometer. Fic1: fiber collimator input; p1 and p2 are polarization controllers; FiR: reference arm collimator; Fic2: signal arm collimator; BD: balanced detection; DLA: demodulating logarithmic amplifier.

It is a simple device to fabricate where the main components are two broadband fiber couplers. The input pulse is the residual 1 µm from the DFG stage (see figure 4.4) which is coupled in the fiber collimator Fic1. Two couplers with $50\ \%$ splitting ratio provide a way to use balanced detection. The interference occurs in the second coupler, analog to a Michelson's interferometer beam splitter. The reference arm of the interferometer is guided to the 1 m translational stage and is reflected by the retroreflector FfFi (shown in figure 4.2). The change in OPD is tracked by the same reference laser as the large interferometer. The fiber collimator Fic2 is the output for the signal arm, which is directed to the gas cell.

The outputs is detected with an InGaAs balanced detector (Thorlabs PDB450C). A demodulating logarithm amplifier (similar to the one employed in the detection of the MIR noise discussed in section 3.2.5) is employed to detect the signal. Figure 4.15 shows a typical result from the LCI measurement with the background removed. Four reflections are observed (indicated by the small arrows) and the large arrow indicates the path inside the gas cell. The graph on the right shows one of the peaks and a parabola fit, used to calculate the center of the interference signal.

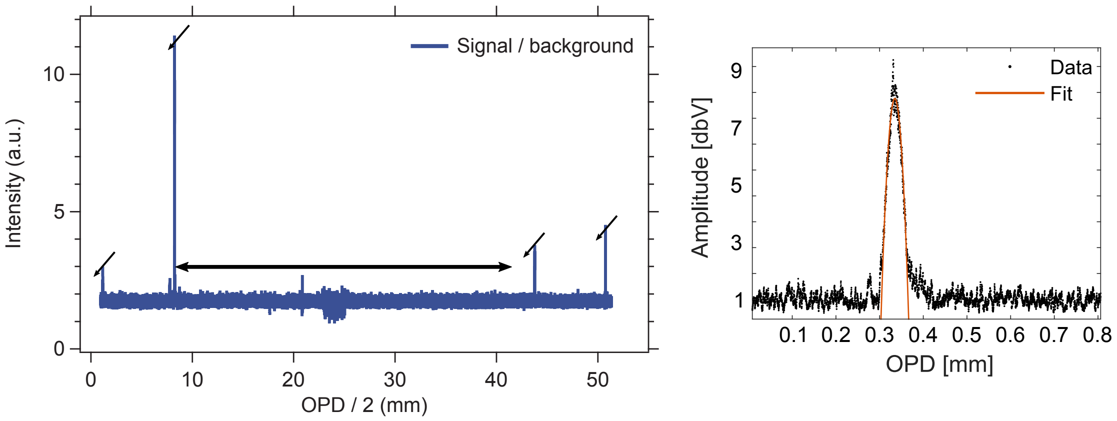

Figure 4.15: Typical results of the LCI measurements. Left: LCI measurement with background reflections removed. Four peaks corresponding to the two surfaces of each substrate can be seen. Right: example of the fitting applied in the retrieval.

Several measurements were performed to provide statistical distribution. Figure 4.16 shows the calculated values of 20 measurements performed in vacuum. The precision, calculated by the standard deviation is in the order of 1 µm. The accuracy of the measurement provided by the tracking of the reference arm, which is performed by the reference laser of the FT spectrometer.

4.10.3 Optical path length measurement

In order to evaluate the effects of increasing the pressure inside the cell, the length measurement was repeated at different pressures of nitrogen: 5, 400, 500 and 700 mbar. Twenty measurements for each pressure were performed to obtain the statistical informa-

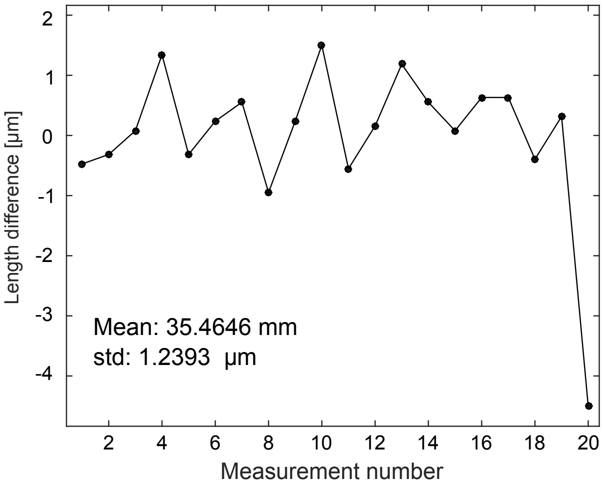

Figure 4.16: Length difference from the mean value of the cell length calculated from twenty scans. The mean value is 35.46 µm *with a standard deviation of* 1.2 µm*, which corresponds to* 16*fringes of the reference laser.*

tion about the calculation of the length. Results from this measurement are presented in table 4.2.

Table 4.2: Cell length measurement results for different pressures of nitrogen.

Pressure (mbar)	Mean length (mm)	Std (µm)
$< 4 \cdot 10^{-4}$	35.4646	1.24
5	35.4651	1.85
400	35.4699	1.27
500	35.4715	1.80
700	35.4727	1.03

The observed increase in length values are not related to an increase in separation between the cell windows but rather to the gas itself. The refractive index change due to the nitrogen concentration increase in the gas cell was calculated [118]. The relation between the measured and the calculated change is shown in figure 4.17. It is important to notice that the length difference is at the 3×10^{-4} level which is close to the statistical error.

Despite the wedged windows, the gas cell has to be operate at an angle to minimize the etalons amplitude. The weak reflection from the windows only allow measurement to be performed at small angles, which is different from the angle during the spectroscopy experiments. The cell length is mounted on a rotation stage with 5 arcmin resolution with a vernier scale. The length of the cell is measured at two angles to estimate the length at zero angle between the cell and the laser beams.

The cell was placed at an angle θ_1 which has an offset θ_0 from the true zero angle

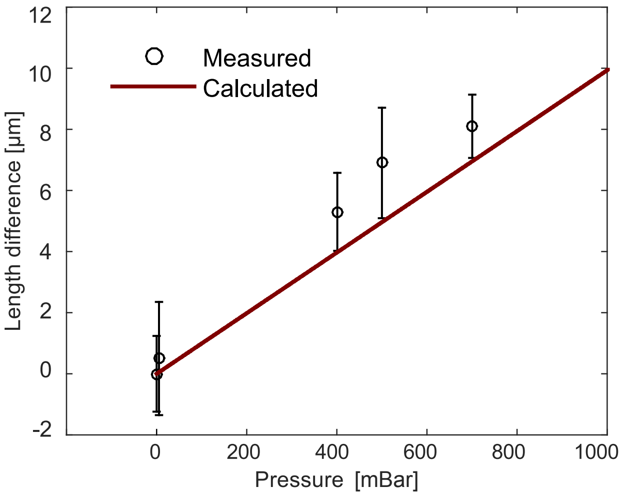

Figure 4.17: Measured path length difference Nitrogen pressure in the gas cell. The observed increase in length can be attributed to the increase of the refractive index due to the nitrogen add to the cell.

between the beam and the cell. A series of length measurements were performed to yield $L_1 = 34.8265$ mm at the angle θ_1. The cell angle was changed to angle θ_2 and the length changed to $L_2 = 34.6404$ mm. Considering a length at zero degrees L_0, the relation $L_0 = L_1 \cdot \cos(\theta_1 + \theta_0)$ and $L_0 = L_2 \cdot \cos(\theta_2 + \theta_0)$ can be used to calculate the length at zero degrees. If $L_1, \theta_1, L_2 \theta_2$ are known, it is possible to calculate the cell length at an arbitrary angle and the offset θ_0

$$\begin{aligned} L_1 \cdot \cos(\theta_1 + \theta_0) &= L_2 \cdot \cos(\theta_2 + \theta_0) \\ \frac{L_1}{\cos(\theta_2 + \theta_0)} &= \frac{L_2}{\cos(\theta_1 + \theta_0)}. \end{aligned} \tag{4.4}$$

Using the trigonometric identity

$$\cos(\theta_1 + \theta_0) = \cos\theta_1 \cos\theta_0 - \sin\theta_1 \sin\theta_0, \tag{4.5}$$

and rearranging the equation

$$\frac{L_1}{L_2} = \frac{\cos\theta_2 \cos\theta_0 - \sin\theta_2 \sin\theta_0}{\cos\theta_1 \cos\theta_0 - \sin\theta_1 \sin\theta_0} \tag{4.6}$$

The cell was positioned at $\theta_1 = 10°$ and $\theta_2 = 9.33°$. Measurements were performed to yield $L_1 = 34.8265$ mm and $L_2 = 34.6404$ mm. Using equation 4.6, the retrieved values are $\theta_0 = 15.05$ and $L_0 = 31.54(85)$. This value differs from the values shown in figure 4.17 because this measurement was performed in different condition, after new assembly of the cell.

4.10.4 Gas circuit

The gas circuit is illustrated in figure 4.18. A turbomolecular pump station is used to remove air from the gas circuit and provide a clean atmosphere for the gas sample. Nitrogen is used to purge the circuit and provide extra effort to assure that there is no contamination with laboratory air. The pressure measurement is performed by two gauges, one for low pressures with 1 mbar span and one with 1000 mbar span. The lower limit in pressure reading is 1×10^{-4} mbar and the vacuum pump can be used to achieve pressures below this level.

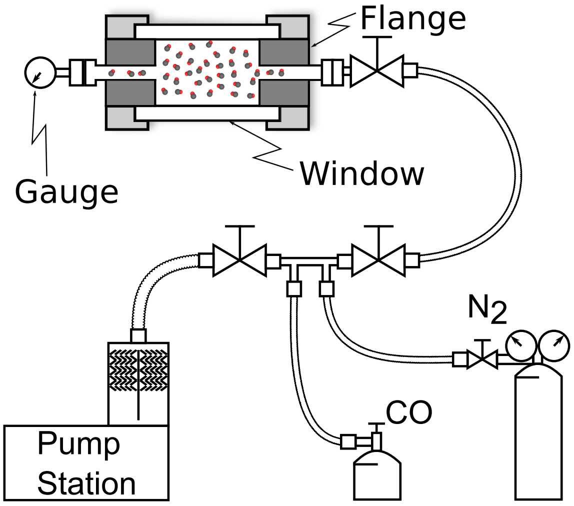

Figure 4.18: Experimental setup of the gas circuit used in the experiments.

To remove any contamination, the gas pressure is decreased below 1×10^{-4} mbar and it stays at this level for at least 24 hours. The circuit is filled with Nitrogen and left at low pressures completing one cleaning cycle. This process is repeated three times to avoid contamination with lab air. After this process, the carbon monoxide sample (Linde 99.997 %) is loaded into the cell.

4.10.5 Long term spectrum acquisition

The signal to noise ratio in the spectrum is increased by averaging the interferograms, as discussed in 5.2. In order to allow long term acquisition, the temporal overlap between pump and signal is stabilized. The strong dependence of MIR intensity noise on the temporal overlap between pump and signal is discussed in 3.2.5.

In order to estimate the improvement, long term measurements were performed using the delay stabilization. The comparison is illustrated in figure 4.19. Each spectrum is compared to the first acquired spectrum and the SNR is shown on the left panel. The right panel shows the averaged SNR in relation to the number of averaged spectra.

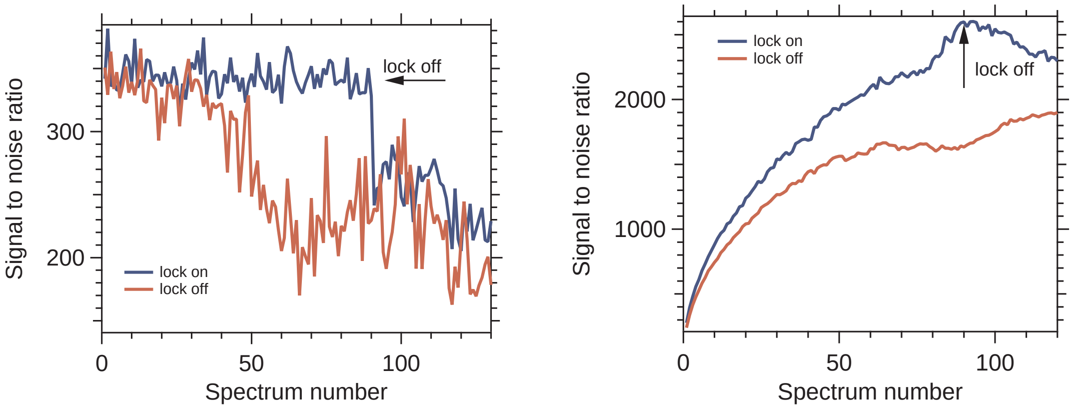

Figure 4.19: Comparison between the SNR behavior with and without stabilization of the temporal overlap between pump and signal.

5 Spectroscopy results

The Fourier transform spectrometer described in the previous sections was used to measure the R-branch of carbon monoxide on the fundamental absorption band ($1 \leftarrow 0$) at 4.6 μm. All measurements were performed at room temperature and in two broadening regimes. At low pressure, the absorption linewidth is Doppler limited and it was possible to resolve features narrower than the spectrometer nominal resolution using the frequency comb. The spectral bandwidth of the comb covered the complete R-Branch, allowing 23 transitions to be measured simultaneously with spectral elements separated by 15 MHz frequency steps. The low pressure measurements allowed the calibration of the FT grid via the frequency comb, which resulted in the high frequency accuracy for the high pressure measurements as well. At higher pressures, both pressure and Doppler broadening influence the linewidths and speed-dependent effects could be observed. The measurements presented in this chapter demonstrate that difference frequency generation is a viable light source for spectroscopy with precision, accuracy and high SNR.

5.1 Experimental conditions

The measurements were performed in two different pressure regimes. At pressures in the 10^{-1} mbar range, the line broadening is dominated by the Doppler effect due to the temperature. The FWHM Gaussian linewidth is in the 100s of MHz, while the Lorentzian contribution is around 1 MHz. In this condition, the absorption linewidth and the comb modes spacing are comparable. Absorption lines are resolved by using the FTS with sub-nominal resolution. Measurements in this regime were performed at 0.2 mbar.

For measurements at pressures above 400 mbar, the line broadening is mostly caused by pressure, with the Lorentzian linewidth around 4 GHz. In this regime, the nominal resolution of the spectrometer is sufficient to retrieve the lines and the necessary OPD is around 30 cm. However, the FTS grid calibration by the frequency comb from the low pressure experiments is maintained, because the measurements were performed at equal spectrometer conditions. In the high pressure regime, measurements were performed at 400 , 500, 700 and 1000 mbar

5.2 Time domain vs. frequency domain averaging

Averaging the signal to increase the SNR is an important step of the data analysis and it can be performed by averaging in the frequency domain (spectra) or in the OPD domain (interferograms). The average in frequency domain requires first that multiple FTs are performed to generate all the spectra. Instead, it is possible to perform the average of the interferograms first, before the Fourier transformation. The comparison between a single spectra and 100 averaged interferograms is shown in figure 5.1. The graphs on side show two regions of the spectrum. On panel A, it is possible to see that frequency and phase of the etalons are constant. It also shows that the etalons limit the SNR as it is not possible to decrease the noise below the etalons amplitude. On panel B at the edge of the spectrum, it is possible to see a sharp absorption feature from the CO inside the gas cell and a water line, from the lab atmosphere.

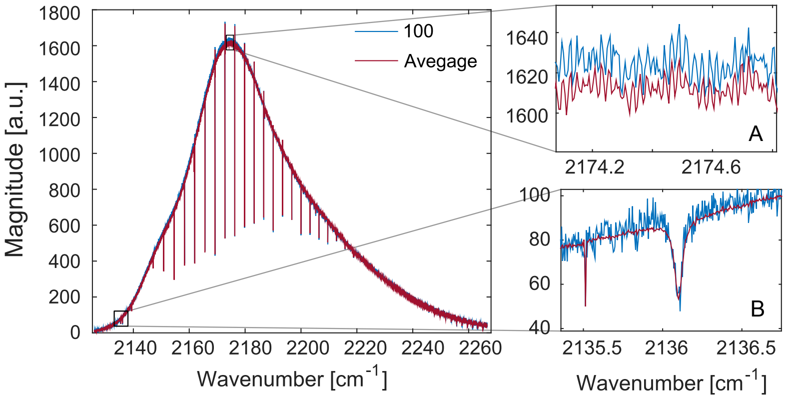

Figure 5.1: Comparison between a single spectrum and a spectrum with hundred averages performed in the interferogram. Panel A: the etalons are limiting the SNR as it is not possible to average below the etalons amplitude. Panel B: CO line and water line at the low intensity region of the spectrum. The CO line is narrow due to the low pressure in the cell and the water line is broad on atmospheric pressure.

As long as the phase of the frequencies composing the interferogram are kept constant during the measurement, the averaging in OPD domain does not introduce errors. Figure 5.2 shows a single scan interferometer in black and a hundred averages in orange. The OPD domain traces show that the phase of the oscillations can be averaged and it is possible to compare the averaged and the single scan features.

The interferograms (both single and averaged) were Fourier transformed and the spectral phase retrieved. Figure 5.3 shows a comparison between spectral phases to investigate the stability over a series of measurements. The phase of 100 spectra were averaged and the ration between the averages was compared to the first (orange trace) and the last (one

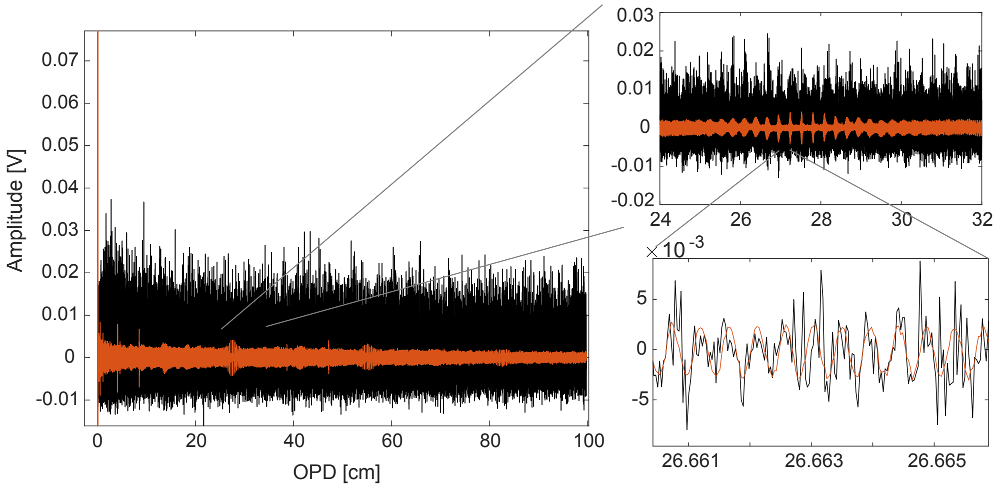

Figure 5.2: Black: single scan interferogram. Orange: average over 100 *interferograms. The features on the interferogram are below noise floor an can only be observed with averaging. The oscillations have the same phase and averaging in the time domain does not decrease the signal.*

hundredth) spectrum (black) The averaged compared to the first spectra shows a slightly smaller variation on the phase, which increases, specially at the edges where the optical power is low. This figure was generated with the spectrum shown in figure 5.1 and the frequency axis has the same range for comparison.

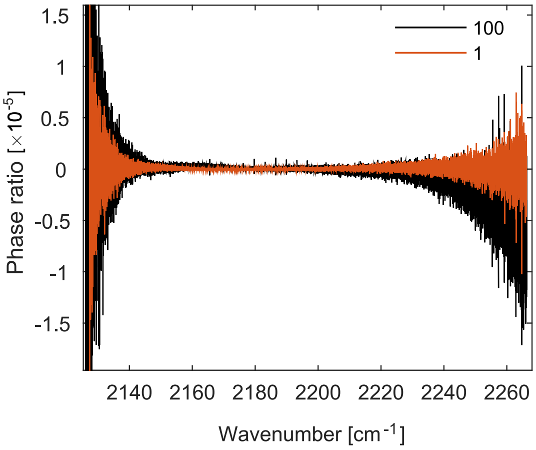

Figure 5.3: The ratio between spectral phases. Orange: the ratio between 100 *averages and the first scan. Black: the ratio between* 100 *averages and the last,* 100*th scan. Despite an increase, the difference is below* 1×10^{-5}.

In section 5.4.2, 100 interferogram were acquired for 8 scans of repetition rate. The OPD domain averaging decreases the manipulation time to achieve an interleaved spectrum from tens of minutes to a few seconds. The result is one averaged interferogram per repetition rate, which reduces considerably the number Fourier transformations to achieve an interleaved spectra, which for the 100 interferograms dataset is from 16000 to 16.

5.3 First low pressure results

The MIR spectrum was adjusted to cover the R-branch and the background spectrum (through the gas cell, without any sample) is shown in figure 5.4 (left) for a single scan at 150 MHz resolution. The plot on the right shows the ratio between spectra, which is used to evaluate the SNR of the measurement. The first acquired spectrum serve as reference and the subsequent spectra are compared to it. The procedure is performed diving the spectrum and taking the inverse standard deviation of the result over the FWHM of the spectrum. Changes in power and central wavelength appear as an offset from unity. The ratio between spectra offers the possibility to observe spectrum changes, which is a good way to evaluate the stability of the light source. Figure 5.4 (right) shows the comparison between the first and second spectrum, in blue; the first and the two-hundredth spectrum, in orange.

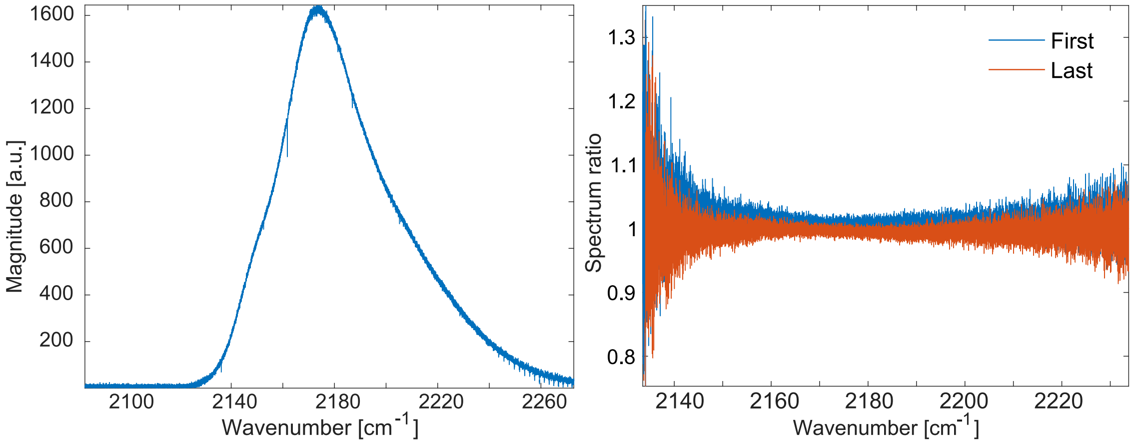

Figure 5.4: Output spectrum of the MIR source with no sample in the gas cell. Left: background spectrum used to perform the measurements at low pressure. Right: the ratio between the first spectrum and the second, and the ratio between the first and two-hundredth spectrum. The reciprocal standard deviation of the spectrum ratio, taken over the spectrum FWHM corresponds to the SNR_{sdt}.

The cell was filled with the CO sample to a pressure 0.20 mbar. Under this pressure, the estimated absorption linewidth is 150 MHz, mainly due to Doppler broadening as the Lorentzian FWHM is < 1 MHz. The center of the R-branch is at 4.587 µm corresponding to 65.354756 THz. The comb repetition rate is $f_{\text{rep}} = 150340580$ Hz and using the comb equation (with $f_{\text{ceo}} = 0$, canceled by the difference frequency generation) the comb mode number for line closest to the center of the spectrum is $n_{\text{comb}} = 435698$. The number of sampling points under the absorption line was chosen to be 8, which corresponds to approximately 18 MHz steps of the comb modes at 65.354756 THz. To achieve this change in optical frequencies, the reference laser frequency was changed in steps, which caused the repetition rate of the laser to change by $\Delta f_{\text{rep}} = 43$ Hz. Figure 5.5 shows the repetition rate steps performed during the measurement. For each of the eight repetition rate shift, 100 spectra were recorded and they were averaged to increase the SNR. For each measurement with the sample in the cell, one set of background measurement was performed.

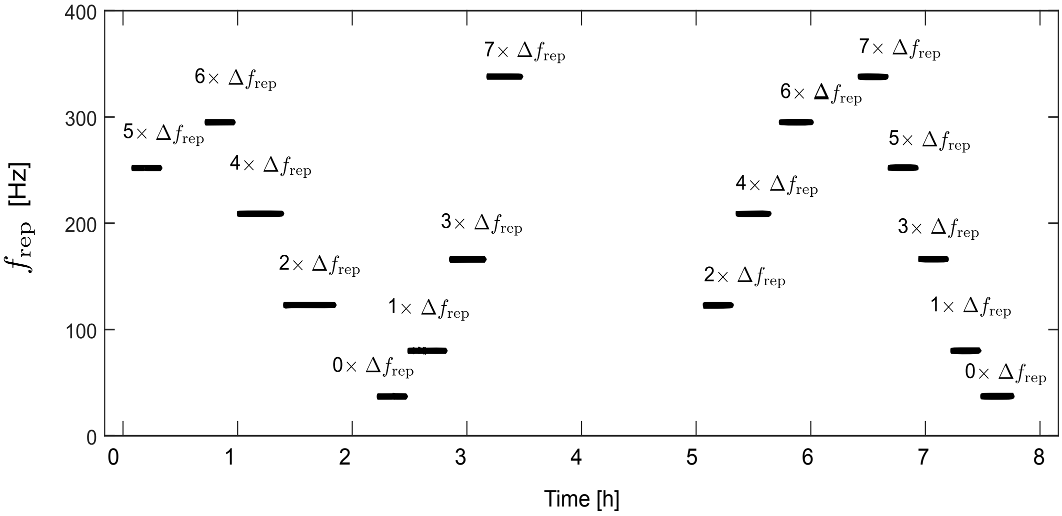

Figure 5.5: Repetition rate of the frequency comb employed during the measurements. The first set (from 0 *to* 4 *hours) were recorded during the sample measurements and the second set (from* 5 *to* 8*), the background.*

Interferograms were resampled and the length is chosen to be higher than c/f_{rep}, to allow the precise adjustment of the interferogram in a later step. Using equation 2.39, and assuming $\lambda_{ref} = 632.992$ nm, nominal resolution of $f_{\text{rep}} = f_{\text{FTS}} = 150323709$ MHz, the number of zero-crossings on each side of the interferogram is $N_0/2 = 3150560$. As discussed in the previous sections, it is usually not enough to choose the interferogram length based on the zero-crossings because the FTS grid needs fine tuning to match the comb spacing. It is possible to observe ILS distortion for two lines on the left spectrum in figure 5.6, which was processed with the closest interferogram length based on the zero-crossings. The plot on the right of figure 5.6 shows a zoom in one line where it is clear to see the ILS oscillation. The next sections will describe how the influence of the ILS can be reduced.

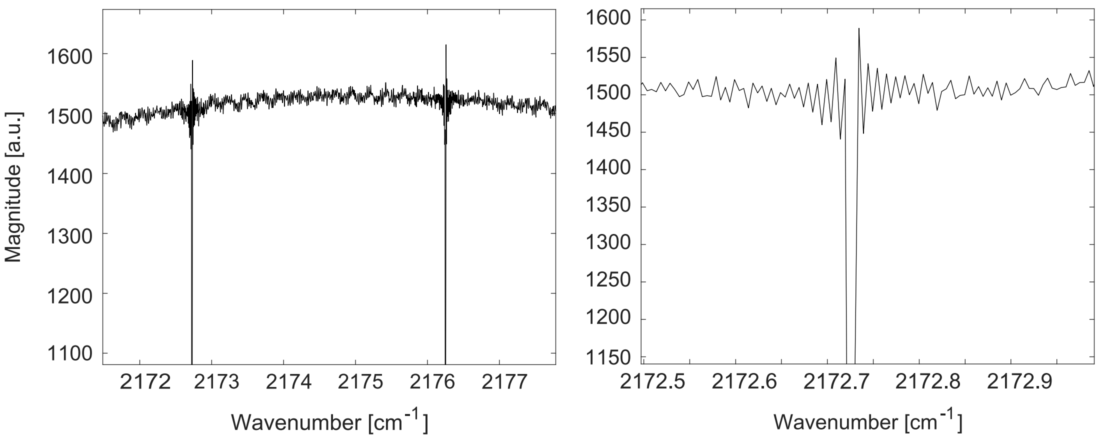

Figure 5.6: Measured spectrum with 0.2 mbar of CO in the gas cell. Left: overview spectrum without adjusting the interferogram length. Right: zoom in one of the lines to show the clear influence of the ILS and the oscillations on the baseline.

5.4 Calibration of the frequency grid

In conventional FT spectroscopy, calibration standards are commonly employed to correct the frequency grid [119]. Calibration standards are usually present at particular spectral regions and are affected, for example, by temperature and pressure. The frequency comb provides the calibration of the FTS grid due to the dependence of the ILS on the mismatch between the frequency comb grid and the FTS grid. It is possible to calibrate the frequency grid using any absorption feature without knowing its center frequency, as long as it is narrower than the frequency comb spacing.

The ILS is visible in the spectrum from figure 5.6 because the FTS has not enough resolution to resolve the absorption line. As described in section 2.5.2, when the FTS grid matches the frequency comb grid, only the spectral components on the top of the comb modes are sampled, the convolution with the ILS is performed at the correct steps and it does not affect the spectrum.

The FTS grid spacing (f_{FTS}) is inversely proportional to the maximum OPD (equation 2.40), which is sampled at discrete points on the zero-crossings of the reference laser. The discrete length of the interferogram (N_0) is calculated using equation 4.3.

The frequency of the comb modes is measured to kHz accuracy and it is considered to be a fixed grid, whereas the wavelength of the reference laser provides the FTS grid. The reference laser is calibrated from the manufacturer to 1 MHz accuracy and stabilized with a relative stability of 2×10^{-9}, or 1 MHz. In addition, an optical heterodyne beat with the comb was performed to evaluate its stability (the results are on appendix B on page 119).

Considering 1 MHz frequency change of the reference laser, the corresponding change in the FTS grid at the MIR optical frequencies is about 130 kHz.

The refractive index of air for the reference laser and for the MIR play an important role in the accuracy of the frequency axis, as it shifts both comb and reference laser frequency. The refractive index for the reference laser depends on temperature, pressure, humidity and CO_2 concentration in the air [118]. The accuracy in the refractive index for the MIR is affected by several absorption bands in the spectral region of interest [120]. In addition, the angle between the MIR and the reference laser needs to be considered for an accurate calculation of the frequency grid. The detailed procedure to match the FTS grid to the comb grid ($\nu_{\text{FTS}} = \nu_{\text{comb}}$) is described in the next sections.

5.4.1 Frequency grid mismatch

The frequency comb lies on a frequency grid (ν_{comb}) given by the comb equation (equation 2.30). The FTS frequency grid (ν_{FTS}), calculated from equation 2.40, is quantized by the zero-crossings of the reference laser wavelength. In order to remove the ILS from the spectrum, it is necessary to adjust the FTS grid to match the comb grid.

The measurement is performed in air and the refractive index needs to be taken into account for an accurate calculation of the FTS frequency grid. The refractive index of air for the reference laser (n_{HeNe}) is calculated using Ref. [118]. It is necessary to account for the refractive index of the MIR frequency comb (n_{comb}) as well, to yield a frequency axis in vacuum. For convenience, all mechanisms that shift the frequency components can be applied as a correction coefficient on the reference laser wavelength. The reference laser wavelength in vacuum (λ_{vac}) is corrected by the refractive indexes

$$\begin{aligned}\lambda_{\text{ref}} &= \lambda_{\text{vac}}\left(\frac{n_{\text{comb}}}{n_{\text{HeNe}}}\right)\\ \lambda_{\text{ref}} &= 632.9909178\ [\text{nm}]\left(\frac{1.000266605800}{1.000270280384}\right) = 632.9885924\ [\text{nm}]\end{aligned} \tag{5.1}$$

The number of points in the interferogram is calculated from equation 2.39. The CO R(7) line was measured with several repetition rates, including $f_{\text{rep}} = 150340580.003$ Hz. Using λ_{ref} from equation 5.1, the number of points is

$$N_0 = \frac{2 \times 299792458\ [\text{m/s}]}{632.9885924\ [\text{nm}] \times 150340580.003\ [\text{Hz}]} \approx 6300552 \tag{5.2}$$

The number of points gives the length of the interferogram. After FT, the frequency spacing of the FTS grid is

$$f_{\text{FTS}} = \frac{2c}{\lambda_{\text{ref}} N_0} = \frac{2 \times 299792458 \text{ [m/s]}}{632.9885924 \text{ [nm]} \times 6300552} = 150340577.798 \text{ [Hz]} \tag{5.3}$$

The difference between the frequency grids ν_{comb} and ν_{FTS} can be calculated by

$$f_{\text{diff}} = -n_{\text{opt}}(f_{\text{FTS}} - f_{\text{rep}}), \tag{5.4}$$

where n_{opt} is an integer corresponding to the optical frequency in question. It is calculated assuming an optical frequency on the spectrum, for example, the R(7) line center (taken from HITRAN database [5]) at $\nu_{\text{R(7)}} = 65.137670879$ THz, which leads to

$$n_{\text{opt}} = \nu_{\text{R(7)}} / f_{\text{rep}} = 433267.39 \approx 433266. \tag{5.5}$$

The mismatch between ν_{FTS} and ν_{comb} under these conditions is

$$f_{\text{diff}} = 955351 \text{ [Hz]} \tag{5.6}$$

5.4.2 Adjusting the frequency grid

The amplitude of the ILS oscillations reflects the residual mismatch between the comb grid and FTS grid. The mismatch can be caused by factors not taken into account yet, such as the alignment between MIR and HeNe trough the interferometer, and the refractive index of air for both the comb and the reference laser. It is possible to change the FTS grid by changing the interferogram length. The result is a shift in the FTS frequency grid. However, the mismatch between the grids is much smaller than the change of one point on the interferogram length. Figure 5.7 illustrates the effect in one line for different number of points in the interferogram.

The observed line shape repeats itself every time the FTS grid under the absorption line changes the equivalent to one repetition rate in the spectrum. On the other hand, the frequency grid calculated from equation 2.40, shifts continuously moving the center of the line in the frequency axis. Constrains in the experimental conditions and the accuracy of the estimations provide initial guesses that result in accuracy of the frequency grid much higher than one repetition rate. For example, the initial calculation of the reference laser wavelength is know to an accuracy better than one repetition rate. In addition, the

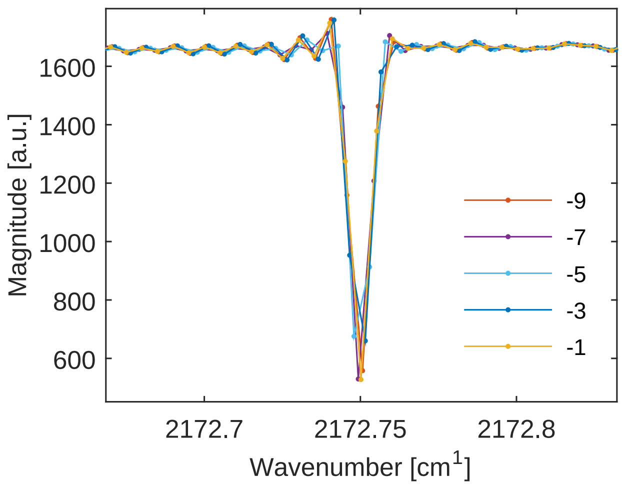

Figure 5.7: The instrument line shape and the line profile change in relation to the interferogram length. The legend shows the number of removed points from the correct interferogram length.

change of the ILS amplitude is much stronger compared to the frequency change of the line center due to the change of the correction coefficient.

Figure 5.8 shows the interleaved spectrum with the FTS frequency grid calculated solely from the repetition rate.. The legend shows the individual measurements starting at $f_{rep} = 150340537$ MHz and the steps Δf_{rep} =43 Hz. It is possible to see that the ILS amplitude is higher for few of the lines. The reason is that the frequency grid change due to a change in the interferogram length is not sufficiently small due to the discrete sampling of the OPD. It is only possible to achieve the closest match $\nu_{fts} \approx \nu_{comb}$ for a certain spectral range. For example, at 2150 cm^{-1}, the comb mode number $n_{2150} \approx 428729$ and at 2120 cm^{-1}, $n_{2120} \approx 422747$. For a change one point in N_0, the change is 300 kHz higher at 2150 cm^{-1} than at 2120 cm^{-1}.

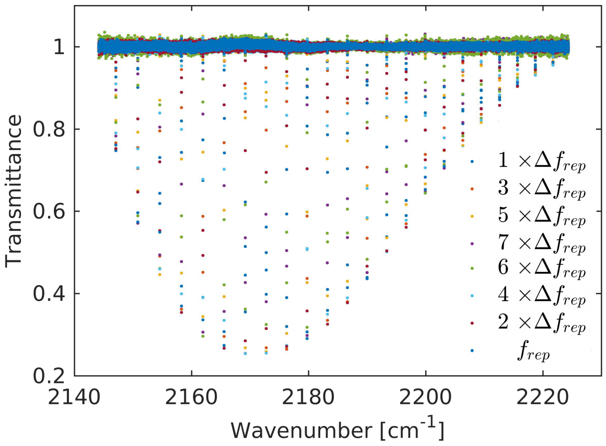

Figure 5.8: Transmittance spectrum after optimizing the interferogram length. At this magnification, most of the lines present ILS at the baseline level.

5.4.3 Zero-padding tests

The difference between ν_{FTS} and ν_{comb} lies on the fact that the interferogram is sampled at discrete points, on the zero crossings of the reference laser. Zero-padding the interferogram ($k_{pad} \geq 1$, on equation 2.41) reduces the frequency change of the FTS grid by changing the number of points in the interferogram.

The optimization routine was performed as in the previous section using zero padding. The available GPU memory (NVIDIA Tesla K40 - 12 Gb) limited the padding factor to eight. Figure 5.9 shows the change on the line center with the interferogram length different by one point at each side of the interferogram ($\Delta N_0 = 2$) for, $k_{pad} = 2$ on the top, and $k_{pad} = 8$ on the bottom.

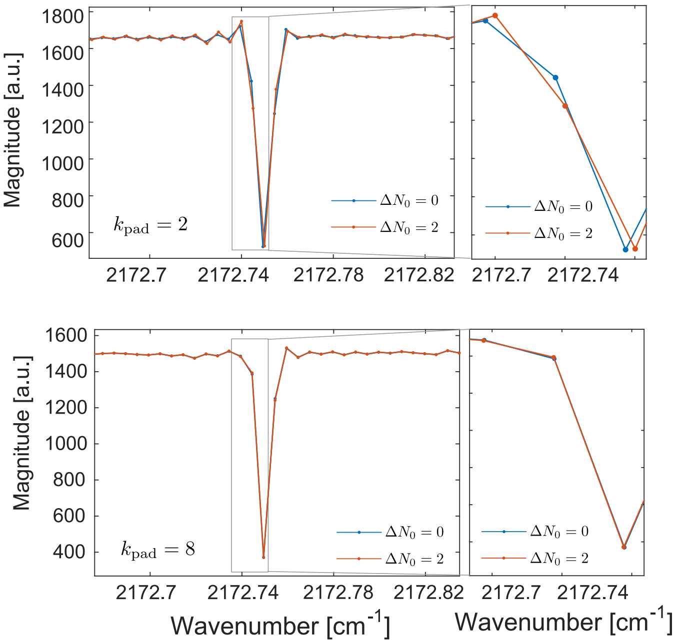

Figure 5.9: Changes in the absorption line for different padding factors and interferogram lengths. Padding the interferogram generates an interpolated spectrum. The graphs show interferograms processed with one point difference in the padded interferogram. Top: padding factor equals two. Bottom: padding factor equals eight. The graphs on the right side shows a zoom in the lines.

Padding the interferogram generates interpolated points between measured points. For a correct retrieval of the absorption line, the final spectrum should contain data points solely at the nominal resolution spacing and the interpolated data points removed. Using the padding, it was possible to shift the FTS scale ν_{fts} by a fraction of the 150 MHz original spacing. The difference between $f_{fts}(N_0)$ and $f_{fts}(N_0{+}2)$ is 23.8 Hz for $k_{pad} = 0$ and 2.65 Hz for $k_{pad} = 8$.

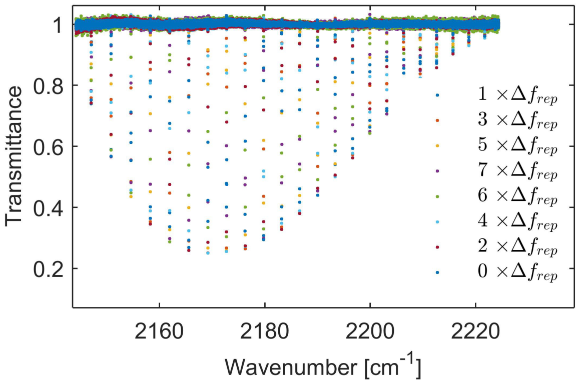

Figure 5.10: Interleaved spectrum with the optimization routine performed for eight times padding factor.

The repetition rate of the laser sets the necessary nominal resolution. In this study, the repetition rate of the laser is higher than previous works that reported FTS spectroscopy with sub-nominal resolution [89, 88]. The interferogram length is directly connected to the size of the file, which is decreased by a factor of four, for example, if the laser repetition rate would be 600 MHz. In this situation, it could be possible to apply a higher padding factor and match $\nu_{fts} = \nu_{comb}$ over a broader spectral bandwidth. However, at 150 MHz technical limitations in computer processing power limited the application of padding to solve the mismatch between $\nu_{fts} = \nu_{comb}$ and a second method was applied to correct the axis.

5.4.4 Offset of the Fourier transformation grid

A complementary approach zero-padding, is to multiply the interferogram by an exponential function to shift the origin of the FTS grid using equation 2.42. The small discrepancy between the comb spacing and the FTS grid (as shown in section 5.4.1) can be compensated by shifting the origin of the FTS grid to achieve locally a matching scenario, $\nu_{\text{comb}} = \nu_{\text{fts}} + f_{\text{shift}}$. The required shift is calculated by using equation 5.4 and is in the order of a few MHz.

The routine for minimizing the ILS is performed by calculating the f_{shift} for each one of the repetition rates. The shift is applied to the interferogram using equation 2.42. The standard deviation on the baseline close to the absorption line is calculated and act as one of the quality factors.. The second quality factor is the width of the interleaved absorption line. The mismatch between the grids results in a convolution of the spectra with the ILS, which causes additional broadening of the absorption line. A correction coefficient, η, is applied to the reference laser wavelength, $\lambda_{\text{eff}} = \lambda_{\text{ref}}\eta$. The correction coefficient η is changed and both the ILS amplitude and the linewidth recalculated. A clear minimum is achieved when the FTS grid and the frequency comb grid are equal under the absorption line, as shown in figure 5.11. The frequency shift moves the whole FTS grid by the same amount $\nu_{\text{fts}} = nf_{\text{fts}} + f_{\text{shift}}$, which corresponds to a relative frequency shift in the 10^{-8} level for $f_{\text{shift}} = 1$ MHz.

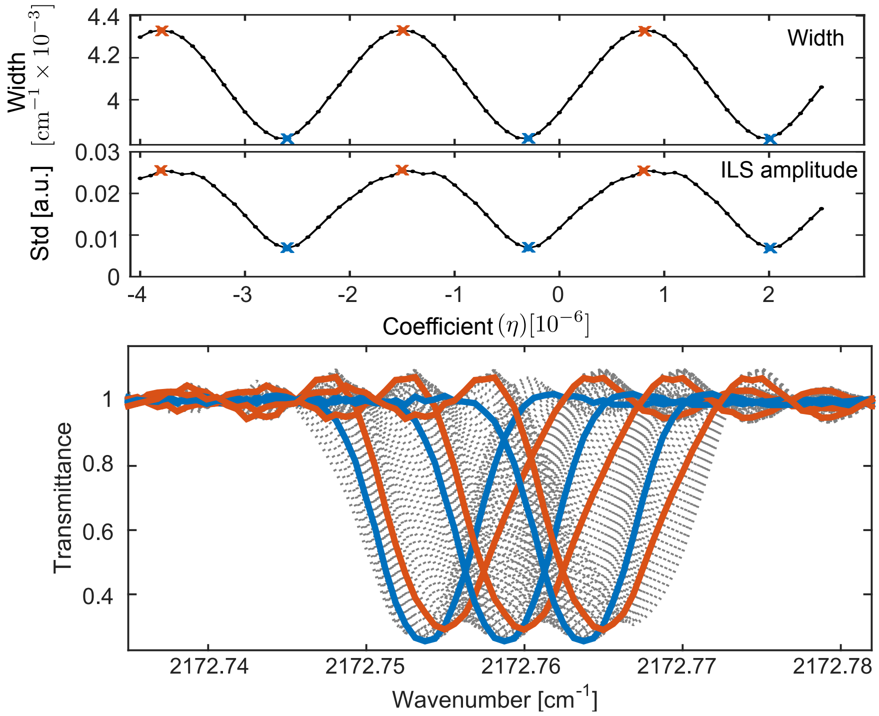

Figure 5.11: Typical optimization results illustrated with the R(7) line. Top: Gaussian width and standard deviation of the ILS amplitude in respect to the correction coefficient. The blue marks and the red marks show respectively the minimum and maximum linewidth and ILS amplitude. Bottom: change of the interleaved absorption line in respect to the coefficient values on the top graph. The minimum (and maximum) are shown in blue (red).

The minimum condition is achieved every time the FTS grid is shifted by one repetition rate and is not sufficient to provide the accuracy of the frequency axis. On the other hand, there are limiting conditions that assures that the correct minimum is obtained. The initial accuracy calculated from the known parameters is close to the optimum position, as can be seen from figure 5.11, and the correction coefficient is -3.4×10^{-7}. The absorption line center frequency changes by one repetition rate as the ILS amplitude or the minimum width repeats itself. The center of the line is known typically to higher accuracy (30 MHz) than one repetition rate ($\approx$ 150 MHz). Figure 5.11 shows an extreme case for illustration purpose only, for the line center to shift by three times the repetition rate. The correction coefficient in figure 5.11 was changed by more than the one order of magnitude (7×10^{-6}) from the necessary (3.4×10^{-7}).

5.4.5 R(7) line at 2172 cm^{-1}

The strongest absorption line of the R-branch was chosen to asses the quality of the spectrum. The gas cell temperature was monitored during the acquisition via resistance temperature detector (RTD), which was calibrated to 0.01 °C accuracy. The temperature is 19.995 °C with 0.015 standard deviation over 12 hours. The estimated FWHM Gaussian width at this temperature is 150.916 MHz. The pressure was monitored and recorded before each measurement and it is shown in figure 5.12. The Lorentzian FWHM linewidth for a pressure of 0.2035 mbar is 0.81270 MHz.

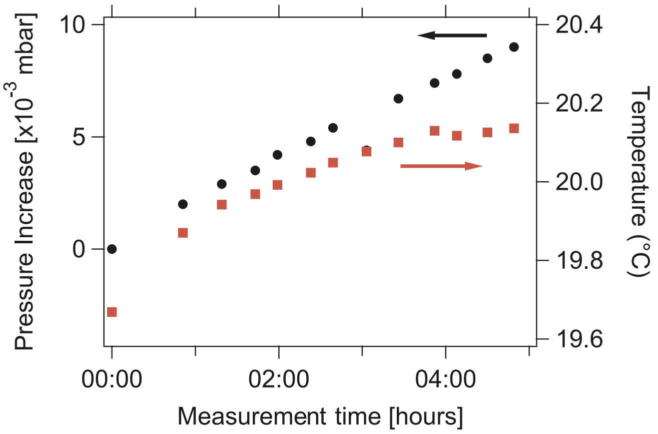

Figure 5.12: Recorded pressure values during the measurements.

Figure 5.13 shows the R(7) line at 2172 cm^{-1} and the fitted Voigt profile. The fitting converged yielding a quality factor (standard deviation of the residuals, QF) of QF $= 198$. Except for the small oscillation at 0.2 GHz, the ILS is not clearly observed in the residuals.

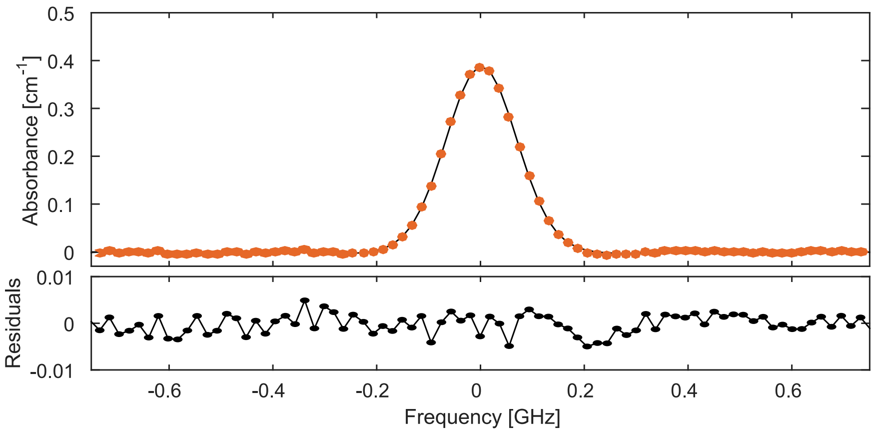

Figure 5.13: The R(7) line and the residuals for the VP fit. The line can be resolved via interleaving eight repetition rate scans.

Figure 5.14 show the R(5) at 2165 cm^{-1} and the R(9) at 2179 cm^{-1} to illustrate the effect of the mismatch of the frequency grids for comparison with the optimized line in figure 5.13.

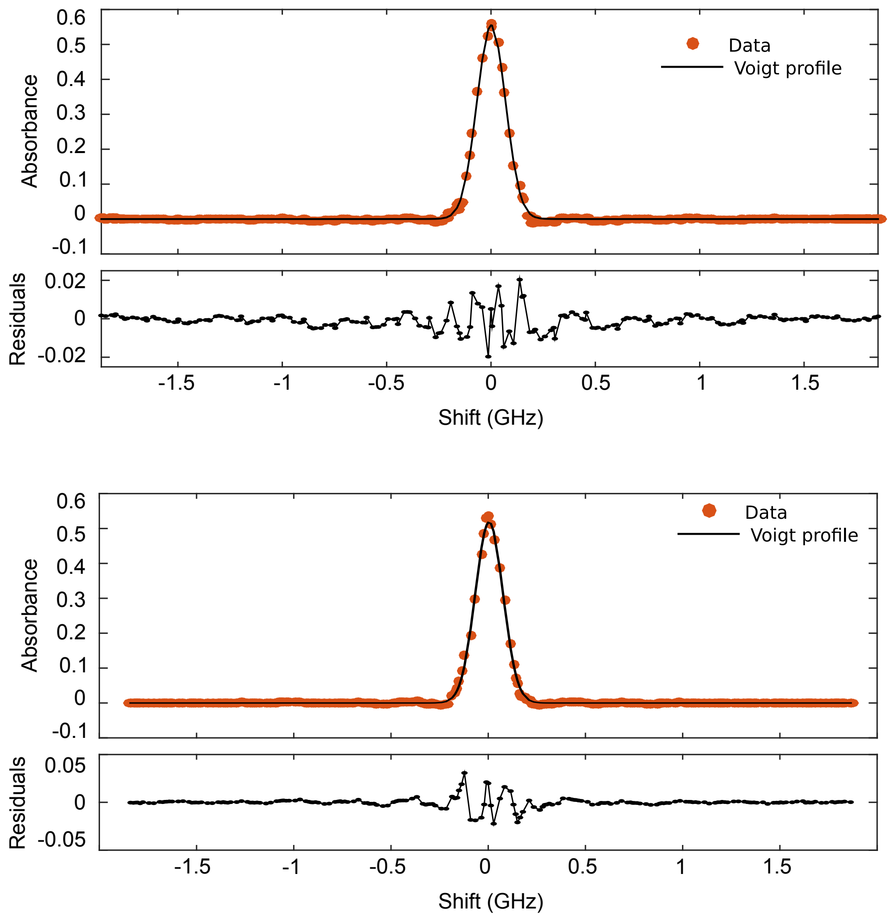

Figure 5.14: Interleaved spectrum showing the lines R(5) and R(9) with a mismatch between the FTS and comb grid, illustrates that the noise at the center of the absorption line is observed at other spectral regions.

The offset of the FTS grid results in a local match between the frequency grids. Due to the periodicity of the grids (f_{rep} for the comb, and f_{FTS} for the FTS grid), the grid mismatch is different for spectral regions away from the optimized frequency. To investigate the effect of the grid mismatch over the complete bandwidth covered by the comb, the VP was fitted to all the lines composing the R-branch and the result is shown in figure 5.15. It is not possible to see a clear influence of the ILS on the residuals.

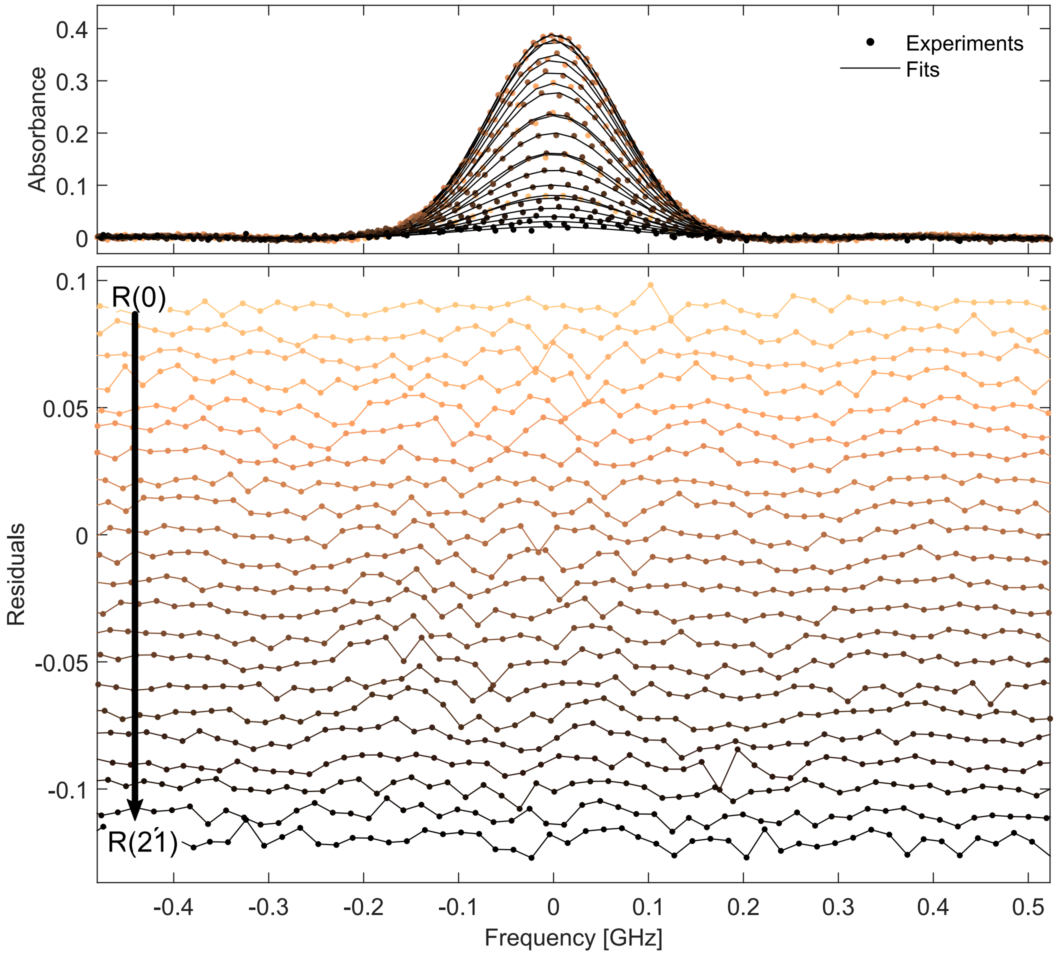

Figure 5.15: Interleaved spectra for the complete R-branch and the residuals from the Voigt profile. The residuals show from top to bottom the R(1) to R(23) and no clear ILS influence is observed.

Although not observed in the residuals, the retrieved Gaussian linewidths show that the ILS is present. As the correction coefficient was calculated observing the R(7) line, the effect of the mismatch is expected to be small for lines close to the R(7) line and to increase for further lines. It causes an increase in the linewidths and the effect is higher for lines further from the R(7) line. Figure 5.16 shows the FWHM Gaussian linewidth for all the lines in the R-branch. The error bars shows one standard deviation calculated from the fitting of the Gaussian linewidth.

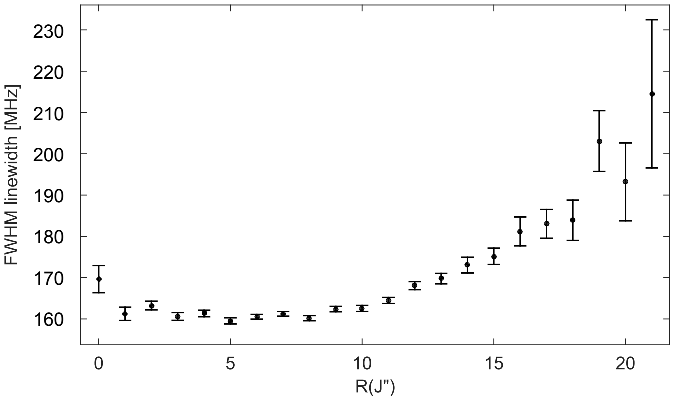

Figure 5.16: Retrieved absorption linewidths versus transition number. The increase in the linewidth is cause by the mismatch between the comb and FTS grid, which is higher for frequencies further from the optimized line, the R(7) in this case.

The FWHM linewidth of the R(7) line, retrieved from the Gaussian fit is 159 MHz, which is 9 MHz broader than the calculated 150 MHz. The necessary pressure or temperature to cause this effect would be more than 10 times higher than the estimated values. Therefore, the effect was attributed to residual ILS influence on the measurement, which is discussed next.

5.4.6 Residual instrument line shape

The assumption was that the line broadening was connected to the stability of the comb modes. The performance of the comb is monitored via the beat notes from phase locked loops and the repetition rate, which is recorded during the measurement. Figure 5.17 shows the repetition rate values from the counter during one of the measurements.

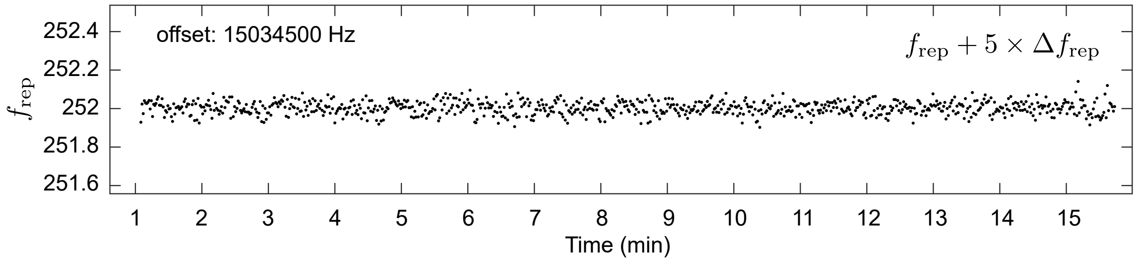

Figure 5.17: Frequency counter values recorded during the measurements for a repetition rate of $f_{rep} + 5 \times \Delta f_{rep}$.

Repetition fluctuations are on the order of 100 mHz and they are caused by frequency drift of the reference laser. A slow feedback is performed to the temperature of the laser to keep the reference laser at a certain frequency. However, the slow bandwidth of this feedback loop is not sufficient to maintain the frequency stable. As the optical beat between the comb and the reference laser is stabilized by the PLL of the repetition rate, fluctuations of the reference laser frequency are transferred to the comb. This is the main contribution to the changes observed in the repetition rate. The comb mode number is in the range of $n_{\mathrm{MIR}} \approx 430000$ it corresponds to a variation of the comb frequency of 43 kHz.

The stabilization was modified and an additional phase locked loop introduced to control the reference laser was performed (as described in section 3.1.3). Repetition rate fluctuations were decreased to 1 mHz, which corresponds to ≈ 430 Hz fluctuation for the comb mode at the center of the spectrum at 65.354756 THz. The comb modes stability was improved by a factor of 100 which was enough to eliminate the comb as a source for the broadening of the lines. New measurements were performed and the results described in the next section.

5.5 Second low pressure results

In addition to the frequency comb stability, the previous measurement showed that etalons were limiting the SNR. The angle between the gas cell and the MIR beam was increased to avoid reflections from the wedged windows. To increase the pressure accuracy, the gauge was changed to a MKS (690A11TRA) with 0.05% accuracy (in comparison with 0.1% from the Pfeiffer). To provide comparable absorption strength to the first measurement, the sample pressure was 0.2085 mbar. Additional improvements in the electronics and interferometer alignment were performed, which contributed to an overall SNR increase. The overlap of the MIR beam in the interferometer was improved. The balanced detection was changed and the polarity inversion performed close to the detector housing. The time domain SNR increased from 2000 to 4000 and the number of averages could be decreased from 100 to 10. Because of the shorter acquisition time, the repetition rate scans were increased from 8 to 10. The recorded values from the frequency counters are shown in figure 5.18.

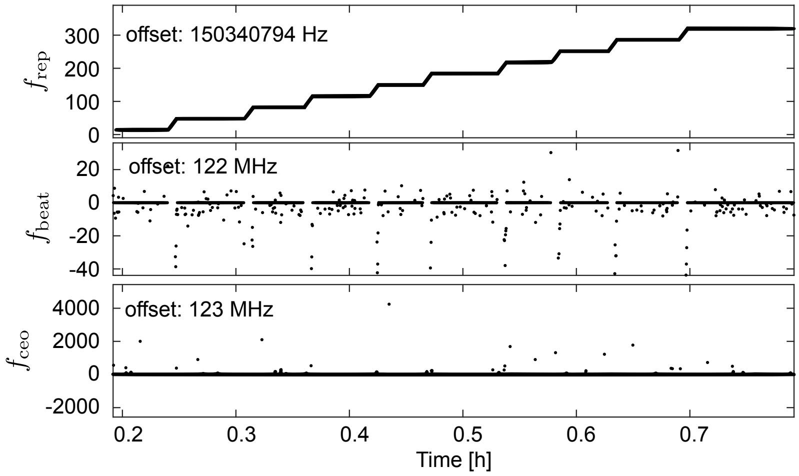

Figure 5.18: Recorded values from the frequency counters used to monitor the laser stabilization.

The interferograms were processed as described in the previous sections, with the OPD domain averaging and correction coefficient calculated. The amplitude of the etalons decreased because of the cell angle and it is possible to see the ILS clearly. When the mismatch is high, the oscillations can be observed for a longer range. The R(7) line is shown in figure 5.19 after the processing and finding the correction coefficient.

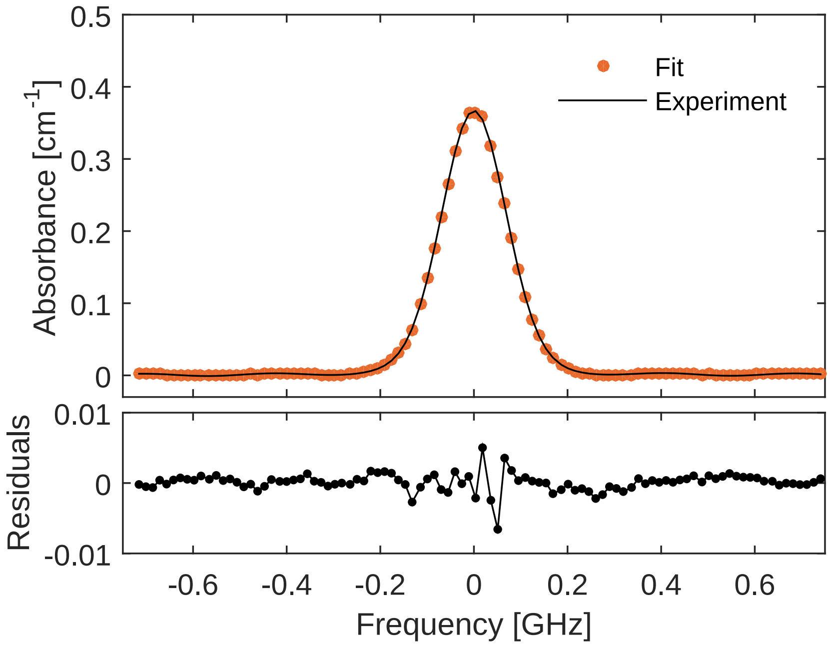

Figure 5.19: Interleaved spectrum showing the R(7) line and the VP fit using the sub-nominal method.

The quality factor of the fitting is 285 and the correction coefficient was found to be -8.4×10^{-7}. Such difference corresponds to a change of the frequency grid by 2 MHz at 65 THz which is the same order of magnitude that a change in 1 mbar of atmospheric pressure or 0.5 K of temperature on the laboratory air.

The retrieved Gaussian linewidth for the R(7) line in the second measurement was 156 MHz, which is 6 MHz broader than the calculated 150 MHz. Despite the broadening of the line, the overall performance of the system was improved and the stabilization of the comb is in a level that can be excluded.

One factor that can influence the measurement in such a way is the divergence of the MIR beam, as in traditional FTS with incoherent light source. The maximum beam divergence (calculated from formula 2.38) is 1.5 mrad, which is higher than the 0.8 mrad for the MIR beam. However, the effect on the absorption line is small and considering that both the formula and the calculations are estimations, it is possible that the divergence is affecting the measurement.

The measurements at sub-nominal resolution cannot be used to estimate the intensity of the lines, due to the external broadening. Nevertheless, they still provide the calibration of the the frequency grid, which can be used to retrieve information about the center frequency of the lines as will be subsequently demonstrated. The correction coefficient provides the indirect calibration of the OPD via the frequency comb, which can be used in the high-pressure measurements to achieve the frequency accuracy. The next section describes the measurements at the pressure broadening regime, and the results from the first and second low pressure measurements are presented combined at the end of the section.

5.6 High pressure

Sections 5.3 and 5.5 discussed the experiments in low pressure condition, where the absorption lines are not affected by collisional effects. The line broadening was dominated by temperature and the line shape is described by a Gaussian profile. Pressure has not a measurable effect in the line center or linewidth. Moreover, it was showed that the residual ILS observed in the vicinity of the absorption line depends on the agreement between the FT grid and the frequency comb structure. This dependence is explored to find the correction coefficient (η) for the absolute calibration of the OPD, which provides the accuracy of the frequency spacing in the FT grid.

This section presents results from a regime which pressure dominates the absorption line broadening and causes the center of the absorption line to change. The frequency accuracy is equally calibrated by the correction coefficient found on the low pressure measurements, due to the equal experimental conditions.

5.6.1 Measurement condition

Carbon monoxide is mixed with nitrogen to provide a sample transmitting $\approx 30\%$ of the incident light and FWHM absorption line width in the GHz range. Measurements were performed in four different pressures and 200 interferograms recorded for each pressure.

The gas cell under vacuum, $< 10^{-4}$ mbar, is filled with 5.07 mbar of CO and nitrogen is included to reach a pressure of 991.3 mbar. The sample pressure was decreased in steps and the transmission measured at 991.3, 702.13, 497.27, and 400.00 mbar. Figure 5.20 shows the overview spectra of the CO R-branch and parameters will be reported for the indicated lines.

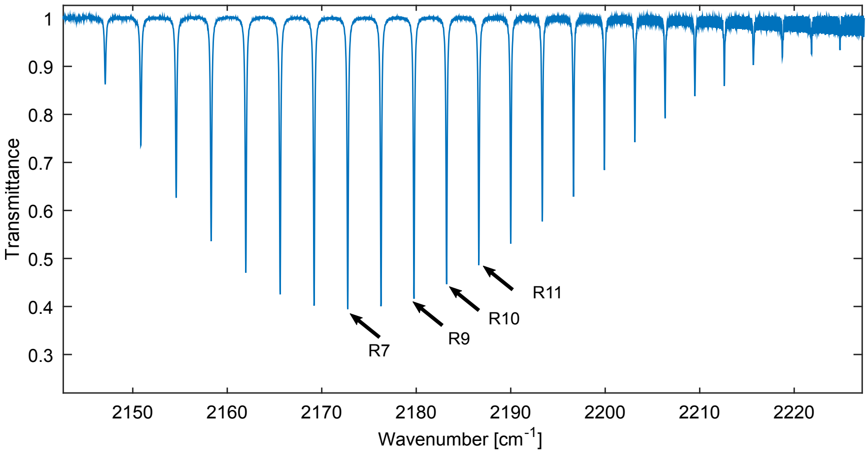

Figure 5.20: Overview spectra showing CO R-branch for the mixture at 991.3 *mbar.*

5.6.2 Speed-dependent effects

The R(7) line was chosen to illustrate steps of the data processing because it provides the strongest absorption and the highest SNR ≈ 1500. The data analysis is equally performed for the other lines.

Figure 5.21 shows the fitting results for the R(7) line at four pressures. The line shape was fitted using the Voigt profile (VP) and the speed-dependent Voigt profile (SDVPq), with quadratic approximation. The residuals of the VP demonstrated that speed-dependent effects were observed and the quality factor is improved when the line shape is modeled by the SDVPq.

The next sections describe retrieval of the line parameters from the fitting procedure using the speed-dependent Voigt profile with quadratic approximation (SDVPq). The fittings were performed using the software described in Ref. [121]. Line strengths, line center, pressure broadening coefficients are reported for four transitions. The results from the fitting of the additional lines are in the appendix C, on page 120.

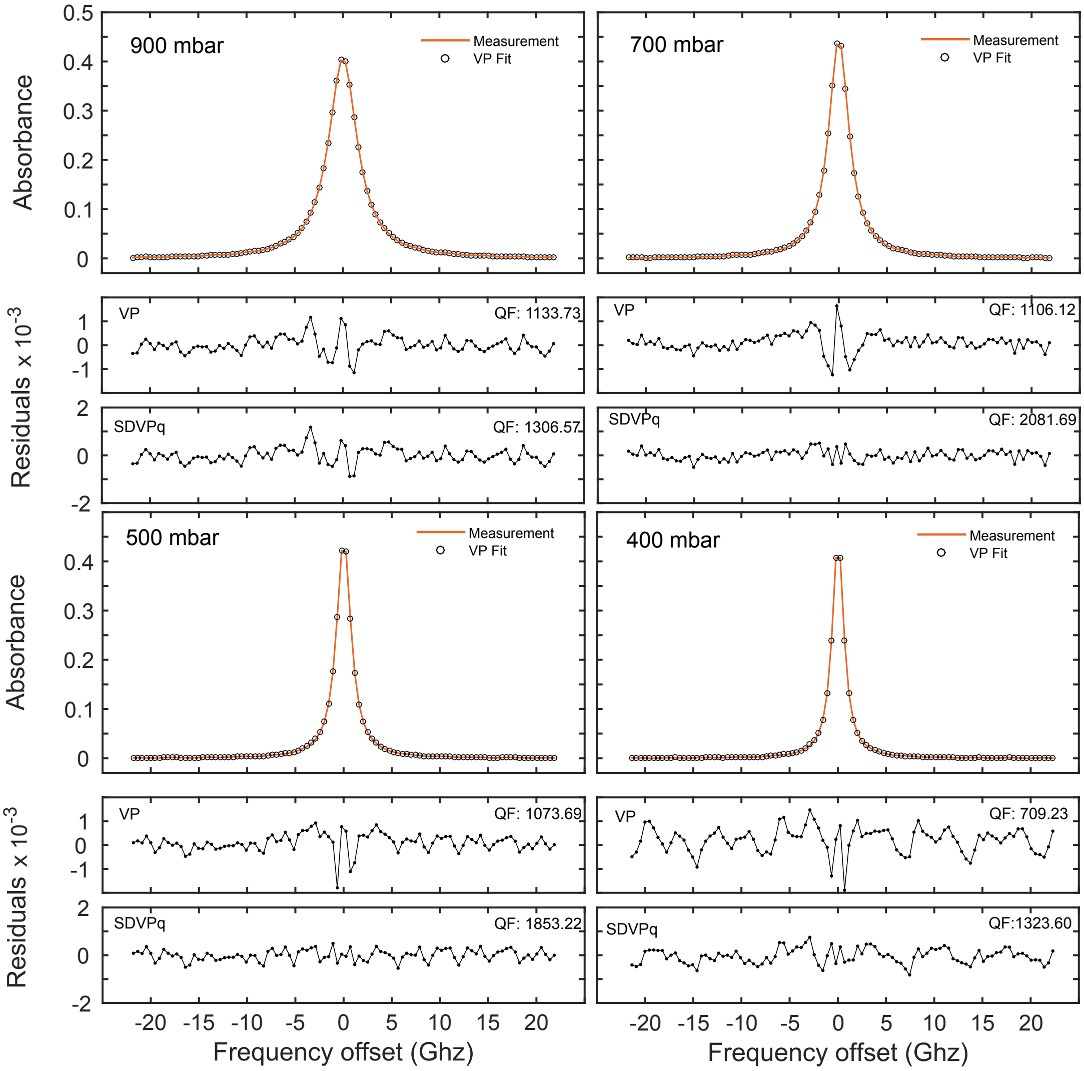

Figure 5.21: The R(7) line and fit results at four pressures. Speed-dependent effects can be observed in the residuals when the VP is used. The SDVP shows increased agreement between the measurements and the model.

5.6.3 Line strength

The SDVPq was chosen to be the model and the fitting was performed individually for each line and each pressure. The line strength S per molecule is calculated from the area of the line divided by the number of molecules in the respective pressures (described in section 2.2). The temperature and pressure are recorded for each measurement and they are employed to calculate the number density. The line intensity is corrected for temperature using a the correction based on total partition sums [52, 53]. Table 5.1 summarizes the result from the calculated values of line intensity of four transitions. The accuracy represents one standard deviation from the area fitting and a summary of accuracies are presented in section 5.7. The values retrieved from the measurements at 991.3 mbar were not included in the calculation. The calculated line intensities were on average 8.8% lower than the values from the other three pressures, and the difference was consistent over the lines. It points to an systematic error on the highest pressure reading.

Table 5.1: Retrieved values of line strengths for the lines R(7), R(9), R(10), and R(11) and the comparison with data on the literature.

Pressure [mbar]	**R(7)**	**R(9)**	**R(10)**	**R(11)**
	$[10^{-19}\mathrm{cm}^{-1}/(\mathrm{molecule}\cdot\mathrm{cm}^{-2})]$			
400	4.45020	4.070721	3.707128	3.278977
497.27	4.45459	4.065648	3.700965	3.286206
702.13	4.46240	4.040709	3.700129	3.287111
Mean (293.72K)	4.45459	4.065648	3.700965	3.286206
Corrected (296K)	4.4384(43)	4.0609(23)	3.7020(23)	3.2923(24)
Ref. [5]	4.55(6)	4.16(2)	3.80(5)	3.38(7)
Ref. [122]	4.47(7)	4.18(8)	3.80(5)	3.36(9)
Ref. [123]	4.3347(22)	3.9786(12)	3.36579(9)	3.2668(7)

5.6.4 Line center versus pressure

The Gaussian linewidth, Γ_D, is a function of the temperature, which is known from the temperature measurement of the gas to 1 mK accuracy. This parameter is calculated and fixed at $\Gamma_D = 151.387$ MHz. The free parameters for the fitting are the Lorentzian linewidth (Γ_L), the integrated line strength, S, the speed-dependent width, a_w, and the center of the line at the pressure P, $\nu(P)$. The pressure increase causes the line center to linearly shift from its vacuum value. Figure 5.22 shows the center of the line for measurements performed at three pressure values. The highest pressure (991.3 mbar) was not included in the calculations because the analysis of the line intensities suggested a systematic error on the pressure readings at this particular pressure.

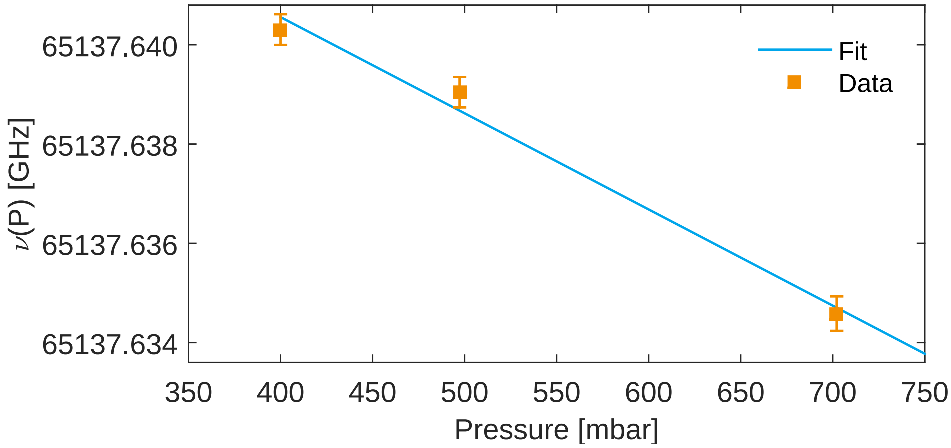

Figure 5.22: Center frequency of the R(7) line versus gas cell pressure. Linear regression is performed to retrieve the value of the line center in vacuum.

The line center in vacuum is found taking into consideration the three lowest pressures. Linear regression is performed to find the line center in vacuum of $\nu_0 = 65137.67394$ GHz. This value is in good agreement with the value found in the low pressure cases, 65137.66968 GHz for the first and 65137.67094 GHz for the second run. Once the position of the line, ν_0, is known it is possible to analyze smaller effects on the line. The shift of the line center is caused by collisions with the perturbing gas, N_2 and represented by δ_{N_2}. In addition to the collisional shifting, the speed-dependent shift, a_s, is also included in the model. Figure 5.23 shows the changes in the line before and after considering the speed-dependent shift parameter.

Although the SNR in the line is close to the limit for observing the asymmetry in the line caused by the speed-dependent shift, it is possible to observe a slight increase of the quality factor. The difference between the residuals helps to illustrate the asymmetry.

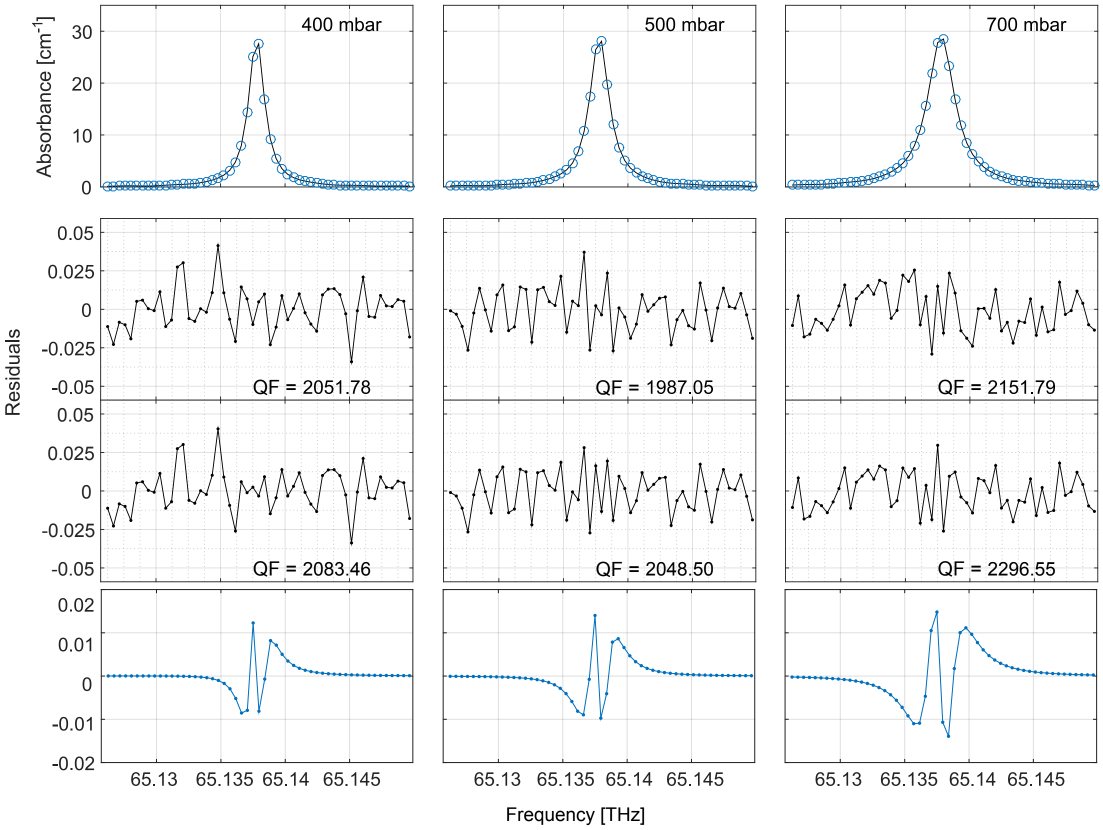

Figure 5.23: Asymmetry of the absorption line caused by the speed-dependent shift. First line: measurements and the fits for three pressures; second line: SDVPq fit without the SD shift of the line; third line: SP shift is included and causes minor changes; fourth line: the difference between the residuals without and with the shift included.

5.6.5 Line center frequencies

The line strength calculated for the measurement performed at 991.3 mbar does not agree with the values calculated from the other lines and was not included in the calculations. In comparison to HITRAN database, the values agrees within 2% for the lower pressures (400, 497 and 702.12 mbar) and it is within $\approx\ 9\%$ for 991.3. The line shift depends linearly on the pressure and the value in vacuum is calculated from a linear regression. Table 5.2 show the center of the lines together with the values from the the literature database for comparison. The table includes the line position for the low pressure measurements as well, performed with sub-nominal resolution. The accuracy for the measurements from this thesis are one standard deviation results from the fitting, which does not include the experimental factors such as temperature and pressure. A table showing accuracies are presented in section 5.7.

Table 5.2: Line centers in vacuum obtained from the measurements at 400, 497, *and* 702.12 *mbar. The values of four transitions are shown, together with the comparison with the HITRAN database.*

	R(7)	**R(9)**	**R(10)**	**R(11)**
(ν_0 − offset [GHz])	($\nu_0 - 65137$)	($\nu_0 - 65347$)	($\nu_0 - 65451$)	($\nu_0 - 65553$)
High-pressure fit	$0.670(12)$	$0.917(12)$	$0.4006(47)$	$0.784(17)$
Low pressure 1	$0.6704(2)$	$0.9173(2)$	$0.4016(2)$	$0.7889(2)$
Low pressure 2	$0.6686(1)$			
HITRAN	$0.670(30)$	$0.917(30)$	$0.402(30)$	$0.790(30)$
Ref. [123]	$0.6752(1)$	$0.9214(1)$	$0.4066(1)$	$0.7932(1)$

5.7 Discussion

The FTS was employed to acquire spectra at sub-nominal resolution. The spectra was not completely free of residual ILS. This effect was attributed to two factors. One is the divergence of the MIR beam. The second is the possible loss of coherence of the MIR beam. The divergence can be investigated by optimization of the MIR beam collimation, or with the use of an aperture in front of the FTS detectors. The loss of coherence, on the other hand, is not trivial to be studied. One approach is to perform optical heterodyne beat between the MIR and a reference laser. However, the lack of MIR optical references with coherence comparable to the frequency comb is still to be found.

The absorption measurements performed at low pressure are used to obtain the correction coefficient for adjusting the effective reference laser frequency. The FTS frequency grid is obtained by the sampling of the OPD, which is performed via the zero crossings of the reference laser. The reference laser provides accuracy (typically ≈ 1 MHz) for the initial estimation of the frequency grid which is less than one repetition rate of the laser (typically > 100 MHz). The correction coefficient is obtained from an optimization routine that uses the residual ILS amplitude to find the correct match between the frequency comb and the FTS grid.

The center frequency of the lines listed on table 5.2 are a clear evidence that the correcting the frequency grid by observing the mismatch between the frequency comb grid and the FT grid can be applied to acquire high-quality spectrum via a frequency comb based FTS. The accuracy of the pressure measurement (0.05%) is the limiting factor for calculating the number of molecules, and hence the line strength. The SNR and the absorption linewidth is the limiting factor to calibrate the frequency grid. The narrower the absorption line in relation to the frequency comb spacing, stronger is the ILS amplitude and the correction coefficient, found via minimizing the ILS amplitude. Lower noise on the baseline would provide better contrast to find smaller ILS variations. The accuracy on the measurements are listed in table 5.3.

Table 5.3: Accuracy values for each one of the experimental parameters.

		Accuracy		
	Value	Relative	Absolute	Units
Reference laser	4.74×10^8	2.00×10^{-9}	0.8	MHz
Temperature	293	4.00×10^{-6}	10^{-3}	K
Pressure	0.2	5×10^{-4}	10^{-4}	mbar
Path length	35.55	3×10^{-5}	10^{-3}	mm

The sub-nominal method is successfully applied to resolve absorption lines narrower than the OPD limitation of conventional FTS. Observing the residual ILS distortion, it is possible to provide the calibration of the reference laser via the frequency comb. A summary with the MIR frequency comb and the FTS achievements is shown in table 5.4.

Table 5.4: Specifications of the spectroscopy system. The SNR is considering 100 % *absorption. Spectral elements assuming a sub-nominal resolution of* 15 *MHz, which corresponds to* 10 *repetition rate steps.*

	Value	Units
Output range	2000 to 3300 | (5 to 3)	cm^{-1} | (µm)
Spectral coverage	80 | (170)	cm^{-1} | (nm)
Frequency step (optical)	15	MHz
Sensitivity	5.35×10^{-5}	$\mathrm{cm}^{-1}\mathrm{Hz}^{-1/2}$
Spectral elements	1.3×10^5	
SNR (A = 1)	> 2000	
Acquisition time (150 MHz)	4.1	s

The values for the spectral coverage, SNR, sensitivity are based on the measurements performed in CO. The 15 MHz frequency steps were performed 10 times to resolve the 150 MHz absorption line using the FTS with sub-nominal resolution. The spectral elements were calculated from optical bandwidth covered at the sub-nominal resolution of 15 MHz. The acquisition time is for each spectrum and the sensitivity was calculated via [124]

$$\alpha_{min} = (L\ \mathrm{SNR}_{\mathrm{std}})^{-1}\sqrt{\frac{T}{M}} \tag{5.7}$$

where, L is the sample path length (35.55 mm), $\mathrm{SNR}_{\mathrm{std}}$ the SNR in the spectrum, T is acquisition time (4.1 s for each of the 10 frequency steps of 15 MHz) over the 80 cm^{-1} bandwidth. The value for sensitivity is lower than other frequency comb based systems [124]. The measurements presented here were designed for highly-absorbing samples, and not intended to optimize sensitivity. The short sample path length is orders of magnitude lower than the effective length of kilometers from cavity enhanced systems.

6 Conclusion and outlook

The work reported in this thesis described the construction of a mid-infrared spectroscopy system and the acquisition of high-quality absorption spectra. The light source is a femtosecond mid-infrared frequency comb, which covers a broad bandwidth and provides high frequency accuracy.

Investigations of intensity noise of the MIR source showed that an optimal operation point exist for minimum noise operation, which is related to the temporal overlap of the pump and signal fields. An active stabilization of the temporal overlap was performed by detecting the noise at the FTS detectors and a feedback to a delay stage. The stabilization of the temporal delay was enough to allow long term spectroscopy measurements. It has been demonstrated that difference frequency generation is a reliable source for spectroscopy with high accuracy and signal-to-noise ratio.

Fourier transform spectroscopy is performed with a system designed to work with the frequency comb, allowing the retrieval of absorption features narrower than the limit set by the optical path difference. The fact that the ILS influence on the absorption feature depends on the match between the FTS frequency grid and the frequency comb spacing is explored. It allows the calibration of the FTS grid by the frequency comb, which provides high accuracy of the frequency axis. The system provided detection with high signal-to-noise ratios which resulted in quality factors of the absorption lines fittings reaching values above 2000.

Position and strength of four transitions were presented and the agreement with previous works within one standard deviation. The instantaneous optical bandwidth of the frequency comb covers the full R-branch of carbon monoxide. The spectrum covers approximate 2 THz, which was measured with 15 MHz frequency spacing and MHz accuracy on the retrieved transition frequencies. The full R-branch was measured and further analysis will be performed to provide state of the art values for line shape parameters. The difference frequency generation provided an adjustable output spectrum from 3 to 5 μm. Several relevant molecular transitions are covered within this range, such as methane, ammonia and carbon dioxide.

The instantaneous coverage of several transitions providesa large quantity of spectroscopy data in short time. The analysis of the transitions not presented in this thesis is in progress and will provide relevant experimental data, as the spectral region is not traditionally covered by coherent light sources. Measurements at different pressure ranges can be performed and the adjustment of the laser to cover the P-branch would offer a complete characterization of the fundamental carbon monoxide band.

An extended characterization of the MIR would contribute for future works with the difference frequency generation source. The minimum noise operation point is present throughout the spectrum and evidence was found that the temporal overlap position is different for each wavelength. Investigation of the temporal overlap within the minimum noise region with increased temporal resolution can provide insight on the time scales of this effect. The coherence of the MIR comb is yet to be performed directly at the MIR spectral region, with a possible heterodyne beat between an OPO and the DFG comb. The characterization of the MIR beam quality factor would provide a better understanding of the beam propagation and the optical path through the interferometer could be optimized even further.

The studies presented here were performed at room temperature. The absorption linewidths are Doppler limited were comparable with the frequency comb spacing, which is not the best scenario for the sub-nominal method. Lower temperatures would allow a samples with narrower absorption line to be measured and test the limits of the sub-nominal acquisition. The frequency comb steps can be performed at sub-MHz values, which would provide an order of magnitude increase in interleaving steps.

Bibliography

[1] M. Bass *et al.*, *Handbook of optics.* McGraw-Hill,, 2000.

[2] S. Svanberg, *Atomic and molecular spectroscopy: basic aspects and practical applications.* Springer Science & Business Media, 2012, vol. 6.

[3] B. Stuart, *Infrared spectroscopy.* Wiley Online Library, 2005.

[4] P. M. Chu, F. R. Guenther, G. C. Rhoderick, and W. J. Lafferty, "The NIST quantitative infrared database," *Journal of research of the National Institute of Standards and Technology*, vol. 104, no. 1, p. 59, 1999.

[5] I. Gordon, L. Rothman, C. Hill, R. Kochanov, Y. Tan, P. Bernath, M. Birk, V. Boudon, A. Campargue, K. Chance *et al.*, "The HITRAN2016 molecular spectroscopic database," *Journal of Quantitative Spectroscopy and Radiative Transfer*, 2017.

[6] S. W. Sharpe, T. J. Johnson, R. L. Sams, P. M. Chu, G. C. Rhoderick, and P. A. Johnson, "Gas-phase databases for quantitative infrared spectroscopy," *Applied spectroscopy*, vol. 58, no. 12, pp. 1452–1461, 2004.

[7] H. S. Müller, S. Thorwirth, D. Roth, and G. Winnewisser, "The cologne database for molecular spectroscopy, cdms," *Astronomy & Astrophysics*, vol. 370, no. 3, pp. L49–L52, 2001.

[8] R. Pohl, A. Antognini, F. Nez, F. D. Amaro, F. Biraben, J. M. Cardoso, D. S. Covita, A. Dax, S. Dhawan, L. M. Fernandes *et al.*, "The size of the proton," *Nature*, vol. 466, no. 7303, p. 213, 2010.

[9] O. L. Polyansky, R. I. Ovsyannikov, A. A. Kyuberis, L. Lodi, J. Tennyson, A. Yachmenev, S. N. Yurchenko, and N. F. Zobov, "Calculation of rotation-vibration energy levels of the ammonia molecule based on an ab initio potential energy surface," *Journal of Molecular Spectroscopy*, vol. 327, pp. 21–30, 2016.

[10] P. Chapovsky and L. Hermans, "Nuclear spin conversion in polyatomic molecules," *Annual review of physical chemistry*, vol. 50, no. 1, pp. 315–345, 1999.

[11] A. Miani and J. Tennyson, "Can ortho–para transitions for water be observed?" *The Journal of chemical physics*, vol. 120, no. 6, pp. 2732–2739, 2004.

[12] D. A. Horke, Y.-P. Chang, K. Długołęcki, and J. Küpper, "Separating para and ortho water," *Angewandte Chemie International Edition*, vol. 53, no. 44, pp. 11 965–11 968, 2014.

[13] P. Connes, "Early history of Fourier transform spectroscopy," *Infrared Physics*, vol. 24, no. 2-3, pp. 69–93, 1984.

[14] M. B. Comisarow and A. G. Marshall, "Fourier transform ion cyclotron resonance spectroscopy," *Chemical physics letters*, vol. 25, no. 2, pp. 282–283, 1974.

[15] R. R. Ernst and W. A. Anderson, “Application of Fourier transform spectroscopy to magnetic resonance,” *Review of Scientific Instruments*, vol. 37, no. 1, pp. 93–102, 1966.

[16] V. M. Devi, D. C. Benner, M. Smith, A. Mantz, K. Sung, L. Brown, and A. Predoi-Cross, “Spectral line parameters including temperature dependences of self-and air-broadening in the $2 \leftarrow 0$ band of CO at 2.3 µm,” *Journal of Quantitative Spectroscopy and Radiative Transfer*, vol. 113, no. 11, pp. 1013–1033, 2012.

[17] S. Albert, K. K. Albert, and M. Quack, “High-resolution Fourier transform infrared spectroscopy,” *Handbook of High-Resolution Spectroscopy*, 2011.

[18] S. Albert, K. K. Albert, and M. Quack, “Very high resolution studies of chiral molecules with a Bruker IFS 120 HR: The rovibrational spectrum of CDBrClF in the range 600-2300 cm^{-1},” in *Fourier Transform Spectroscopy*. Optical Society of America, 2003, p. FWD2.

[19] S. Albert and M. Quack, “High resolution rovibrational spectroscopy of chiral and aromatic compounds,” *ChemPhysChem*, vol. 8, no. 9, pp. 1271–1281, 2007.

[20] A. McKellar, D. Tokaryk, L.-H. Xu, D. Appadoo, and T. May, “High resolution analysis of the ν_{12} and ν_{17} fundamental bands of acrolein, CH_2CHCHO, in the 600 cm^{-1} region,” *Journal of Molecular Spectroscopy*, vol. 242, no. 1, pp. 31–38, 2007.

[21] A. McKellar, “High-resolution infrared spectroscopy with synchrotron sources,” *Journal of Molecular Spectroscopy*, vol. 262, no. 1, pp. 1–10, 2010.

[22] T. Chimdi, E. G. Robertson, L. Puskar, C. D. Thompson, M. J. Tobin, and D. McNaughton, “High resolution synchrotron FTIR spectroscopy of the far infrared ν_{10} and ν_{11} bands of R152a (CH_3CHF_2),” *Chemical Physics Letters*, vol. 465, no. 4, pp. 203–206, 2008.

[23] O. N. Ulenikov, O. V. Gromova, E. S. Bekhtereva, G. Onopenko, Y. S. Aslapovskaya, K.-H. Gericke, S. Bauerecker, and V.-M. Horneman, “High resolution FTIR study of the ν_7+ν_{10}-ν_{10} and ν_{10}+ ν_{12}-ν_{10} "hot" bands of C_2H_4,” *Journal of Quantitative Spectroscopy and Radiative Transfer*, vol. 149, pp. 318–333, 2014.

[24] E. Chukalina, M. Popova, L. Bezmaternykh, and I. Gudim, “Spectroscopic study of the magnetic ordering in $SmFe_3(BO_3)_4$,” *Physics Letters A*, vol. 374, no. 15, pp. 1790–1792, 2010.

[25] G. Carr, R. Smith, L. Mihaly, H. Zhang, D. Reitze, and D. Tanner, “High-resolution far-infrared spectroscopy at NSLS beamline U12IR,” *Infrared Physics & Technology*, vol. 51, no. 5, pp. 404–406, 2008.

[26] P. Roy, M. Rouzières, Z. Qi, and O. Chubar, “The AILES infrared beamline on the third generation synchrotron radiation facility SOLEIL,” *Infrared Physics & Technology*, vol. 49, no. 1, pp. 139–146, 2006.

[27] S. Albert, K. K. Albert, P. Lerch, and M. Quack, “Synchrotron-based highest resolution Fourier transform infrared spectroscopy of naphthalene ($C_{10}H_8$) and indole (C_8H_7N) and its application to astrophysical problems,” *Faraday discussions*, vol. 150, pp. 71–99, 2011.

[28] P. R. Griffiths and J. A. De Haseth, *Fourier transform infrared spectrometry*. John Wiley & Sons, 2007, vol. 171.

[29] H. Keller-Rudek, G. K. Moortgat, R. Sander, and R. Sörensen, "The MPI-Mainz UV/VIS spectral atlas of gaseous molecules of atmospheric interest," *Earth System Science Data*, vol. 5, no. 2, pp. 365–373, 2013.

[30] A. O ' Keefe and D. A. Deacon, "Cavity ring-down optical spectrometer for absorption measurements using pulsed laser sources," *Review of Scientific Instruments*, vol. 59, no. 12, pp. 2544–2551, 1988.

[31] K. C. Cossel, E. M. Waxman, I. A. Finneran, G. A. Blake, J. Ye, and N. R. Newbury, "Gas-phase broadband spectroscopy using active sources: progress, status, and applications," *JOSA B*, vol. 34, no. 1, pp. 104–129, 2017.

[32] S. Mirov, V. Fedorov, I. Moskalev, D. Martyshkin, and C. Kim, "Progress in Cr2+ and Fe2+ doped mid-IR laser materials," *Laser & Photonics Reviews*, vol. 4, no. 1, pp. 21–41, 2010.

[33] M. Ebrahim-Zadeh and K. Vodopyanov, "Mid-infrared coherent sources and applications: introduction," *J. Opt. Soc. Am. B*, vol. 33, no. 11, pp. MIC1–MIC1, Nov 2016. [Online]. Available: http://josab.osa.org/abstract.cfm?URI=josab-33-11-MIC1

[34] R. W. Boyd, *Nonlinear optics*. Academic press, 2003.

[35] A. Schliesser, N. Picqué, and T. W. Hänsch, "Mid-infrared frequency combs," *Nature Photonics*, vol. 6, no. 7, pp. 440–449, 2012.

[36] V. Petrov, "Frequency down-conversion of solid-state laser sources to the mid-infrared spectral range using non-oxide nonlinear crystals," *Progress in Quantum Electronics*, vol. 42, pp. 1–106, 2015.

[37] W. H. Louisell, A. Yariv, and A. E. Seigman, "Quantum fluctuations and noise in parametric processes. i." *Physical Review*, vol. 124, no. 6, pp. 1646–1654, 1961.

[38] R. L. Byer, S. E. Harris, and M. K. Oshman, "Observation of tunable optical parametric fluorescence." *Physical Review Letters*, vol. 18, no. 18, pp. 732–734, 1967.

[39] C. Fischer and M. W. Sigrist, *Mid-IR Difference Frequency Generation*. Berlin, Heidelberg: Springer Berlin Heidelberg, 2003, pp. 99–143.

[40] K. F. Lee, C. Mohr, J. Jiang, P. G. Schunemann, K. Vodopyanov, and M. Fermann, "Midinfrared frequency comb from self-stable degenerate gaas optical parametric oscillator," *Optics express*, vol. 23, no. 20, pp. 26 596–26 603, 2015.

[41] C. Wan, P. Li, A. Ruehl, and I. Hartl, "Coherent frequency division with a degenerate synchronously pumped optical parametric oscillator," *Optics letters*, vol. 43, no. 5, pp. 1059–1062, 2018.

[42] P. Maddaloni, G. Gagliardi, P. Malara, and P. De Natale, "A 3.5-mw continuous-wave difference-frequency source around 3 µm for sub-doppler molecular spectroscopy," *Applied Physics B: Lasers and Optics*, vol. 80, no. 2, pp. 141–145, 2005.

[43] M. Seiter and M. W. Sigrist, “Trace-gas sensor based on mid-IR difference-frequency generation in PPLN with saturated output power,” *Infrared physics & technology*, vol. 41, no. 5, pp. 259–269, 2000.

[44] T. W. Hänsch, “Nobel lecture: passion for precision,” *Reviews of Modern Physics*, vol. 78, no. 4, p. 1297, 2006.

[45] J. L. Hall, “Nobel lecture: Defining and measuring optical frequencies,” *Reviews of Modern Physics*, vol. 78, no. 4, p. 1279, 2006.

[46] M. Zimmermann, C. Gohle, R. Holzwarth, T. Udem, and T. W. Hänsch, “Optical clockwork with an offset-free difference-frequency comb: accuracy of sum-and difference-frequency generation,” *Optics letters*, vol. 29, no. 3, pp. 310–312, 2004.

[47] C. Erny, K. Moutzouris, J. Biegert, D. Kühlke, F. Adler, A. Leitenstorfer, and U. Keller, “Mid-infrared difference-frequency generation of ultrashort pulses tunable between 3.2 and 4.8 μm from a compact fiber source,” *Optics letters*, vol. 32, no. 9, pp. 1138–1140, 2007.

[48] B. Spaun, P. B. Changala, D. Patterson, B. J. Bjork, O. H. Heckl, J. M. Doyle, and J. Ye, “Continuous probing of cold complex molecules with infrared frequency comb spectroscopy,” *Nature*, vol. 533, no. 7604, pp. 517–520, 2016.

[49] C. Phillips, J. Jiang, C. Mohr, A. Lin, C. Langrock, M. Snure, D. Bliss, M. Zhu, I. Hartl, J. Harris *et al.*, “Widely tunable midinfrared difference frequency generation in orientation-patterned GaAs pumped with a femtosecond Tm-fiber system,” *Optics letters*, vol. 37, no. 14, pp. 2928–2930, 2012.

[50] A. Ruehl, M. J. Martin, K. C. Cossel, L. Chen, H. McKay, B. Thomas, C. Benko, L. Dong, J. M. Dudley, M. E. Fermann *et al.*, “Ultrabroadband coherent supercontinuum frequency comb,” *Physical Review A*, vol. 84, no. 1, p. 011806, 2011.

[51] N. Mina-Camilde, C. Manzanares I, and J. F. Caballero, “Molecular constants of carbon monoxide at $\nu = 0$, 1, 2, and 3: A vibrational spectroscopy experiment in physical chemistry,” *Journal of chemical education*, vol. 73, no. 8, p. 804, 1996.

[52] W. Demtröder, *Laser Spectroscopy 1: Basic Principles*, ser. SpringerLink : Bücher. Springer Berlin Heidelberg, 2014.

[53] R. K. Hanson, R. M. Spearrin, and C. S. Goldenstein, *Spectroscopy and optical diagnostics for gases*. Springer, 2016.

[54] L. S. Rothman, I. E. Gordon, Y. Babikov, A. Barbe, D. C. Benner, P. F. Bernath, M. Birk, L. Bizzocchi, V. Boudon, L. R. Brown *et al.*, “The HITRAN2012 molecular spectroscopic database,” *Journal of Quantitative Spectroscopy and Radiative Transfer*, vol. 130, pp. 4–50, 2013.

[55] K. L. Letchworth and D. C. Benner, “Rapid and accurate calculation of the Voigt function,” *Journal of Quantitative Spectroscopy and Radiative Transfer*, vol. 107, no. 1, pp. 173–192, 2007.

[56] J. Humlíček, “Optimized computation of the Voigt and complex probability functions,” *Journal of Quantitative Spectroscopy and Radiative Transfer*, vol. 27, no. 4, pp. 437–444, 1982.

[57] V. P. Kochanov, “On systematic errors in spectral line parameters retrieved with the Voigt line profile,” *Journal of Quantitative Spectroscopy and Radiative Transfer*, vol. 113, no. 12, pp. 1635–1641, 2012.

[58] A. Pine and R. Ciurylo, “Multispectrum fits of ar-broadened hf with a generalized asymmetric lineshape: effects of correlation, hardness, speed dependence, and collision duration,” *Journal of Molecular Spectroscopy*, vol. 208, no. 2, pp. 180–187, 2001.

[59] M. D. De Vizia, F. Rohart, A. Castrillo, E. Fasci, L. Moretti, and L. Gianfrani, “Speed-dependent effects in the near-infrared spectrum of self-colliding h 2 o 18 molecules,” *Physical Review A*, vol. 83, no. 5, p. 052506, 2011.

[60] D. Lisak and J. T. Hodges, “Low-uncertainty h2o line intensities for the 930-nm region,” *Journal of Molecular Spectroscopy*, vol. 249, no. 1, pp. 6–13, 2008.

[61] S. Wójtewicz, P. Masłowski, A. Cygan, P. Wcisło, M. Zaborowski, M. Piwiński, R. Ciuryło, and D. Lisak, “Speed-dependent effects and Dicke narrowing in nitrogen-broadened oxygen,” *Journal of Quantitative Spectroscopy and Radiative Transfer*, vol. 165, pp. 68–75, 2015.

[62] R. Ciuryło, “Shapes of pressure-and doppler-broadened spectral lines in the core and near wings,” *Physical Review A*, vol. 58, no. 2, p. 1029, 1998.

[63] J. Ward, J. Cooper, and E. W. Smith, “Correlation effects in the theory of combined doppler and pressure broadening—i. classical theory,” *Journal of Quantitative Spectroscopy and Radiative Transfer*, vol. 14, no. 7, pp. 555–590, 1974.

[64] P. R. Berman, “Speed-dependent collisional width and shift parameters in spectral profiles,” *Journal of Quantitative Spectroscopy and Radiative Transfer*, vol. 12, no. 9, pp. 1331–1342, 1972.

[65] J.-M. Hartmann, C. Boulet, and D. Robert, *Collisional effects on molecular spectra: laboratory experiments and models, consequences for applications*. Elsevier, 2008.

[66] B. Jeanna, S. Vitaly *et al.*, *Collisional line broadening and shifting of atmospheric gases: a practical guide for line shape modelling by current semi-classical approaches*. World Scientific, 2010.

[67] P. Del’Haye, T. Herr, E. Gavartin, M. Gorodetsky, R. Holzwarth, and T. J. Kippenberg, “Octave spanning tunable frequency comb from a microresonator,” *Physical Review Letters*, vol. 107, no. 6, p. 063901, 2011.

[68] J. Faist, G. Villares, G. Scalari, M. Rösch, C. Bonzon, A. Hugi, and M. Beck, “Quantum cascade laser frequency combs,” *Nanophotonics*, vol. 5, no. 2, pp. 272–291, 2016.

[69] M. Kourogi, K. Nakagawa, and M. Ohtsu, “Wide-span optical frequency comb generator for accurate optical frequency difference measurement,” *IEEE Journal of Quantum Electronics*, vol. 29, no. 10, pp. 2693–2701, 1993.

[70] S. A. Diddams, “The evolving optical frequency comb,” *JOSA B*, vol. 27, no. 11, pp. B51–B62, 2010.

[71] J. Ye and S. T. Cundiff, *Femtosecond optical frequency comb: principle, operation and applications*. Springer Science & Business Media, 2005.

[72] S. T. Cundiff and J. Ye, “Colloquium: Femtosecond optical frequency combs,” *Reviews of Modern Physics*, vol. 75, no. 1, p. 325, 2003.

[73] T. Udem, R. Holzwarth, and T. W. Hänsch, “Optical frequency metrology,” *Nature*, vol. 416, no. 6877, p. 233, 2002.

[74] D. Matei, T. Legero, S. Häfner, C. Grebing, R. Weyrich, W. Zhang, L. Sonderhouse, J. Robinson, J. Ye, F. Riehle *et al.*, “1.5 μm lasers with sub-10 mHz linewidth,” *Physical review letters*, vol. 118, no. 26, p. 263202, 2017.

[75] N. R. Newbury and W. C. Swann, “Low-noise fiber-laser frequency combs,” *JOSA B*, vol. 24, no. 8, pp. 1756–1770, 2007.

[76] H. R. Telle, G. Steinmeyer, A. Dunlop, J. Stenger, D. Sutter, and U. Keller, “Carrier-envelope offset phase control: A novel concept for absolute optical frequency measurement and ultrashort pulse generation,” *Applied Physics B*, vol. 69, no. 4, pp. 327–332, 1999.

[77] J. M. Dudley, G. Genty, and S. Coen, “Supercontinuum generation in photonic crystal fiber,” *Reviews of modern physics*, vol. 78, no. 4, p. 1135, 2006.

[78] M. J. Thorpe, K. D. Moll, R. J. Jones, B. Safdi, and J. Ye, “Broadband cavity ringdown spectroscopy for sensitive and rapid molecular detection,” *Science*, vol. 311, no. 5767, pp. 1595–1599, 2006.

[79] F. Adler, M. J. Thorpe, K. C. Cossel, and J. Ye, “Cavity-enhanced direct frequency comb spectroscopy: technology and applications,” *Annual Review of Analytical Chemistry*, vol. 3, pp. 175–205, 2010.

[80] C. Gohle, B. Stein, A. Schliesser, T. Udem, and T. W. Hänsch, “Frequency comb vernier spectroscopy for broadband, high-resolution, high-sensitivity absorption and dispersion spectra,” *Physical review letters*, vol. 99, no. 26, p. 263902, 2007.

[81] A. Khodabakhsh, V. Ramaiah-Badarla, L. Rutkowski, A. C. Johansson, K. F. Lee, J. Jiang, C. Mohr, M. E. Fermann, and A. Foltynowicz, “Fourier transform and vernier spectroscopy using an optical frequency comb at 3–5.4 μm,” *Optics letters*, vol. 41, no. 11, pp. 2541–2544, 2016.

[82] G. Kowzan, K. Stec, M. Zaborowski, S. Wójtewicz, A. Cygan, D. Lisak, P. Masłowski, and R. Trawiński, “Line positions, pressure broadening and shift coefficients for the second overtone transitions of carbon monoxide in argon,” *Journal of Quantitative Spectroscopy and Radiative Transfer*, vol. 191, pp. 46–54, 2017.

[83] D. Mondelain, T. Sala, S. Kassi, D. Romanini, M. Marangoni, and A. Campargue, “Broadband and highly sensitive comb-assisted cavity ring down spectroscopy of CO near 1.57 μm with sub-MHz frequency accuracy,” *Journal of Quantitative Spectroscopy and Radiative Transfer*, vol. 154, pp. 35–43, 2015.

[84] S. Barbieri, P. Gellie, G. Santarelli, L. Ding, W. Maineult, C. Sirtori, R. Colombelli, H. Beere, and D. Ritchie, “Phase-locking of a 2.7-THz quantum cascade laser to a mode-locked erbium-doped fibre laser,” *Nature Photonics*, vol. 4, no. 9, p. 636, 2010.

[85] S. Schiller, “Spectrometry with frequency combs,” *Optics letters*, vol. 27, no. 9, pp. 766–768, 2002.

[86] G. Ycas, F. R. Giorgetta, E. Baumann, I. Coddington, D. Herman, S. A. Diddams, and N. R. Newbury, "High coherence mid-infrared dual comb spectroscopy spanning 2.6 to 5.2 microns," *arXiv preprint arXiv:1709.07105*, 2017.

[87] R. H. Norton and R. Beer, "New apodizing functions for Fourier spectrometry," *JOSA*, vol. 66, no. 3, pp. 259–264, 1976.

[88] P. Maslowski, K. F. Lee, A. C. Johansson, A. Khodabakhsh, G. Kowzan, L. Rutkowski, A. A. Mills, C. Mohr, J. Jiang, M. E. Fermann *et al.*, "Surpassing the path-limited resolution of Fourier-transform spectrometry with frequency combs," *Physical Review A*, vol. 93, no. 2, p. 021802, 2016.

[89] L. Rutkowski, P. Masłowski, A. C. Johansson, A. Khodabakhsh, and A. Foltynowicz, "Optical frequency comb Fourier transform spectroscopy with sub-nominal resolution and precision beyond the Voigt profile," *Journal of Quantitative Spectroscopy and Radiative Transfer*, vol. 204, pp. 63–73, 2018.

[90] Y. Nakajima, H. Inaba, K. Hosaka, K. Minoshima, A. Onae, M. Yasuda, T. Kohno, S. Kawato, T. Kobayashi, T. Katsuyama *et al.*, "A multi-branch, fiber-based frequency comb with millihertz-level relative linewidths using an intra-cavity electro-optic modulator," *Optics Express*, vol. 18, no. 2, pp. 1667–1676, 2010.

[91] F. Adler, A. Sell, F. Sotier, R. Huber, and A. Leitenstorfer, "Attosecond relative timing jitter and 13 fs tunable pulses from a two-branch Er:fiber laser," *Optics letters*, vol. 32, no. 24, pp. 3504–3506, 2007.

[92] R. Paschotta, J. Nilsson, A. C. Tropper, and D. C. Hanna, "Ytterbium-doped fiber amplifiers," *IEEE Journal of quantum electronics*, vol. 33, no. 7, pp. 1049–1056, 1997.

[93] I. Hartl, G. Imeshev, L. Dong, G. C. Cho, and M. E. Fermann, "Ultra-compact dispersion compensated femtosecond fiber oscillators and amplifiers," in *Lasers and Electro-Optics, 2005.(CLEO). Conference on*, vol. 3. IEEE, 2005, pp. 1641–1643.

[94] D. Strickland and G. Mourou, "Compression of amplified chirped optical pulses," *Optics communications*, vol. 55, no. 6, pp. 447–449, 1985.

[95] R. Trebino, *Frequency-resolved optical gating: the measurement of ultrashort laser pulses*. Springer Science & Business Media, 2012.

[96] R. Trebino, K. W. DeLong, D. N. Fittinghoff, J. N. Sweetser, M. A. Krumbügel, B. A. Richman, and D. J. Kane, "Measuring ultrashort laser pulses in the time-frequency domain using frequency-resolved optical gating," *Review of Scientific Instruments*, vol. 68, no. 9, pp. 3277–3295, 1997.

[97] A. Ruehl, A. Gambetta, I. Hartl, M. E. Fermann, K. S. Eikema, and M. Marangoni, "Widely-tunable mid-infrared frequency comb source based on difference frequency generation," *Optics letters*, vol. 37, no. 12, pp. 2232–2234, 2012.

[98] D. H. Jundt, "Temperature-dependent sellmeier equation for the index of refraction, n e, in congruent lithium niobate," *Optics Letters*, vol. 22, no. 20, pp. 1553–1555, 1997.

[99] D. S. Hum and M. M. Fejer, "Quasi-phasematching," *Comptes Rendus Physique*, vol. 8, no. 2, pp. 180–198, 2007.

[100] G. Krauss, D. Fehrenbacher, D. Brida, C. Riek, A. Sell, R. Huber, and A. Leitenstorfer, “All-passive phase locking of a compact Er:fiber laser system,” *Optics letters*, vol. 36, no. 4, pp. 540–542, 2011.

[101] F. C. Cruz, D. L. Maser, T. Johnson, G. Ycas, A. Klose, F. R. Giorgetta, I. Coddington, and S. A. Diddams, “Mid-infrared optical frequency combs based on difference frequency generation for molecular spectroscopy,” *Optics express*, vol. 23, no. 20, pp. 26 814–26 824, 2015.

[102] S. A. Meek, A. Poisson, G. Guelachvili, T. W. Hänsch, and N. Picqué, “Fourier transform spectroscopy around 3 µm with a broad difference frequency comb,” *Applied Physics B*, vol. 114, no. 4, pp. 573–578, 2014.

[103] A. Gambetta, N. Coluccelli, M. Cassinerio, D. Gatti, P. Laporta, G. Galzerano, and M. Marangoni, “Milliwatt-level frequency combs in the 8–14 µm range via difference frequency generation from an Er:fiber oscillator,” *Optics letters*, vol. 38, no. 7, pp. 1155–1157, 2013.

[104] L. Fu, B. K. Thomas, and L. Dong, “Efficient supercontinuum generations in silica suspended core fibers,” *Optics express*, vol. 16, no. 24, pp. 19 629–19 642, 2008.

[105] A. Mayer, C. Phillips, C. Langrock, A. Klenner, A. Johnson, K. Luke, Y. Okawachi, M. Lipson, A. Gaeta, M. Fejer *et al.*, “Offset-free gigahertz midinfrared frequency comb based on optical parametric amplification in a periodically poled lithium niobate waveguide,” *Physical Review Applied*, vol. 6, no. 5, p. 054009, 2016.

[106] T. W. Neely, T. A. Johnson, and S. A. Diddams, “High-power broadband laser source tunable from 3.0 µm to 4.4 µm based on a femtosecond Yb:fiber oscillator,” *Optics letters*, vol. 36, no. 20, pp. 4020–4022, 2011.

[107] R. S. Hughes, “Logarithmic amplification: with application to radar and EW,” *Dedham, MA, Artech House, Inc., 1986, 205 p.*, 1986.

[108] C. Homann and E. Riedle, “Direct measurement of the effective input noise power of an optical parametric amplifier,” *Laser & Photonics Reviews*, vol. 7, no. 4, pp. 580–588, 2013.

[109] D. Wetterdienst. (2018). [Online]. Available: https://www.dwd.de/EN/research/research_node.html

[110] J. Piotrowski and W. Gawron, “Ultimate performance of infrared photodetectors and figure of merit of detector material,” *Infrared physics & technology*, vol. 38, no. 2, pp. 63–68, 1997.

[111] L. Vina, C. Umbach, M. Cardona, and L. Vodopyanov, “Ellipsometric studies of electronic interband transitions in Cd$_x$Hg$_{1-x}$Te,” *Physical Review B*, vol. 29, no. 12, p. 6752, 1984.

[112] D. E. Aspnes and A. Studna, “Dielectric functions and optical parameters of Si, Ge, GaP, GaAs, GaSb, InP, InAs, and InSb from 1.5 to 6.0 ev,” *Physical review B*, vol. 27, no. 2, p. 985, 1983.

[113] A. Rogalski, “Infrared detectors: status and trends,” *Progress in quantum electronics*, vol. 27, no. 2, pp. 59–210, 2003.

[114] H. Carleton and W. Maloney, “A balanced optical heterodyne detector,” *Applied optics*, vol. 7, no. 6, pp. 1241–1243, 1968.

[115] R. Stierlin, R. Bättig, P.-D. Henchoz, and H. Weber, "Excess-noise suppression in a fibre-optic balanced heterodyne detection system," *Optical and quantum electronics*, vol. 18, no. 6, pp. 445–454, 1986.

[116] H. P. Yuen and V. W. Chan, "Noise in homodyne and heterodyne detection," *Optics letters*, vol. 8, no. 3, pp. 177–179, 1983.

[117] I. Hartl, X. Li, C. Chudoba, R. Ghanta, T. Ko, J. Fujimoto, J. Ranka, and R. Windeler, "Ultrahigh-resolution optical coherence tomography using continuum generation in an air–silica microstructure optical fiber," *Optics letters*, vol. 26, no. 9, pp. 608–610, 2001.

[118] P. E. Ciddor, "Refractive index of air: new equations for the visible and near infrared," *Applied optics*, vol. 35, no. 9, pp. 1566–1573, 1996.

[119] A. G. Maki and J. S. Wells, "New wavenumber calibration tables from heterodyne frequency measurements," *Journal of research of the National Institute of Standards and Technology*, vol. 97, no. 4, p. 409, 1992.

[120] R. J. Mathar, "Wide-band and air dispersion effecting the abcd algorithm of phase-recovery in long-baseline interferometry," *arXiv preprint astro-ph/0605304*, 2006.

[121] A. Cygan and D. Lisak, "Multi-spectrum fitting software for advanced spectral line shapes analysis," in *Journal of Physics: Conference Series*, vol. 810, no. 1. IOP Publishing, 2017, p. 012025.

[122] E. Lanzinger, K. Jousten, and M. Kühne, "Partial pressure measurement by means of infrared laser absorption spectroscopy," *Vacuum*, vol. 51, no. 1, pp. 47–51, 1998.

[123] A. Predoi-Cross, K. Esteki, H. Rozario, H. Naseri, S. Latif, F. Thibault, V. M. Devi, M. Smith, and A. Mantz, "Theoretical and revisited experimentally retrieved he-broadened line parameters of carbon monoxide in the fundamental band," *Journal of Quantitative Spectroscopy and Radiative Transfer*, vol. 184, pp. 322–340, 2016.

[124] A. Foltynowicz, P. Masłowski, T. Ban, F. Adler, K. Cossel, T. Briles, and J. Ye, "Optical frequency comb spectroscopy," *Faraday discussions*, vol. 150, pp. 23–31, 2011.

A Oscillator modification

The oscillator was reworked because two different components were damaged: the saturable absorber mirror (SAM), and the gain fiber section. The SAM is a crucial component for stable laser operation. The SAM specifications highly depends on the fabrication conditions. Even though a SAM with similar specifications as the original was acquired, it was necessary to test different SAMs to obtain the spectrum closest to the original mode-locked. Table A.1 summarizes the specifications of the tested SAMs and their absorption spectra.

Type	TC(ps)	R(%)	MD (%)	NSL (%)	SF (μJ/cm^2)
1040-65 (original)	**0.5**	**35**	**35**	**30**	**20**
1040-60	0.5	40	35	25	30
1040-35	3	65	26	9	50
1040-43	1	57	25	18	70
1040-45	0.5	55	25	20	50
1040-48	1	52	29	19	60

Table A.1: List of the tested saturable absorber mirrors. TC: time constant. R: reflectance. MD: modulation depth. NSL: Non-saturable losses. SF: saturation fluence.

They are all designed for operation at 1040 nm. Nevertheless, their reflectance spectra (shown in figure A.1) shows a shift on the center wavelength. Despite being for information only, they illustrate how the reflectance minimum can vary from the specifications.

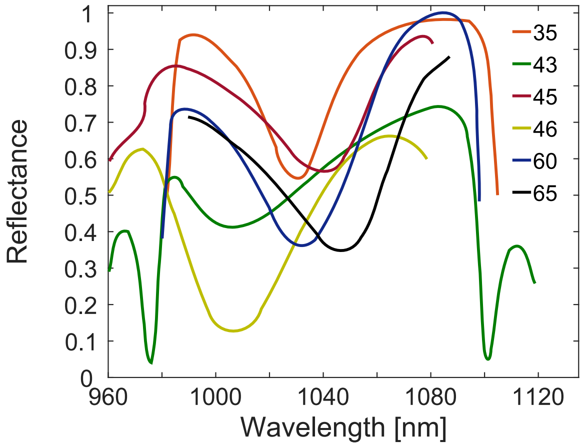

Figure A.1: Reflectance spectra for the SAMs tested in the oscillator.

The focusing condition on the SAM was also modified, because the original SAM had a lower saturation fluence. Figure A.2 show a summary of the achieved results while investigating SAMs. The focusing spot was modified by exchanging the collimation and focusing lenses on the free-space section of the oscillator. The legend shows the amplification ratio being used.

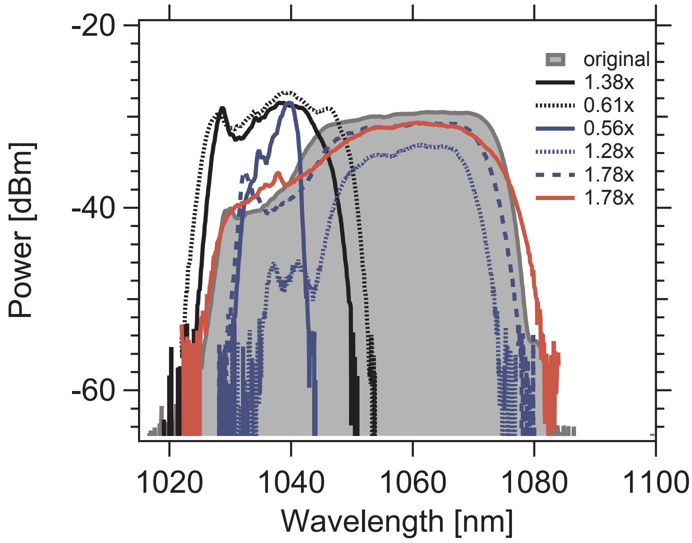

Figure A.2: Oscillator output spectra. The original spectrum is shown in the gray background. Black: SAM 1040-60. Blue: 1040-48. Red: 1040-48 with optimized oscillator alignment.

The oscillator stopped working because of a damaged splicing point in the cavity, which occurred between the fiber Bragg grating and the gain fiber. In order to perform a new splice, a few millimeters of gain fiber were removed. It is a sensitive point, specially because of the high doping concentration of the gain fiber. The overall cavity gain reduced and altered the pulse evolution, due to new dispersion and nonlinear effects values. The output power was also lower compared to the previous condition (10 mW instead of 100 mW).

The new oscillator spectra were narrower and would support, in the best case, bandwidth limited pulses of 70 fs instead of 60 fs. Despite this fact, attempts to characterize this pulse were made. With the new spectra, only longer pulses could be generated after amplification. The solution was to modify other experiment and to take a new seed from another oscillator using a fiber splitter. Further work with the old oscillator was considered to be out of the scope of the project. Figure A.3 shows the change between the old oscillator and the new achieved spectra.

The work with the oscillator is considered finished and the efforts were turned to the amplifier. All the results presented in the thesis uses the second oscillator as a seed.

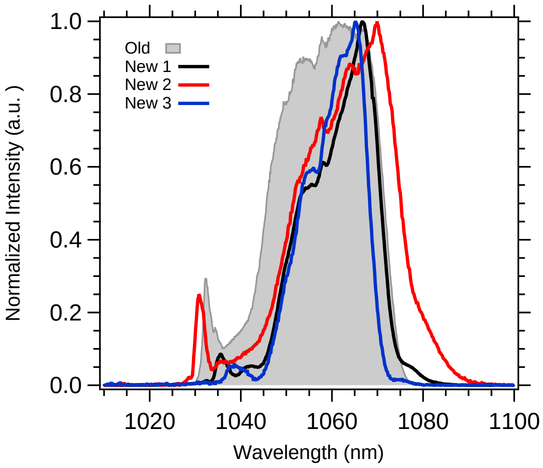

Figure A.3: Comparison between the oscillator spectrum before and after the damage occurred. The FWHM of the seed spectrum decreased from 25.8 nm to 23.3 nm.

B Reference laser frequency measurement

The reference laser is used to record the displacement of the retroreflectors and provide a way to sample the MIR interferogram at equidistant values of OPD. When performing measurements with high-accuracy, it is important to know the frequency and stability of the reference laser. The reference laser frequency was measured with an heterodyne beat with the frequency comb. The figure shows the beat notes and the Gaussian fit to retrieve the linewidths at seconds integration time.

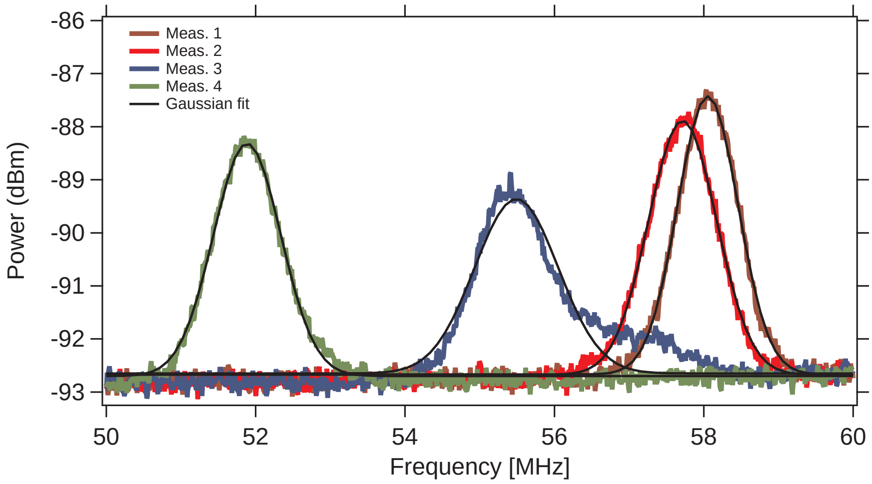

Figure B.1: Optical heterodyne beat between the reference laser and the comb.

Table B.1: Results from the heterodyne beat between the frequency comb and the reference laser

$f_{\mathbf{rep}}$ [MHz]	$f_{\mathbf{ceo}}$ [MHz]	n	$f_{\mathbf{beat}}$ [MHz]	ν_{ref} [MHz]	
150.34049773	123	3150264	58.055	473612437.4	
150.34049761	123	3150264	57.716	473612438.2	
150.34049727	123	3150264	55.492	473612434.6	
150.34264413	123	3150219	51.886	473612428.9	
				473612435.0	**Mean**
				4.191	**Std.**

The standard deviation of the width from the beat notes 1, 2, 3 and 4 are respectively, 575.01, 647.11, 792.38 and 640.06 kHz. Assuming the initial frequency from the specification sheet of the reference laser (473612.4366 GHz) to retrieve the comb numbers. The measurements yield a frequency of the reference laser of 473612.4359 GHz with 4.2 MHz standard deviation.

C Fitting results

Fitting results for the R(7), R(9), R(10), R(11) lines.

R(7)

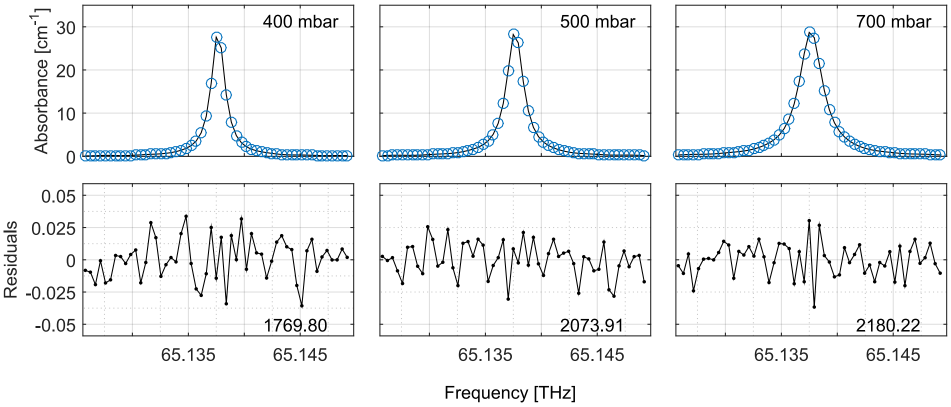

Figure C.1: Results from the SPVPq fitting of the R(7) line.

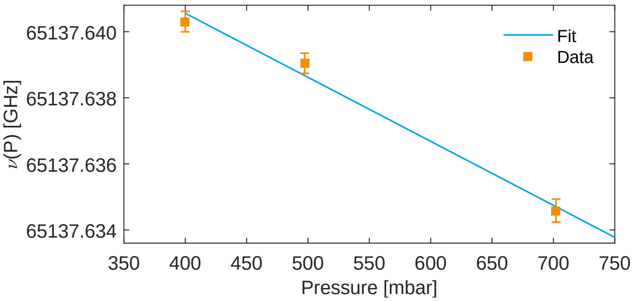

Figure C.2: The R(7) line center at three pressures. The linear regression provides the line center in vacuum.

R(9)

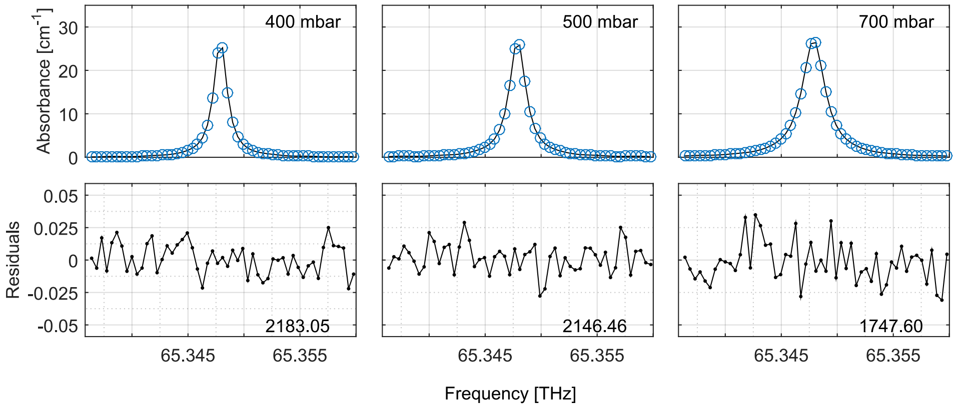

Figure C.3: Results from the SPVPq fitting of the R(9) line.

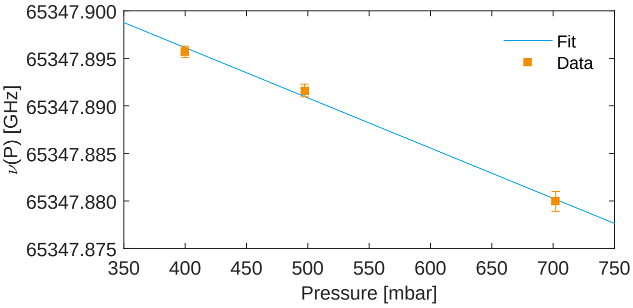

Figure C.4: The R(9) line center at three pressures.

R(10)

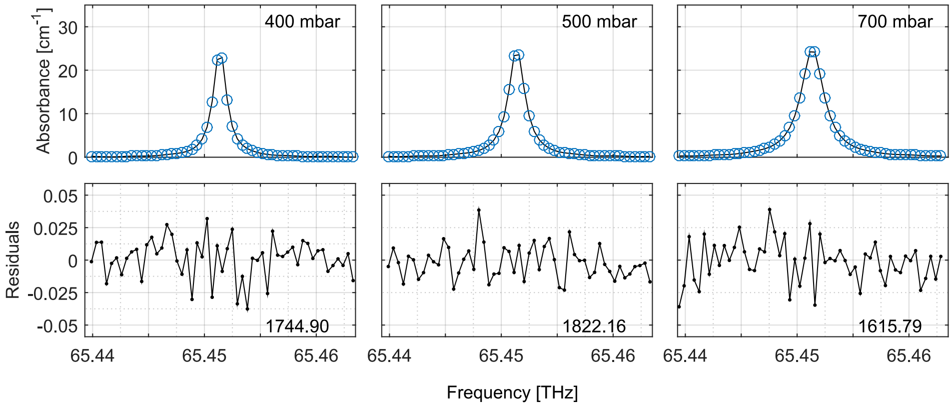

Figure C.5: Results from the SPVPq fitting of the R(10) line.

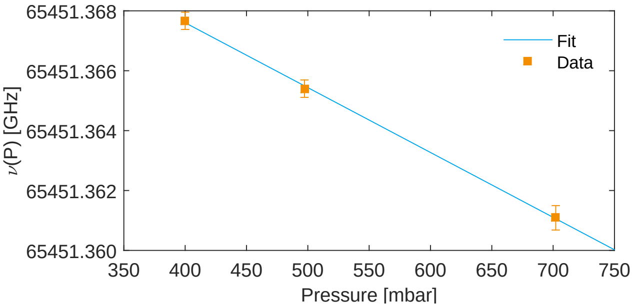

Figure C.6: The R(10) line center at three pressures.

R(11)

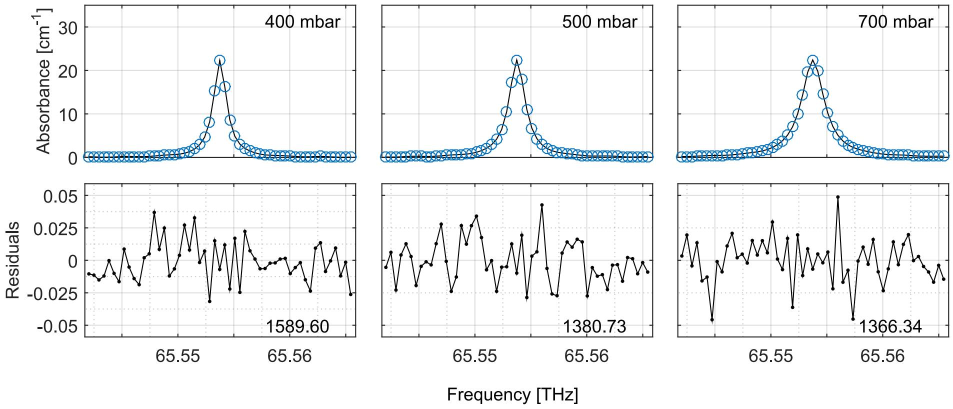

Figure C.7: Results from the SPVPq fitting of the R(11) line.

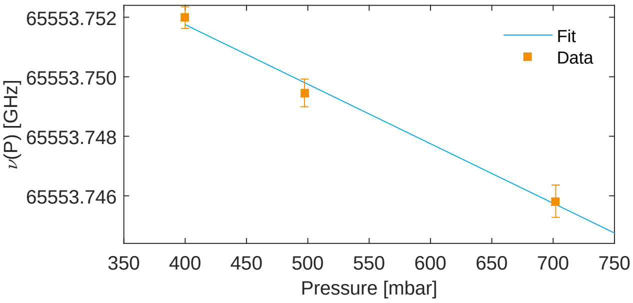

Figure C.8: The R(11) line center at three pressures. The linear regression provides the line center in vacuum.

Line parameters

Table C.1: Retrieved speed-dependent width parameters (a_w), no units.

Pressure [mbar]	**R(7)**	**R(9)**	**R(10)**	**R(11)**
400	0.1059(63)	0.1142(49)	0.1003(68)	0.0579(86)
497.27	0.1094(17)	0.0946(48)	0.1001(55)	0.0718(89)
702.13	0.1062(36)	0.0668(64)	0.0903(54)	0.0830(71)

Table C.2: Retrieved speed-dependent shift parameters (a_s), no units.

Pressure [mbar]	**R(7)**	**R(9)**	**R(10)**	**R(11)**
400	0.68(11)	0.30(10)	0.26(11)	0.79(22)
497.27	0.33(11)	0.40(11)	0.22(9)	0.25(21)
702.13	0.33(9)	0.46(16)	0.03(11)	0.07(16)

Table C.3: Retrieved N_2 line broadening coefficient (γ_{N_2}) in $[cm^{-1}/atm]$.

	R(7)	**R(9)**	**R(10)**	**R(11)**
N_2 - retrieved	0.0631	0.0592	0.0596	0.0597
Air - Ref. [5]	0.0599	0.058	0.0573	0.0567

Table C.4: Retrieved N_2 line shifting coefficient (δ_{N_2}) in $[cm^{-1}/atm]$.

	R(7)	**R(9)**	**R(10)**	**R(11)**
N_2 - retrieved	-0.0016(11)	-0.0018(10)	-0.0018(9)	-0.0017(11)
Air - Ref. [5]	-0.003	-0.003	-0.003	-0.003

Vinicius Silva de Oliveira received support from CNPq, Conselho Nacional de Desenvolvimento Científico e Tecnológico - Brasil